# Compressible single and dual stream jet stability and adjoint-based sensitivity analysis in relationship with aeroacoustics

Tobias Ansaldi

# THÈSE

**En vue de l'obtention du**

## DOCTORAT DE L'UNIVERSITÉ DE TOULOUSE

**Délivré par :**

Institut National Polytechnique de Toulouse (INP Toulouse)

**Discipline ou spécialité :**

Dynamique des fluides

---

**Présentée et soutenue par :**

M. TOBIAS ANSALDI

le vendredi 14 octobre 2016

**Titre :**

COMPRESSIBLE SINGLE AND DUAL STREAM JET STABILITY AND ADJOINT-BASED SENSITIVITY ANALYSIS IN RELATIONSHIP WITH AEROACOUSTICS

---

**Ecole doctorale :**

Mécanique, Energétique, Génie civil, Procédés (MEGeP)

**Unité de recherche :**

Institut de Mécanique des Fluides de Toulouse (I.M.F.T.)

**Directeur(s) de Thèse :**

M. CHRISTOPHE AIRIAU

**Rapporteurs :**

M. JEAN-CHRISTOPHE ROBINET, ENSAM - ARTS ET METIERS PARISTECH

M. UWE EHRENSTEIN, AIX-MARSEILLE UNIVERSITE

**Membre(s) du jury :**

M. YVES GERVAIS, UNIVERSITE DE POITIERS, Président

M. JEAN-PHILIPPE BRAZIER, ONERA TOULOUSE, Membre

M. JEROME HUBER, AIRBUS FRANCE, Membre

# Abstract

This thesis leads to a better knowledge of the physic and of the control of acoustic radiation in turbulent single and dual-stream jets. It is known that jet noise is produced by the turbulence present in the jet that can be separated in large coherent structures and fine structures. It is also concluded that these large-scale coherent structures are the instability waves of the jet and can be modelled as the flow field generated by the evolution of instability waves in a given turbulent jet. The growth rate and the streamwise wavenumber of a disturbance with a fixed frequency and azimuthal wavenumber are obtained by solving the non-local approach called Parabolized Stability Equations (PSE). Typically the Kelvin-Helmholtz instability owes its origin into the shear layer of the flow and, moreover, the inflection points of the mean velocity profile has a crucial importance in the instability of such a flow. The problem is more complex in case of imperfectly expanded jet where shock-cells manifest inside the jet and strongly interaction with the instability waves has been observed. Several configurations are tested in this thesis, from a subsonic incompressible case to the dual-stream underexpanded supersonic jet obtained by solving Large Eddy Simulations LES (CERFACS). The acoustic far-field is determined by the Ffowcs-Williams-Hawkings acoustic analogy. Then a sensitivity analysis of the jet with respect to external forcing acting in a localized region of the flow are investigated by solving the adjoint PSE equations. High sensitivity appeared in the shear-layer of the flow showing, also, a high dependency in the streamwise and radial direction. In the case of dual-stream jet the propagation of the instability in the inner and outer shear layer should be taken into account. This configuration leads to two different distinct Klevin-Helmholtz modes that are computed separately. The highest sensitivity is determined in the exit of the nozzle outside of the potential core of the jet. In addition, comparison between sensitivity computed by adjoint equations and Uncertainty Quantification (UQ) methods has been done, in the case of a single-stream jet, showing a link between these two methods for small variations of the input parameters. This result leads to the application of a lower cost tool for mathematical analysis of complex problem of industrial interest. This work and in particular the sensitivity theory investigated in this thesis contribute to a development of a new noise control strategy for aircraft jet.

# Résumé

La thèse est relative à la compréhension de la physique et au contrle des émissions acoustiques dans les jets tubulents simples et double-flux. La génération du bruit est associé à des structures turbulentes de grandes tailles caractéristiques et à la turbulence de petites échelles. i Il est maintenant admis que les structures de grandes échelles sont des instabilités se propageant dans un champ moyen turbulent. Ici elle sont analysées sur la base de la théorie linéaire non locale appelées PSE pour Parabolized Stability Equations. Ces instabilités inflexionnelles associées à la présence de couche de cisaillement sont des modes de Kelvin-Helmhotz. Dans le cas du jet sous détentu des cellules de choc apparaissent et influencent très fortement les taux damplification et fréquences des modes propres. Divers écoulements sont investigués, de faible nombre de Mach au jet double-flux supersonique dont le champ moyen provient de simulation LES (Cerfacs). Le champ acoustique lointain est déterminé par lanalogie de Ffowcs-Williams-Hawkings. Ensuite une étude de sensibilité originales des instabilités et du bruits par rapport à divers forage locaux est produite sur la base des équations de stabilité PSE adjointes. Les fortes sensibilités apparaissent dans les couches de cisaillements et aussi dans une moindre mesure autour des cellules de chocs. Les sensibilités sont plus complexes pour le jet double flux et dépendent du mode instable étudié lié soit au jet primaire soit au jet secondaire. Les sensibilités maximales se trouvent au voisinage de la sortie de la tuyère et à la limite ou à l'extérieur du cne potentiel. En complément une étude sur le jet simple flux permet de mettre en rapport les approches de quantification dincertitude et la sensibilité calculée par des équations adjointes. Les résultats de sensibilité vont permettre de contribuer à proposer des stratégies de contrle aéroacoustique dans les jets de turboréacteurs.

# Contents

# Introduction

Recent rise in aviation transport and environmental concern has caused a growing interest in environmentally friendly aircrafts. Pollutant emissions have raised over the past years. The concentration of carbon dioxide ($CO_2$) in the atmosphere has increased by more than 30% after the industrial revolution. Greenhouse gases contribute to climate change and global warming, in addition to other environmental impacts, such as sulphuric acid formation in the atmosphere, and health problems like respiratory diseases. From an aerodynamic point of view, gas emissions from aircrafts can be related to the gas consumption caused by the drag. Furthermore, there is another issue which concerns aircrafts and causes environmental and health problems: the noise. Continuous exposure to high levels of noise, for example in the vicinity of an airport, may induce temporal or permanent health problems. Some of them are increase in stress, blood pressure and heart rate. Cardiovascular effects are associated with long-term exposure to values in the range of 65 to 70 dB or more, for both air- and road-traffic noise. A mechanical damage of the ear can occur with very high instantaneous Sound Pressure Levels (around 140dB for adults and 120dB for children). Aircraft noise has three main sources, namely mechanical, aerodynamic and from aircraft systems. Mechanical noise is mainly produced by the engines. The aerodynamic noise is created by the unsteady flow around airframes. Aircraft systems contribute to the interior cabin noise. During landing, aerodynamic noise is as important as mechanical noise, thus the interest to reduce it. Nowadays the understanding of these problems are motivating the research on environmentally friendly aircrafts, that is to say aircrafts which are more affordable, safer, cleaner and quieter.

### AeroTraNet 2 project

This PhD thesis is part of an European Project named AEROnautical TRAining NETwork 2. he AeroTraNet project concerns the investigation of modelling shock cell noise in a wide-body aircraft engine configuration from private sector partner Airbus France, by shock-tolerant numerical modelling for under-expanded jets (ULEIC), large eddy simulations for turbulent jets with weak shocks (Cerfacs), advanced flow-noise correlations (UNIROMA TRE), jet and near-field noise experiments (VKI), reduced-order modelling and flow control (IMFT-INP), and advanced laser-based measurement techniques (INSEAN).

**Overview of the thesis**

The objective of this thesis is to propose a mathematical model to analyse sensitivity in jets. Several cases are investigated in this work. The analysis is permormed from an incompressible semi-empirical case to the interaction between shock cell and Kelvin-Helmholtz instabilities for an under-expanded dual stream jet case. In order to model the flow instability the Parabolized Stability Equations (PSE) are solved. This approach takes into account of the streamwise variation of the base flow and in presence of shock-cell the interaction between instabilities and shock-cells.

A sensitivity analysis is performed to determine the most sensitive region of the flow to external forcing. The adjoint code developed at IMFT is used to solve the sensitivity functions. The code shows a good flexibility to analyze different cases with increasing complexity. In particular, four cases are taken in exam:

1. Incompressible single stream jet (calculated by semi-empirical law).
2. Supersonic perfectly expanded single stream jet (calculated by semi-empirical law).
3. Supersonic under-expanded single stream jet (calculated by Large Eddy Simulation).
4. Supersonic under-expanded dual stream jet (calculated by Large Eddy Simulation).

Necessarily, a "complex" numerical chain to connect PSE and adjoint PSE solver has been developed and implemented with blocks written in FORTRAN 90 and MATLAB. The different blocks exchange data between each others through shell BASH scripts.

A general overview of the bibliography in jet noise is given in chapter I. Theoretical, numerical and experimental approaches are discussed highlighting the previous works that provide the base of this thesis.

Chapter II describes the numerical method used to implement the direct simulation algorithm (PSE solver). The PSE solver has been developed by the ONERA's team[63]. First, the code is validated by comparing with known results, then the direct algorithm is used to investigate the interaction between shock-cell and instabilities.

In chapter III the mathematical formulation of the adjoint methods is given, as well as its numerical implementation. The validation of the adjoint algorithm is described for different cases. Finally, the sensitivity analysis of dual stream under-expanded jet is performed and some physical conclusions are drawn.

Chapter IV investigates the relationship between adjoint-based sensitivity and Uncertainty Quantification analyses. The theory is developed, firstly, for a toy model and then applied to the PSE approach.

The last Chapter associates the PSE solution to an acoustic simulation, based on Ffowcs Williams and Hawkings theory (FW-H) and analyzes wave propagation in the near and far field for a simple test case.

Three appendix describing details about PSE, adjoint PSE and advanced Ffowcs Williams and Hawkings theory are also written.

# Chapter 1

# Introduction aeroacoustics and sensitivity

Aviation has fundamentally transformed society over the past 40 years. The economic and social benefits throughout the world have been immense in 'shrinking the planet' with the efficient and fast transportation of people and goods. The growth of air traffic over the past 20 years has been spectacular, and will continue in the future. As expected, the important progresses in aviation directly exposed to the higher noise levels associated with aircraft operations. Initial attempts to reduce the community noise exposure have included changes in takeoff and approach procedures, development of acoustically treated inlets and mounting jet noise suppressor on the exhaust nozzle. The Federal noise aviation regulations have established noise limits for new airplanes that are significantly lower than previous jet operation levels. More over, the Advisory Council for Aviation Research and Innovation in Europe has estimated then 65% of aircraft noise has to be reduced before 2050. This continuous restrictions on aircraft noise have resulted in considerable acoustics related research and development activities. These activities are focused many investigator toward the identification of the noise generation mechanism of aircraft engines and then to the reduction of the noise at its source trough design innovations, suppression devices or passive/active external controls. In order to obtain a global noise reduction in aircraft noise it is absolutely necessary to study and analyzed the noise produced by jets, since they are one of the most important source of noise component in a modern aircraft. The following of this chapter is based to a collection of different articles and books, to give to the reader a general overview of the mechanism of jet noise and sensitivity analysis.

## 1.1 Jet noise

Research into the jet noise generation and radiation process culminated in the birth of a new field, *Aeroacoustics*, with Sir James Lighthill, Lighthill (1952) [66], widely consider as the mentor of this branch. In the years many progress have been done in term of reduction of noise, the most common way to reduce jet noise in aircraft is to increase the bypass ratio of turbofan engines and very good results have been obtained using this procedure. This bypass ratio has steadily increased over the past 30 years. On the

most recent large engines the bypass ratio exceeds 10:1. However, this trend can not be continued indefinitely due to practical limitations, such as the size and weight of the engine nacelle and this poses new challenges for noise reduction. Other approaches to noise reduction have been pursued like introducing acoustically absorbent material on the interior surfaces, or like using the passive or active manipulation of the boundary layer near the nozzle lip e.g. serrated nozzles or tabs technologies. As explained in Colonius and Lele (2004) [26] the complexity of the nozzle design in modern aircraft engine required a strong sophistication of the theoretical and computational approaches in order to correctly predict noise and to propose new noise controls strategies. Furthermore, the flows that generate the undesired noise are usually nonlinear, unsteady and turbulent. Typically the unsteady flow region contains significant vortex that are eddying motions which also have associated near field pressure disturbances. To conclude, the radiated noise is far smaller than these near field pressure fluctuations. Due to all these considerations and the limitation in terms of power computation of Direct Numerical Simulations of realistic jets a strong theoretical background of this phenomena can be found in literature. The first issue for these researchers was the identification of the source mechanisms that are responsible to noise generation. Since 1960, with the work of Mollö-Christensen and Narashima [83] large scale structures are identified as one of the most important mechanism in the production of noise.

One of the first evidence of instability as source of jet noise can be found in the work of Tam (1971) [121] where a theory based on the concept of instability of the shear layer is developed. his theory prediction shows as the directional sound waves radiated from the shear layer of a supersonic jet are the direct result of instability of the shear layer. In figure 1.1 can be observed the strong directional waves emitted from the shear layer close to the exit of the nozzle [70]. This results are in according to those found in our work when computing sensitivity analysis as explained in chapter 3.

In parallel Crow and Champagne (1971)[27] report the observation of large scale coherent structures in turbulent jet and free shear layers. Since those works, there has been an abundance of papers in the literature devoted to the measurement [79, 78, 57, 43], and to the numerical simulations[121, 122, 133, 134, 98, 102] focused on large scale structures of the turbulence as a dominant noise generation mechanism for jet flows.

Figure 1.2 is a pulsed laser picture where are clearly observed the large turbulence structures in the mixing layer of a supersonic jet with Mach 1.3, Thurow et al. (2003) [126]. This picture is typical of most optical observations of large turbulence structures in a turbulent jet flow and put in evidence the complexity of such a flow. It is shown the evolution of the shear layer along the axial direction.

The turbulence present in the jet, figure 1.2, can be separated in large structures and fine structures. It is now generally accepted that jet noise is created by both fine and large scale turbulence structures. A consistent part of subsonic jet noise is produced by fine scale turbulence, whereas large turbulence structures are dominant noise sources of supersonic and high temperature jets. Figure 1.3 illustrate pressure measurements taken along an arc in the farfield of a jet with an upstream Mach number $M_\infty = 1.5$. These measurements have been Fourier transformed in time $t$ and azimuthal angle $\theta$; the figure 1.3 shows axisymmetric fluctuations (azimuthal wavenumber $m = 0$) of frequency

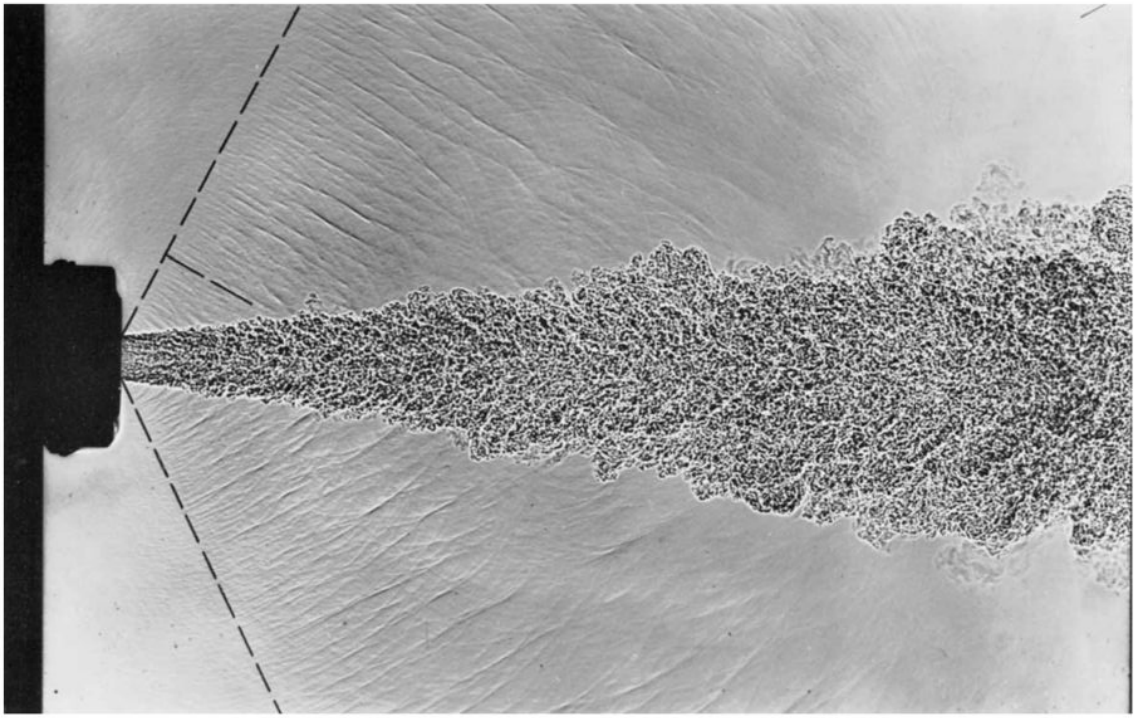

Figure 1.1: Shadowgraphs of a cold supersonic helium jet. Strong directional waves are emitted from the shear layer close to the exit of the nozzle.

$St = 0.25$. The Sound Pressure Levels (SPL) are function of the directivity $\phi$, the radiation peaks is reached at low values of the angles $\phi$ where it is highly directive and as explained above the instability is radiating noise. At higher angles the curve flattens out, a testament to the isotropic nature of radiation in the fine scale of the turbulence. Note that the peak fluctuations in this particular case are almost $25dB$ or 270 times greater in power than those near the sidelines. This directivity is further exaggerated at still higher Mach numbers and diminished at lower values of it.

Moreover, for supersonic jets, just one operative condition exists for which the jet is perfectly expanded and the fluid inside the nozzle reaches the external pressure at the nozzle exit section. In all the other conditions, the jet is incorrectly expanded, figure 1.4(a) and 1.4(b). Tam (1995)[119] gave an exhaustive description of the phenomenon, that in the case of incorrectly expanded jet is characterized by three main components: the turbulent mixing noise, the broadband shock associated noise and the screech tones. In figure 1.5 a typical jet noise spectrum is reported, from which the three contributions are clearly visible. The highest peak is the screech tone, while the weaker noise peak to the left and right of the screech tone are respectively the turbulent mixing noise and the broadband shock associated noise. These three components are generated by different mechanisms and have different relative intensity according to the direction of observation.

The turbulent mixing noise component is generated by both the fine and large scales of turbulence in the flow. It is mainly directed downstream at an angle between 45° and 60°

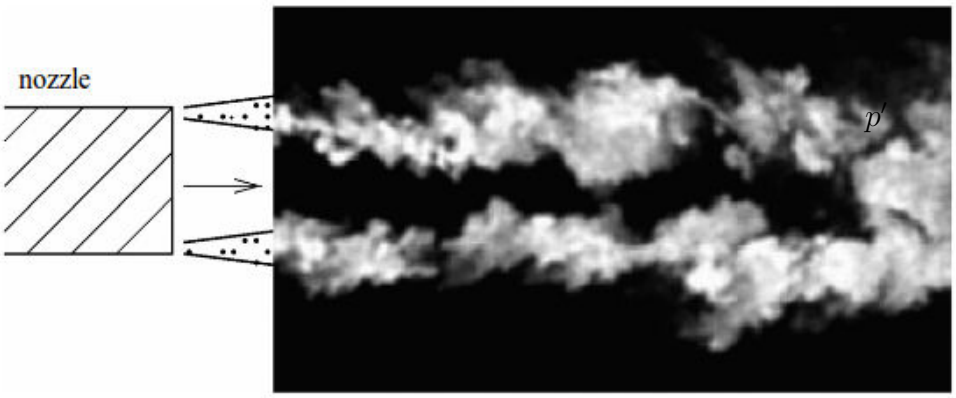


Figure 1.2: Pulsed laser picture of the large turbulence structures in the mixing layer of a Mach 1.3 jet (Thurow et al. 2003). Copyright 2003, American Institute of Physics.

from the jet axis. The upstream weaker contribution is given by the fine scale turbulence, while the dominant component in the downstream direction is emitted by the larger scale, Tam (1995)[119].

The broadband shock associated noise component is predominant in the upstream direction. The peak Strouhal number depends on the radiation direction and several weaker peaks are usually observed, Tam (1995)[119], to the right of the screech tone.

The third component is an intense tonal noise contribution, first observed by Powell [99] in 1953. The main emission is in the upstream direction and usually several harmonics of the screech tone are observed with different directivity patterns. An important characteristic of a jet flow undergoing screech noise emission is the oscillation of the jet, which can be both axial symmetric with toroidal modes and helical with flapping modes [119].

Figure 1.4(a) shows a schematic representation of an over expanded jet with the flow at the nozzle exit experiencing a pressure lower than the ambient value. The velocity difference between the airflow at the nozzle exit plane and the surrounding quiescent air creates a streamwise growing shear layer forming at the nozzle lip. The over expanded air flow from the nozzle exit plane re-compresses due to the higher ambient pressure through a shock cone. The oblique shocks from the nozzle lip first converge on the nozzle axis, where they re-compress the flow, then reflect as expansion waves at the shear layer, re-expanding the jet. This process repeats as a sequence of compressions and expansions. The inflected velocity profile of the shear layer is receptive to disturbances that amplify, developing into large scale instabilities. The resulting shear layer motion makes the shock cell structure inside it unsteady. Shock shear layer interaction results in screech noise being emitted in the surroundings.

Figure 1.4(b) shows the other case of incorrectly expanded jets. This time the under expanded flow from the nozzle exit plane first expands through a fan of expansion waves generated by the surrounding lower ambient pressure, then undergoes a compression through the shock cone created by the refraction of the expansion waves onto the

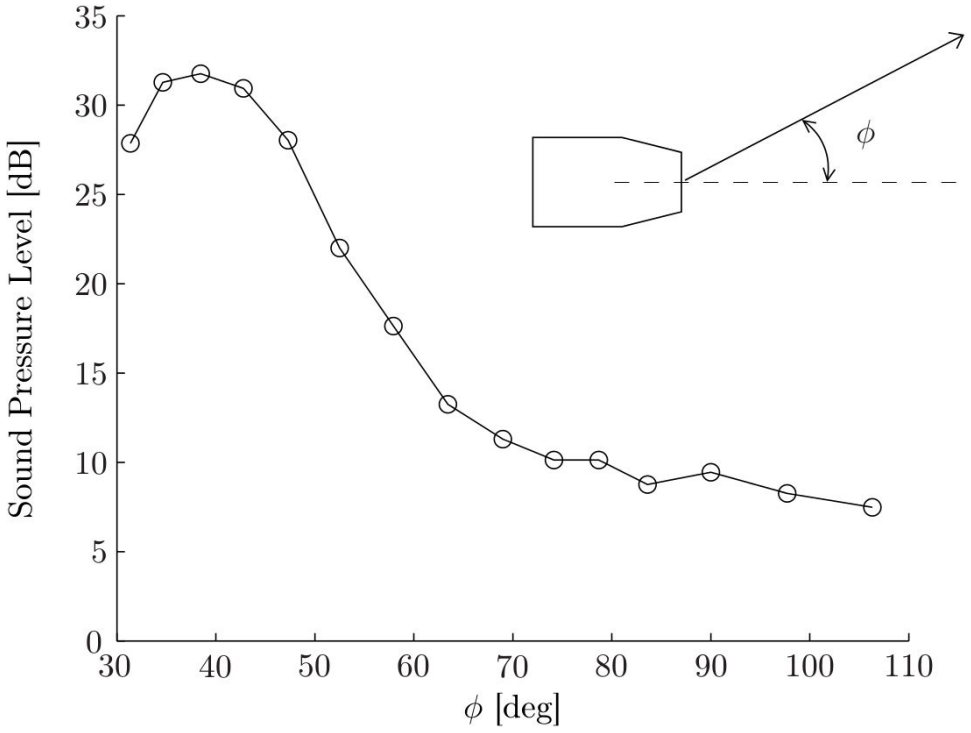


Figure 1.3: Acoustic power measurements of a heated $M_\infty = 1.5$ jet. Azimuthal mode $m = 0$ and frequency $St = 0.25$. Data obtained from measurements of Suzuki and Colonius (2006)[117].

shear layer. Afterwards the process is similar to the one described for over expanded jets, with the flow experiencing a sequence of compressions and expansions.

Summarizing, the problem becomes more complex in case of imperfectly expanded supersonic jet where the noise associated with the presence of shocks has to be taken into account. In this configuration the jet is characterized by a train of shock waves. In the presence of the shock cells, the jets emits two additional components of noise. They are referred to as screech tones and broadband shock associated noise.

Indeed, for those jets sound is generated not only by the interactions between instabilities and the coherent structures in the shear turbulent flows, but also by the weakly non linear interaction between instabilities and shock cell structure, producing shock associated noise Panda et al. (1998)[92]. In the work of Ray and Lele (2007) [103], source terms representing the instability wave/shock cell interaction are assembled and the radiating components have been isolated, providing very good approximation to the full problem. Inspired to this previous work a non local stability approach, presented in chapter 2, is implemented to study these interactions.

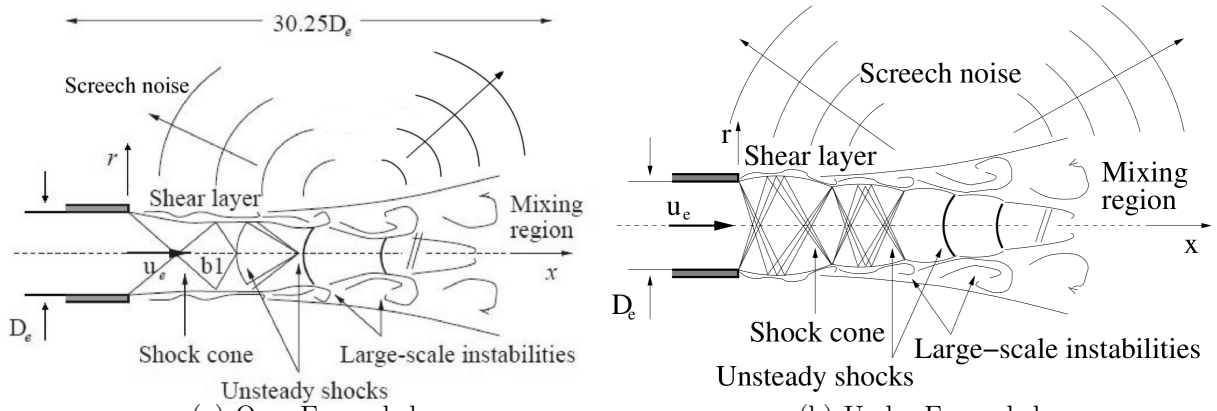


(a) Over-Expanded (b) Under-Expanded

Figure 1.4: Noise radiation in a turbulent jet flow.

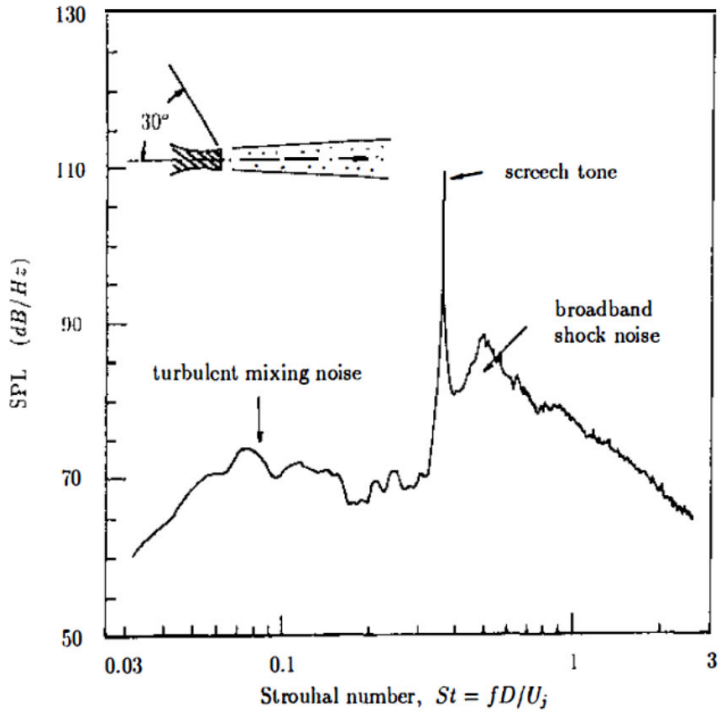


Figure 1.5: Typical far field jet noise spectrum, Tam (1995)[118].

## 1.2 Acoustic analogy

In principle, all the noise properties are included in the flow equations. However, aeroacoustic simulations are often a complex and delicate process to be undertaken, given the number of factors and difficulties to be considered. A comprehensive overview of the numerical requirements for a successful aeroacoustic simulation is given by Tam (1995)[118]. The most important difference between standard aerodynamics problems and aeroacoustic applications lays in the time dependent nature of the noise generation phenomenon, which requires time dependent simulations as well as the storing of a time history of the flow predictions.

The large spectral bandwidth of the disturbances is an important difference between an aerodynamic and an aeroacoustic simulation, which dictates the spatial resolution requirements of the jet. In particular the shortest wavelength (highest frequency) of the sound waves determines this constraint. Besides this, the amplitude of the velocity fluctuations associated with the sound radiation represents another issue. This is usually several orders of magnitude smaller than the amplitude of the turbulent velocity fluctuations from the mean flow, which makes the disturbances far harder to be detected.

The domain size and accuracy requirements are also more stringent compared to aerodynamics and this increases further the computational cost of an aeroacoustic simulation. The sound waves propagate to a long distance compared to aerodynamic disturbances and the computed solution needs to be accurate throughout the entire domain. The dispersive and dissipative characteristics are then critical.

The presence of non linearities in the flow, such as shocks, complicates the scenario further. Tailored boundary conditions are finally needed to prevent the generation of reflection and refraction phenomena at the boundary of the computational domain, which could contaminate the noise estimation with spurious components.

Despite all these reasons, with the increase of computational capacities in the last decades, it became possible to perform unsteady flow simulations (DNS, LES or even unsteady RANS) to reproduce and investigate noise generation. The simulation domain must be sufficiently large to include all the sound sources of interest and at least part of the acoustic near field. Extension to the acoustic far field can then be achieved only by low cost computational methods, such as the linearised Euler equations or wave equation (acoustic analogy). For engineering purposes, the acoustic analogy methods, essentially, consists of separating the acoustic predictions into a source-definition part and a propagation part.

### 1.2.1 General overview

The mathematician Lighthill can be considered the pioneer of the aeroacoustic science, the branch of aerodynamics dealing with the generation of noise by fluid in motion. From his seminal work, Lighthill (1952)[66], many acoustic analogy formulations have been developed. Lighthill's approach is referred to as acoustic analogy, because he established a parallel between sound propagation in a real turbulent flow and an ideal uniform medium at rest. In the latter case, acoustics provides a law which can be simply applied to estimate the radiated sound in real cases. On the other hand, the propagation in a turbulent flow is

a complex phenomenon, which was first addressed by Lighthill. Just a part of the energy content of the flow actually propagates as sound undergoing the conversion between kinetic and acoustic energy and such energy is radiated through pressure waves. For modest speed Lighthill [66] estimated through dimensional analysis the intensity of the radiated sound being proportional to the $8^{th}$ power of a typical velocity in the flow. The sound produced by a turbulent flow interacts with the complex flow structures of different scales and frequencies, giving rise to sound convection and propagation with a variable speed[66], as well as refraction and reflection phenomena. Taking into account all these complexities is not trivial and Lighthill developed a simple concept to tackle them. By rearranging the Navier-Stokes equations he obtained a convenient formulation in the form of a linear wave equation for a uniform medium at rest. Adopting this approach, sound can be considered as if generated in a uniform medium at rest and the noise estimation is reduced to the evaluation of a quadrupole type source term, which appears on the right-hand side of the rearranged equation:

$$T_{ij} = \rho u_i u_j + P_{ij} - c_0^2 \rho \delta_{ij}, \qquad P_{ij} = p\delta_{ij} + \tau_{ij} \tag{1.1}$$

Lighthill assumed that this term, representing applied fluctuating stresses acting upon a uniform medium at rest, is known or can be modelled from the flow field prediction. In Figure 1.6, a turbulent jet flow is compared with the uniform medium at rest in the acoustic analogy approach. The schematic representation of the under expanded jet in figure 1.6(b) shows both the aerodynamic feature of the flow and the noise radiation with downstream and upstream components. In Figure 1.6(a) the same phenomenon of noise radiation is modelled with a volume distribution of quadrupole source terms in the jet shear layer, which reproduces the same acoustic effect of the real flow.

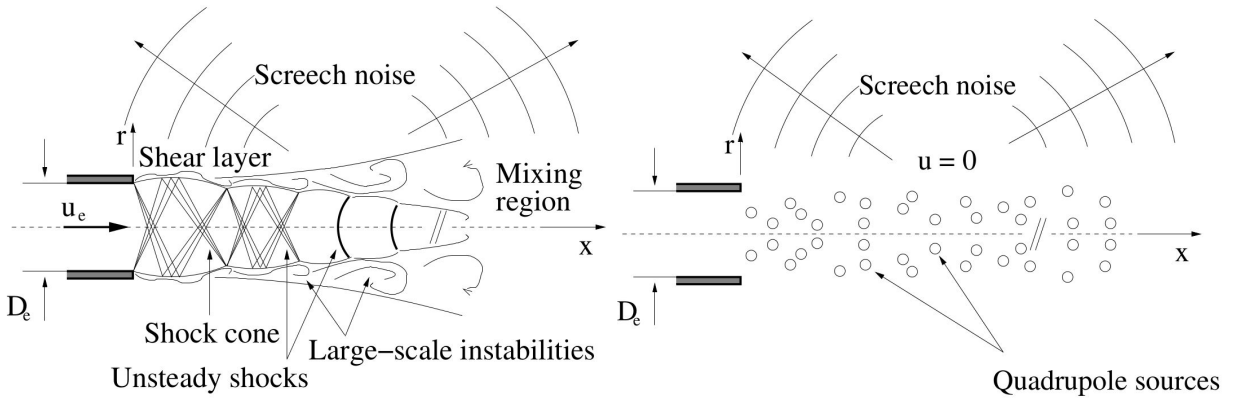


(a) Noise radiation in a real turbulent jet flow

(b) Noise radiation model in an acoustic analogy approach

Figure 1.6: Schematic representation of the acoustic analogy approach.

In this acoustic analogy flow the noise propagates in a uniform medium at rest following the linear wave equation of acoustics. All the effects of the turbulence of the

flow are included in the volume distribution, which takes also into account the non linear characteristics of the flow. Lighthill (1954)[67] addressed directly the turbulence as a source of sound by applying his theory to a subsonic cold jet obtaining results in good agreement with previous experiments. He analysed just low speed effects without developing an extended theory for the effect of source convection. Ffowcs Williams (1963)[34] extended these concepts to account for high speed steady convection of sources. Lowson (1965)[69] investigated the effect of arbitrary convection of multiple noise sources, proving that moving boundaries can be modelled with a surface distribution of dipole sources.

Ffowcs Williams and Hawkings(1965)[35], FW-H, tried to develop a general expression for sources in arbitrary motion convected in a turbulent flow. A considerable complexity neglected by Lighthill is indeed represented by the possible presence of solid boundaries, which definitely occurs in a jet noise test case when we try to model the nozzle lip. Curle (1955)[28] split the influence of rigid bodies to noise radiation into two parts. Firstly, a solid boundary in a turbulent flow produces reflection and diffraction phenomena of the sound generated by the flow itself and modelled by Lighthill with a volume distribution of quadrupole source terms. Secondly, a vibrating surface interacts with the flow by directly applying an external forcing to it. Curle (1995)[28] modelled these two effects with a surface distribution of dipole like sources on the boundaries, which represents the limit of the volume source distribution of quadrupole terms. He developed a formulation to include these effects, by adding to the integral solution proposed by Lighthill a second term in which a surface integration is carried out. This term accounts for the fluctuating forces applied by the vibrating surface upon the flow. In order to include the reflection and diffraction phenomena, he also proposed a modified volume integral term, modelling the effect of the impact on the solid surface of sound waves from the quadrupole distribution. The assumption that Lighthill's stress tensor expressed in equation 1.1 is known from the flow field prediction is true in many simple cases and Lighthill's theory can be used to estimate the radiated sound. Nevertheless, in many applications this estimation is not trivial bringing doubts on Lighthill's analogy feasibility. Several researchers tried to undertake a different approach in order to get more accurate predictions of the radiated noise for flows of interest in aerodynamic engineering applications. An important development was to derive an inhomogeneous moving media wave equation for the sound generation process, instead of considering a uniform medium at rest. With this approach, results were obtained by Phillips (1960)[96] and Lilley (1974)[68]. The complexity of the formulation increases in this development, but the analytical cost is compensated by not requiring the estimation of the Lighthill source field term (eq. 1.1) to be estimates, as it was in his first acoustic analogy theory. Keeping in mind that in many real cases this estimation is hard or not feasible, the results of using an inhomogeneous moving media wave equation tended to be more accurate. Following the approach stated by Lilley (1974)[68] and developing it, Goldstein (2002)[41] tried to find a more general formulation, pursuing a more sensitive method, able to relate even small modifications in the flow to their effect in the sound generation and propagation. One year later, Goldstein (2003)[40] formulated a generalized acoustic analogy theory, which takes into account the importance of the fluctuating component of the velocity field in the mechanism of noise radiation. The result is a general set of Linearised Inhomogeneous Euler equations (LIE).

### 1.2.2 Computational Aeroacoustics (CAA) simulation

The origin of Computational Aeroacoustics (CAA) can be dated back to the middle of the 1980s, with a publication of Hardin and Lamkin (1984)[46]. Few years later the same authors introduced the abbreviation CAA. The term was initially used for a low Mach number approach (Expansion of the acoustic perturbation field about an incompressible flow). Later in the beginning 1990s the growing CAA community picked up the term and extensively used it for any kind of numerical method describing the noise radiation from an aeroacoustic source or the propagation of sound waves in an inhomogeneous flow field. Mankbadi et al. (1994)[75] discussed the application of direct CAA simulation to supersonic jet aeroacoustics compared to a Lighthill's analogy approach. He found the direct CAA simulation more computational expensive in order to get the sound field predictions. He also pointed out the difficulties of the Lighthill acoustic analogy in dealing with acoustically non compact sources. Di Francescantonio[36] and Lyrintzis[73] also argued the direct CAA computation not to be an appropriate method for the standard distance between source region and observer positions in most of the real applications. However, when the geometry of the problem does not allow the direct estimation of the pressure fluctuations on the observer positions, an integral method is required to project the solution onto the acoustic far field. Furthermore, the separation between the aerodynamics and aeroacoustics simulation usually offers the possibility of a better insight of the problem and the use of different physical models describing the flow in regions where the flow does follow different laws.

### 1.2.3 The FW-H acoustic analogy

Ffowcs Williams and Hawkings (1965)[35] developed an acoustic analogy formulation modelling the noise radiation with three kinds of different sound sources, i.e., monopoles, dipoles and quadrupoles, in order to take into account the different aspects of a significantly heterogeneous phenomenon. The FW-H equation and integral solutions are reported in Chapter 4. Ffowcs Williams and Hawkings [35] obtained a generalized inhomogeneous wave equation (eq.1.2) by introducing the use of the generalized function theory, which represented an important turning point in the acoustic analogy historical development.

$$\Box^2 \left\{(\rho - \rho_0)c_0^2 H(g)\right\} = \frac{\partial^2 \left\{T_{ij} H(g)\right\}}{\partial x_i \partial x_j} - \frac{\partial \left\{L_i \delta(g)\right\}}{\partial x_i} + \frac{\partial \left\{Q \delta(g)\right\}}{\partial t}, \tag{1.2}$$

where $H(g)$ is the Heaviside function, in the first source term on the right-hand side $T_{ij}$ is the Lighthill stress tensor and $\delta$ is the Dirac delta function.

All details are given in chapter 4. The FW-H equation introduced the new concept of an unbounded fluid, which is defined everywhere in space. The unbounded fluid follows the real motion (modelled by the Navier-Stokes equations) on and outside a fictitious surface that can be taken as coincident with a solid boundary. Inside the surface the conservation laws are assumed not to apply and the flow state can be defined arbitrarily, so generating a discontinuity at the surface itself. In order to maintain this discontinuity

mass and momentum sources are distributed on the integration surface and they act as sound generators. The strength of this mass and momentum source distribution is given by the difference between the flux requirements in the two regions in which the FW-H surface splits the flow. This acoustic analogy, that is a generalization of Lighthill's one, gave birth to a more applicable and reproducible model, which still appears in many recent formulations. The generalized function theory has been widely used in the aeroacoustic field after Ffowcs Williams and Hawkings and it is developed with a rigorous mathematical approach by Farassat (1994)[31]. Farassat (1975)[30] applied the FW-H acoustic analogy to helicopter rotors showing the power of the theory in predicting aerodynamic sound in the presence of moving surfaces in an unsteady turbulent flow even for non compact source problems. The embedding procedure, which converts the standard fluid dynamic problem to an unbounded fluid case through the use of the generalised function theory, is detailed.

In computational simulations, the FW-H acoustic analogy's main disadvantage is the need to perform a volume integration that is far more expensive than a two dimensional numerical integration. However, the quadrupole source term is usually some order of magnitude smaller than the surface source distribution and in many applications it is neglected, as in Di Francescantonio (1997) [36]. In the case this assumption is not valid, an increase in the computational cost inevitably occurs. Thanks to the increasing computational power, numerical applications including a volume integration have recently been developed by Brentner (1997)[17].

### 1.2.4 The porous FW-H formulation

Di Francescantonio (1997) [36] proposed the use of a FW-H acoustic analogy with a permeable surface, trying to combine the advantages of Kirchhoff's method and the FW-H acoustic analogy. He therefore referred to the new equation as Kirchhoff FW-H (KFWH), pointing out that the main advantage was that no derivatives of CFD quantities were required as in the standard Kirchhoff's formula. The KFWH equation was used by Di Francescantonio[36] neglecting the volume source distribution. By considering a surface placed in a linear region, the Kirchhoff method speed up is recovered. However, the general form of the KFWH equation included a volume integration to take into account possible non negligible quadrupole sources outside the permeable surface.

### 1.2.5 Advanced time vs retarded time

A retarded time equation of the type of equation 1.3 is usually solved for the estimation of the retarded time.

$$\tau_{ret} = t - \frac{|\boldsymbol{x} - \boldsymbol{y}(\tau_{ret})|}{c_0} \tag{1.3}$$

Equation 1.3 expresses that a disturbance emitted from the source position $\boldsymbol{y}$ at time $\tau_{ret}$ will reach the observer $\boldsymbol{x}$ at time $t$, due to the time of flight of the noise propagating at

the speed of sound $c_0$. Two different approaches can be adopted to take into account this propagation of the disturbances. In the retarded time approach the simulation runs in the observer time, meaning that the simulation time axis is representative of the reception phenomenon. In this case an implicit retarded time equation needs to be solved. Different disturbances reaching the observer at the same time can be emitted at different retarded times. A different approach was proposed by Casalino (2003)[19]. In this case the simulation runs in the emission time and, for each different disturbance, an advanced time is calculated for a specific observer. This represents the time of flight for the disturbance to travel from the emission to the reception point. Casalino used the definition of advanced time analysing the differences between the two approaches. He pointed out the advantages of the advanced time formulation in the possibility to run the aeroacoustic prediction simultaneously with the CFD simulation. Furthermore he showed that the advanced time can be explicitly estimated by an algebraic equation with no iterative method required.

### 1.2.6 A convective FW-H acoustic analogy

Most of the FW-H acoustic analogy formulations assume the propagation of sound waves in a medium at rest as in Lighthill's original assumption. A usual way to take into account a moving medium relative to a fixed observer is to circumnavigate the problem, considering a case in which the observer moves in a medium at rest[32]. In 2011 Najafi-Yazdi et al. [90] developed an interesting convective formulation of the FW-H acoustic analogy explicitly taking into account the presence of a mean flow. In such a formulation the standard wave operator is modified to obtain a convective wave operator. A uniform convective velocity is considered directly in the equations originating additional terms compared to the standard FW-H equation. A convective Green's function suggested by Blokhintsev is also adopted to take into account the mean flow, rather than the free space Green's function for a medium at rest (1994)[31]. A Lagrangian derivative appears in the thickness noise, which is slightly different from the FW-H integral solution. A clear Doppler effect caused by the mean flow is showed in the results from elementary source applications.

### 1.2.7 Alternative aeroacoustic techniques

#### a- The Kirchhoff formulation

The Kirchhoff formula was first published in 1883[60]. Later on, Lyrintzis (1994)[72] published a review of the application of this theory in the aeroacoustics field, referring to the methodology as a surface integral method[73]. The basic concept of the method is the use of a control surface on which pressure and its normal and time derivatives are estimated by numerical method. The acoustic pressure in the far field can then be obtained from an integration on this control surface of the above mentioned quantities. The control surface is required to enclose all the non linearities of the flow and the noise sources. The position of the control surface is critical, because the noise propagation on the surroundings is assumed to follow the linear wave equation. Consequently, the surface needs to be placed in a region of the flow where the linear wave equation is valid

and this method does not allow the presence of non linearities on and outside the control surface. On the other hand, the volume integration carried out in the acoustic analogy method to take into account non linearities gathered in the quadrupole source term is not necessary. This translates to an improvement of the computational speed. The first formulation, Kirchhoff (1983)[60], was limited to stationary control surface integration. Morgans (1930)[87] extended the use of the method to moving control surfaces introducing the use of the Green's functions in this integral method. Ffowcs Williams and Hawkings[35] derived a general formulation to deal with the effect of arbitrarily moving surfaces on the generation of sound. Despite the generalization obtained, their modification to the original theory presented some numerical complication for the time and space derivatives being taken in the observer reference frame. Hawkings (1979)[47] applied the Kirchhoff formula to a transonic open rotor introducing the idea of using a surface surrounding the rotating blades, which follows the helicopter moving at the flight forward speed. Farassat and Myers (1988)[33] found a formulation, which prevents the numerical issue of evaluating space and time partial derivatives in the observer reference system, by bringing these derivatives in the source frame and their development is more feasible from a computational viewpoint. They showed [33] that their development represented a more general formula applicable to deformable and rigid piecewise smooth moving surfaces and including the original formula [60] for stationary surfaces as a special case. An extended Kirchhoff method is proposed by many authors by including additional non linearities in the region outside the control surface, where a volume integration is required [73]. An example is given by Pilon and Lyrintzis (1998)[97], who applied the methodology to supersonic jets. Mitchell et al. (1999)[82] applied a Kirchhoff surface integral method with a stationary surface in a jet noise problem. Application of the moving surface with uniform velocity can be found in Morris et al. (1998)[89] and Lyrintzis and Mankbadi (1996)[74]. Di Francescantonio (1997)[36] proposed the use of the FW-H acoustic analogy with a permeable surface (porous FW-H) not coinciding with a physical surface and compared it with the Kirchhoff surface integral method. Brentner and Farassat (1998)[16] followed this approach by comparing the use of the Kirchhoff formula for moving surfaces to the porous FW-H acoustic analogy, showing that the latter is more conveniently applicable to aeroacoustic problems and that it embeds the Kirchhoff formulation as a special case. In the Kirchhoff formulation all the non linearities of the flow are included in the surface integration on a fictitious surface, so called the Kirchhoff surface. This feature avoids a volume integration which is usually far more expensive from a computational viewpoint than a two dimensional one. This advantage is also available in the FW-H acoustic analogy, if the FW-H surface is thought as penetrable or permeable[16]. On the other hand, the FW-H acoustic analogy has the advantage of better representing the physics of the problem and the various terms in the formulation can be easily interpreted. Furthermore, it offers a more robust approach and it is easier to be interfaced to CFD codes[16]. Lyrintzis (2003)[73] also argued that the porous FW-H equation method is equivalent to Kirchhoff's method, representing a preferable alternative given the current state of the art of numerical development. Even though the porous FW-H requires larger memory usage, it is less limiting in the control surface choice and it does not require normal derivative estimation.

**b- Theory of vortex sound**

Powell (1964)[100] first proposed the theory of vortex sound, which follows a different conception from the acoustic analogy and represents an alternative approach in aeroacoustics, to which many authors have contributed. Powell argued that both the hydrodynamics and the acoustics of the flow are governed by vorticity fluctuations in low Mach number turbulent flows and the acoustic sources are associated with limited regions of flow in which the vorticity vector is non vanishing, rather than the whole hydrodynamic field as in Lighthill's theory[66]. Howe (1975)[54] tried to develop a revised formulation of Lighthill's acoustic analogy able to deal with problems characterized by extended region of non uniform flow, in which Lighthill's propagation in a uniform medium at rest assumption would not be applicable. He proposed the stagnation enthalpy as acoustic variable, individuating the source terms of such acoustic variable as confined in regions of non vanishing vorticity and entropy gradient[54], so developing a revised version of the vortex sound, Howe (2003)[55] gives a complete and exhaustive explanation of the vortex sound theory, defining it as the branch of fluid mechanics dealing with the conversion between rotational kinetic energy in a turbulent flow and longitudinal disturbances corresponding to sound waves. He argued that Lighthill's equation can be rearranged by showing the importance of the vorticity in the sound production[55]. To do so, the total enthalpy is chosen as the fundamental acoustic variable instead of the Lighthill acoustic density fluctuation. This new acoustic variable can be introduced by using Crocco's form of the momentum equation, differently from Lighthill's derivation. The justification in the use of total enthalpy as acoustic variable comes from the consideration that, in steady irrotational flows, such a variable is constant. Consequently, at large distances from the acoustic sources, a perturbation in total enthalpy represents an acoustic wave[55].

## 1.3 Instability models of large scale coherent structures

A natural consequence of the presence of coherent structures is to modeled them as instability waves. First stability analysis of steady solutions of the conservative equation of motion (N-S equations) date backs to the early 1892, Rayleigh[104]. Rayleigh focused his attention in the previous work of Reynolds where experiments[105] did in a pipe flow showed the presence of laminar, regular patterns. Rayleigh investigated the instability of the flow in a pipe, referring to the non viscous Euler equations. Later work included viscosity in an attempt to determine the critical Reynolds number for laminar turbulent transition, and the field of hydrodynamic stability has greatly developed.

The model essentially consist on a decomposition of the total flow vector $\boldsymbol{Q}(\boldsymbol{x},t)$, function of the time, $t$, and the spatial coordinates, $\boldsymbol{x}$, into a base flow $\bar{\boldsymbol{q}}(\boldsymbol{x})$ and a small perturbation $\boldsymbol{q}'(\boldsymbol{x},t)$. The base flow is supposed to be steady and the temporal fluctuations are described by the perturbation $\boldsymbol{q}'(\boldsymbol{x},t)$:

$$\boldsymbol{Q}(\boldsymbol{x},t) = \bar{\boldsymbol{q}}(\boldsymbol{x}) + \boldsymbol{q}'(\boldsymbol{x},t) \tag{1.4}$$

Those fluctuations, following the methods of normal modes, are composed of an exponential like wave term and a shape function. In the particular case of an axisymmetric jet, with cylindrical coordinates $\boldsymbol{x} = (x, r, \theta)$, the perturbation $\boldsymbol{q}'$ propagating in the $x$-direction can be written as:

$$\boldsymbol{q}' = \boldsymbol{q}(x, r) \exp\left(i\Theta(x, \theta, t)\right) \tag{1.5}$$

In the above equation $i$ stands for the square root of $-1$, $\boldsymbol{q}(x, r)$ is the amplitude function, or shape function, and $\Theta$ a general phase function. Typically in the Kelvin-Helmholtz (K-H) instability owes its origin to the inertia of the fluids, viscosity does not play an important role, otherwise the inflection points of the mean velocity profile has a crucial importance in the instability of such a flow. More details about hydrodynamics instabilities could be found in Godrèche et al [39].

As explained in the thesis of Cavalieri (2012)[20], the validity of the linearisation of the Navier-Stokes (or Euler) equations can only be shown a posteriori, based on the eventual agreement with an experiment. This has been the case for a number of works in the literature; an example is the linear behaviour of the evolution of coherent structures over a region extending several jet diameters, as observed by Crow and Champagne's (1971)[27] and by Moore's (1977)[86] and shown in figure 1.7. In what follows, we review some of the computations that have been done on instability theory for jets and some experimental measurement that confirmed the validity of such approach for turbulent flows.

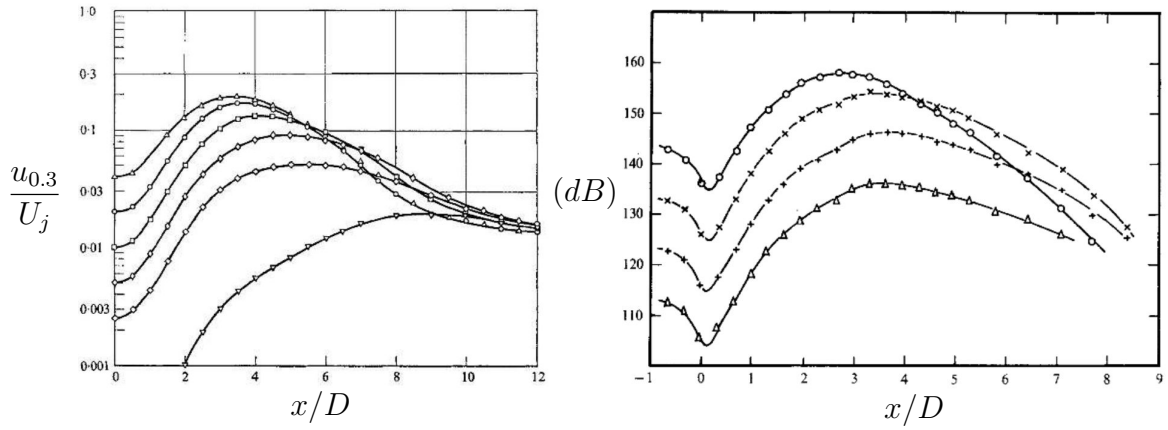


Figure 1.7: Linear and nonlinear behaviour of forced jets in (a) Crow and Champagne's [27] and (b) Moore's[86] experiment. Forcing Strouhal numbers are 0.3 for Crow and Champagne and $\simeq 0.48$ for Moore. The lines from bottom to top refer respectively to increasing forcing amplitudes at the nozzle exit. The triangles in Crow and Champagne's experiment refer to the unforced jet

### 1.3.1 Linear stability theory (LST)

#### a- Theoretical introduction

This spatial theory is based to the local parallel assumption of the flow which yields:

$$\boldsymbol{q}' = \boldsymbol{q}(r)\mathrm{e}^{(i(\alpha x + m\theta - \omega t)} \tag{1.6}$$

where $\alpha$ and $m$ are the wavenumbers in the streamwise and azimuthal direction, respectively; $\omega$ represents the frequency of the perturbation. The complex amplitude of the perturbation $\boldsymbol{q}(r)$ depends only on the radial coordinates. In the frame of spatial theory $\alpha$ is a complex value while $m$ is en integer number and $\omega$ is real. Substituting 1.6 into the Linear Euler Equation, LEE, the system could be rewritten as a classical Ordinary Differential Equation, ODE, function of the pressure shape function $p(r)$, known as the non viscous axysimmetric Pridmore-Brown equation:

$$\frac{d^2p}{dr^2} + \left(\frac{1}{r} - \frac{1}{\bar{\rho}}\frac{d\bar{\rho}}{dr} - \frac{2\alpha}{\alpha\bar{u}_x - \omega}\right)\frac{dp}{dr} + \left(\bar{\rho}M^2(\alpha\bar{u}_x - \omega)^2 - \frac{m^2}{r^2} - \alpha^2\right)p = 0 \tag{1.7}$$

that written in a compact way gives:

$$\mathcal{L}(p) = 0 \tag{1.8}$$

Associated to homogeneous boundary conditions, Tam and Burton (1984)[123] , this system corresponds to an eigenvalue problem with streamwise wavenumber $\alpha$ as the eigenvalue and $\boldsymbol{q}(r)$ as the associated eigenfunction. The eigenvalue problem must to be solve by satisfying the dispersion relation:

$$D(\alpha, m, \omega) = 0 \tag{1.9}$$

The growth rate of the disturbance, $\sigma$, is given by:

$$\sigma = -\alpha_i \tag{1.10}$$

where subscript $i$ refers to the imaginary part of the quantities. A disturbance is stable, neutral or unstable if its growth rate is less, equal or greater then zero, respectively.

**b- Some results (for parallel base flows)**

Preliminary studies of LST apply to the jet and free shear layer are based to work of Crow and Champagne (1971)[27] when it was discovered the presence of large turbulence structures in jets and as well their main role as jet noise sources. Morris (1976)[88] studied the spatial linear stability of axisymmetric ($m = 0$) and helical ($m = 1$) jets. The flows are assumed to be incompressible and viscous, analyzed from the exit of the nozzle to the fully developed turbulent region. An accurate numerical method is proposed to solve the eigenvalue problem and are computed for three different mean velocity profiles. The results show as the axial position where the instability is maximum increase if the frequency decrease. It was also observed that only the helical mode, $m = 1$, will continue to amplify in the developed jet flow. In the work of [81] a LST was performed for a round supersonic jet. In a axisymmetric inviscid jet the influence of the spatial growth rate and disturbance phase velocity is studied. The base flow is considered as a parallel

flow which is infinite upstream and downstream, with radial velocity equal to zero. The author found that flow becomes more stable if the free stream Mach number increase. The good agreement if compared with experimental results[27] confirmed that instability of turbulent jet approximately follow the spatial linearised theory.

The first original description of these coherent structures as statistical instability waves was proposed by Tam and Chen (1979) [124]. This work is based to the fact that large turbulence structures are somewhat more deterministic than the fine scale turbulent motions, moreover comparison with experimental results is made and very favorable agreement is found. In particular, this work point out several difficulties of the comparisons between theoretical and experimental results due to the high influence of the initial condition and to some upstream disturbances that could influence the not fully developed mixing layer. The most important assumption of this model is that the turbulent jet flow spreads out very slowly in the streamwise direction, consequently the flow variables change very slowly as well. This means that, i.e., the turbulence statistics are nearly constants locally. Indeed the flow is stochastically stationary in time and in the axial flow direction. For a system in (quasi) dynamical equilibrium, statistical mechanics theory can be represented mathematically by a superposition of its normal modes. In the case of high speed jets, the large scale fluctuations are the statistical mechanism while the dominant normal modes are the instability wave modes of the mean flow, computed using LST.

Very few works can be found in literature regarding LST for dual stream jets. Perrault-Joncas et Maslowe (2008)[95] applied the LST to a subsonic compressible coaxial jet. The computation have been done with two different mean flow, one with "cold" temperature profile is taken from Papamoschou's experiments[93] and one with "hot" temperature profile is taken from the mean data of a typical turbofan engine. They work has not comparison with experimental results, but their parametric studies show the influence of the diameter ratio, compressibility, azimuthal wavenumber and the ratio between of the two mean velocities in the stability of the jet.

Concluding, large scale structures are an important source of noise and linear instability is the first step in their formation.

### 1.3.2 Parabolized Stability Equations

All the cited works were based on the parallel flow hypothesis. An improvement on the approximations of spatial stability can be done with the assumption of a base flow evolving slowly in the streamwise direction. Herbert (1993)[49] developed the Parabolized Stability Equations (PSE) theory to consider the non parallel effect of the flow in the instability waves in the boundary layer region, inspired by the multiple scale methods.

The fundamental assumption of the PSE theory is that the disturbances consist of a fast oscillatory part and an amplitude that varies slowly in the streamwise direction. The decomposition into fast and slow variations aims at a set of equations that is "almost" parabolic in the streamwise coordinates direction and is suitable to a numerical marching procedure. In this work starting with the Euler equations which are not parabolic in space, appropriate approximations are called for to ensure the removal of elliptic components. Once these approximations are carried out, the Parabolized Stability Equations, PSE,

can be solved as a fraction of the computational costs of Direct Numerical Simulation, Large Eddy Simulation etc, but still conserving a good accuracy in the results. Finally, thanks to the contribution of many investigators [61, 42, 106, 107] it's now known that Parabolized Stability Equations are a powerful tool for the prediction of subsonic and supersonic jet noise.

### a- Theoretical introduction

PSE approach is now well known and applied in various stability problems. Several advantages can be shed on light. Indeed, contrary to the Linear Stability Theory (LST) where local parallel flow is assumed, they take into account of the small streamwise variations of the base flow and of the disturbances directly in the formulation. Since PSE are mathematically PDE, it is simple to solve them by adding various boundary conditions and source terms. This leads to use them for receptivity and sensitivity analysis [7], in optimal flow control approaches [5] and for weakly nonlinear stability studies[50].

In the following, all the variables are made non-dimensional. The characteristic length is based on the nozzle diameter and the characteristic flow properties are chosen to be those of the flow on the axis at the nozzle exit [98].

The small perturbation $\boldsymbol{q}'$ is assumed to have a wave like exponential term $\exp(i\Theta)$ rapidly varying in the $x$-direction and an amplitude function $\boldsymbol{q}(x,r)$ that varies slowly as:

$$\boldsymbol{q}' = \boldsymbol{q}(x,r)e^{i\Theta}, \quad \text{with} \quad \Theta = \int_{x_0}^{x} \alpha(\xi)d\xi + m\theta - \omega t, \tag{1.11}$$

where $\alpha(x)$ is the complex axial wavenumber (spatial theory), $m$ is the fixed integer azimuthal wavenumber, $\omega$ is the fixed angular frequency of the disturbance, $x_0$ is the inlet of the computational domain and $t$ is the time. The imaginary part, $\alpha_i(x)$, can be defined as a growth rate and $2\pi/\alpha_r(x)$ corresponds to a spatial wavelength.

The decomposition is introduced into the linearised Euler Equations (LEE) and the PSE are derived using the assumption of small streamwise variations of $\alpha$, of $\boldsymbol{q}$ and of the based flow quantities:

$$L_{PSE}\ \boldsymbol{q} = \boldsymbol{0}, \tag{1.12}$$

with

$$L_{PSE} = i\alpha A_1 + imA_2 - i\omega A_3 + B + A_1\frac{\partial}{\partial x} + A_0\frac{\partial}{\partial r},$$

where $A_0$, $A_1$, $A_2$, $A_3$, $B$ are matrix operators defined by the mean-flow properties and they are described by Ansaldi and Airiau (2015) [11]. From equation (3.13) it can be noticed that the streamwise change of the disturbance can be described by the product of the amplitude function and of the exponential term. This ambiguity must be resolved by the introduction of an additional equation, called normalization or closure relationship, which imposes that the growth of the disturbance is absorbed by the wave function part of the decomposition, making sure that the shape function $\boldsymbol{q}(x,r)$ stays with a slow variation in $x$ [50]. We set:

$$\mathcal{N}(\boldsymbol{q}, x) = \int_0^\infty \boldsymbol{q}^h \frac{\partial \boldsymbol{q}}{\partial x}\ r\ dr = 0, \tag{1.13}$$

where the superscript $h$ denotes the transpose conjugate. The system with the unknown $(\boldsymbol{q}, \alpha)$ is only quasi parabolic because a residual ellipticity due to the normalization condition and a streamwise pressure gradient term remains, see Airiau and Casalis (1993)[6], and Andersson et al. (1998)[8].

### b- Some results

PSE used to calculate the instability waves were introduced by Herbert and Bertolotti[51, 48, 49], they were focused on the study of instability in boundary layers. Tam and Burton (1984) presented a theory based to PSE approach and Yen and Messersmith (1998)[133] applied the PSE approach to the prediction of instabilities in a incompressible, isothermal, round jet. Results show as PSE is capable to well capture the physical evolution of the instabilities over the streamwise domain until the end of the potential core; outside of the potential core, where the shear layer is fully developed, the PSE are less capable of supporting the like wave model. In the same period, PSE have been used for prediction of instabilities and noise in supersonic jets[14, 134] by coupling PSE equations with a solution of the wave equations in the far field; good agreements were found between the computed and the measured Sound Pressure Levels (SPL), see figure 1.8.

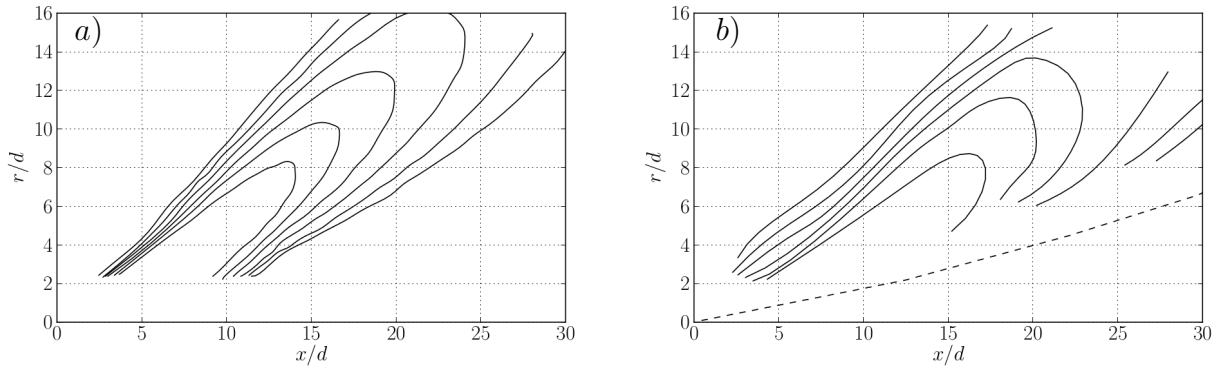


Figure 1.8: Comparison between SPL obtained by Balakumar (a) computing the wave equation for fixed Strouhal number, $St$, and azimuthal wavenumber $m$ with experimental results (b) measured by Troutt and McLaughlin[129].

One more important consideration, in according to the experimental observations, is that the majority supersonic jet noise is produced in the first few diameters to the exit of the nozzle. Piot et al (2006)[98] have compared the results obtained by solving PSE and by solving Large Eddy Simulation (LES) for two different jet with Mach number 0.7 and 2 respectively. The results show that PSE predicts very well the spatial growth of the disturbances. However, at least for this work, PSE does not predict correctly the noise radiation as LES approach for the subsonic case, maybe in this configuration K-H

instability waves has not an important role in the production of noise. The agreement is very good when compare the supersonic case, showing the crucial role of K-H instabilities in supersonic jets. Also in this work to compute the acoustic pressure from the PSE results, the wave equation have been solved and again the noise sources is concentrated near the jet exit.

More recent works have focused attention of the non linear effect of the instability waves. A natural approach to investigate the non linear effect is to compute the Nonlinear PSE equations (NPSE). A very good analysis of the non linear effects of the instability waves in terms of noise radiation have been successfully made by Cheung and Lele (2009)[24]. Three jet configurations are tested, one supersonic and two subsonic; actually non linear approach may capture the sound generation process more accurately then the linear instability theory.

Ray and Lele (2007)[103] take into account the weakly nonlinear interaction between linear instability and shock cell structure in under expanded supersonic jet. Figure 1.9 shows the results obtained by Linear Euler Equation (LEE) computation in the far field and PSE shock cell interaction model.

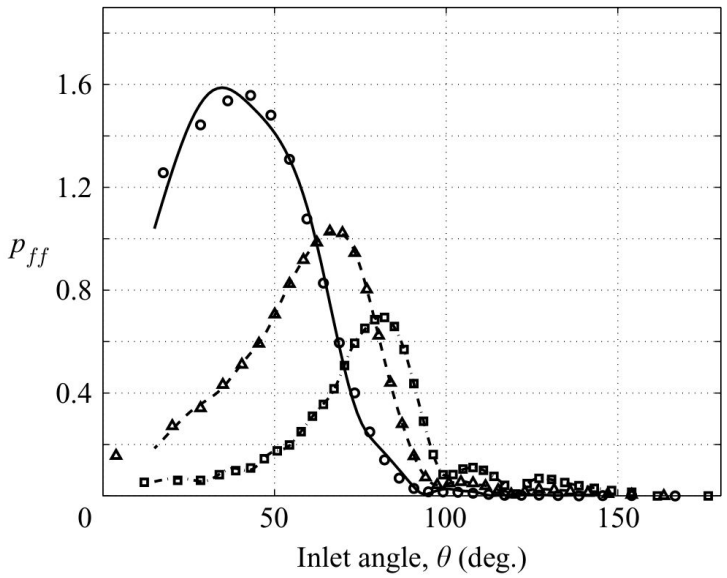


Figure 1.9: Shock noise test case, $Mj = 1.22$, $m = 0$. The curves represent the far field pressure amplitude, $p_{ff}$, computed by LEE solutions at different Strouhal number and symbols represent PSE/shock cell model solutions, Ray and Lele (2007)[103].

The evolution of instability for coaxial jet using PSE approach has been taken into account in the work of Léon and Brazier (2011)[64]. The hydrodynamics unstable modes are computed using the non local approach and is coupled with Kirchhoff surface technique to predict noise in the far field. Low frequencies instabilities waves for both mixing layer are taken into account focusing to the first two azimuthal modes, $m = 0$ and 1. The instability waves grown in the external shear layer appears as the most unstable one and dominate the hydrodynamic region of the jet. Then because of the lack of the PSE in the

prediction of noise in the far field, the model is coupled with a acoustic wave propagation. Results are compared with experiment and with LES computation obtaining encouraging results. Recently, PSE approach applied to LES computation of a subsonic dual stream jet illustrate very well the propagation of the instability in the inner and outer shear layer. A parametric study of different Strouhal and azimuthal wave number for the two unstable modes (one in the primary and one in the secondary shear layer) has been performed, Sinha et al. (2016)[111]. In this work is well presented the problem of PSE for dual stream jet, in fact PSE can not well distinguish between the two unstable modes if their complex wavenumbers are to similar, or if one stabilize during the streamwise marching, but the other stay unstable.

Finally, with the work of Sinha et al (2014) [112] that demonstrate the validity of linear instability to predict the average wavepacket evolution in supersonic jet inside the potential core, leads to the conclusion that large scale structure manifest in the subsonic and supersonic jets and its evolution is well predicted inside of the potential core of the jet.

### c- Non linear PSE

Also if in this thesis we only treated linear PSE problem a briefly introduction of non linear PSE approach is done in this section. In the linear PSE approach described above, the disturbance amplitude is assumed to be infinitesimally small so that the non linear interaction of waves with different frequencies and azimuthal wave numbers is neglected. When finite amplitude waves are present in the flow, the linear approach is no longer valid. For non linear studies, we assume that the total disturbance is again periodic in time and in the azimuthal direction, thus, the total disturbance function $\boldsymbol{q}'$ can be expressed by the following Fourier series[29, 63].

$$\boldsymbol{q}' = \sum_{n=-N}^{N} \sum_{m=-M}^{M} \boldsymbol{q}_{m,n}(x,r) e^{\,i\left(\int_{x_0}^{x} \alpha_{m,n}(\xi)d\xi + m\theta - n\omega t\right)} \tag{1.14}$$

where $\alpha_{m,n}$ and $\boldsymbol{q}_{m,n}$ are the Fourier components of the streamwise wave number and shape function corresponding to the Fourier mode $(n\omega, m)$, while, $M$ and $N$ are the total number of modes kept in the truncated Fourier series. Notice that the frequency $\omega$ and the wave number $m$ are set as the smallest values, respectively. Because of the characteristic symmetry of a jet flow only a quarter of modes ($m$ ranging from 0 to $M$ and $n$ ranging from 0 to $N$) are computed in the marching process. Finally, similar to the Linear PSE approach, an additional closing equation is imposed for each mode $(n\omega, m)$. These last equations ensure the hypothesis of small variations of each shape function $\boldsymbol{q}_{m,n}$ in the streamwise direction.

$$N_{m,n} = \int_0^{\infty} \boldsymbol{q}^h_{m,n} \frac{\partial \boldsymbol{q}_{m,n}}{\partial x}\, dr = 0 \tag{1.15}$$

### 1.3.3 Convective and absolute instability

The distinction between convective and absolute instability has to be done. We are looking to a simple criterion that allows us to determine, based to an unstable flow, whether it is convectively or absolutely unstable. If the localized disturbance generated by the impulse spreads both upstream and downstream of the location where it originated, the flow is considered absolutely unstable. In case the disturbance is swept downstream or upstream of the source, the flow is convectively unstable. This characterisation for parallel base flows can be made based on the impulse response of the flow, as reviewed by Huerre and Monkewitz (1990)[56]. Cold (unheated) jets, such as the ones studied in this thesis, are convectively unstable, but sufficiently heated jets may present absolute instabilities. This was shown theoretically by Monkewitz and Sohn (1990)[85], and subsequent experiments by Monkewitz et al. (1990)[84] confirmed the theoretical predictions. The flow is stable in figures 1.10 a) convectively unstable in figures 1.10 b) and absolutely unstable in figures 1.10 c). As expected, convectively unstable flows give rise to wave packets that move away from the source and ultimately leave the medium in its undisturbed state. Absolutely unstable flows, by contrast, are gradually contaminated everywhere by a point source input.

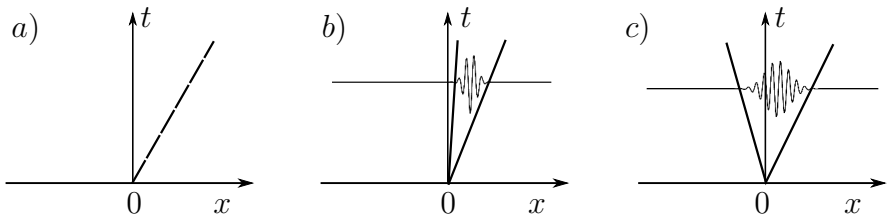


Figure 1.10: Case a) the flow is stable. Case b) the perturbation is convected away from $x = 0$ the flow is convectively unstable. Case c) the perturbation expands around $x = 0$ the flow is absolutely unstable.

It is now possible to treat linear stability problems in a framework where no assumption is made regarding the order of magnitude of the perturbation wavelength by discretizing all the non-homogeneous directions. Such approaches are referred to as global, in contrast with the local analyses described above. This distinction does not correspond to a difference in the methodology or mathematical concepts involved, but to the investigation of different situations. Using a two or three dimensional discretization, the temporal eigenmodes, optimal perturbations and optimal forcing (receptivity) can be analyzed by using exactly the same formalism as in the local approach. The modal analysis of the linearised flow equations gives access to the growth or decay rate, to the frequency and to the spatial structures of the eigenmodes. For a jet we can assume a "biglobal" behaviour of the disturbance by imposing that the base flow varies in two out of the three spatial directions and is independent of the azimuthal coordinate, $\bar{\boldsymbol{q}} = (x, r)$, the analysis proceeds by following:

$$\boldsymbol{q}'(x,r,\theta,t) = \bar{\boldsymbol{q}}(x,r) + \boldsymbol{q}(x,r)e^{i[m\theta - \omega t]}. \tag{1.16}$$

This amounts to considering the disturbance as harmonic dependence along the time and azimuth direction. The flow variables are expanded as two dimensional eigenfunctions in $(x,r)$ with a $\exp[i(\omega t - m\theta)]$ dependence, with integer $m$ and complex $\omega$. Unstable global modes have negative imaginary parts of $\omega$, and, inversely, for stable modes $\mathrm{Im}(\omega) > 0$. Such calculations are nowadays feasible, but much more numerically intensive than the application of methods based on parallel or slowly diverging base flows. A review of applications of global instability is made by Theofilis (2003)[125]. Since cold jets are convectively unstable, they present only globally stable modes, but combinations of such decaying modes, which are not orthogonal, may lead to amplitude growth during transients (see discussion by Schmid (2007)[110]). An example was recently shown by Nichols and Lele (2011)[91], who determined, for a supersonic jet, optimal combinations of global modes for transient growth of the fluctuation energy. Such transient growth causes emission of bursts of acoustic energy to the far field. The use of global linear theory is only justified when local modal analysis suggests that the flow will contain regions of local absolute instability. In that case, global linear theory can provide definitive answers which are free from the assumptions of local theory. However, when the instability in question is convective, convective instability analysis tools not only are adequate from a physical point of view but also orders of magnitude more efficient than global linear theory.

## 1.4 Sensitivity analysis

### 1.4.1 Introduction

Sensitivity analysis (SA) is the study of how the variation to different sources in the input of a mathematical model will modified, qualitatively or quantitatively, the output of the model. Or also, it is a technique for systematically changing parameters in a model to determine the effects of such changes. Such analysis is common in different fields of fluid dynamics since it is closely 'related' to optimisation problems and optimal control. 'Related' here means that these different fields of study (sensitivity, optimisation and control) can be outlined such that the sensitivity calculation becomes crucial.

The interest of sensitivity optimization and control in complex physical phenomena have grown in the years as economic, but also environmental needs. The field of aerodynamics is no exception. For example, large amounts of money could be saved if one could lower the fuel consumption of an airplane by just a fraction. To achieve this goal, control the flow around the aircraft might be one way.

In this thesis the idea is to use sensitivity analysis to identify the most sensitive region of the flow with respect to external forcing in order to propose some new noise control strategy.

During the last decade, new approaches to solve SA problems have emerged. By formulating the flow SA as the first step of optimization problems where one wants to

minimize or maximize some flow characteristic quantity, one obtains a problem similar to what is studied in optimal control theory. The early publications regarding optimal flow control problems, such as Abergel and Temam (1990)[1], Glowinski (1991) [38], Gunzburger et al. (1989)[44], Sritharan (1991a)[115], and Gunzburger et al. (1992) [45] are mostly concerned with theoretical aspects of the optimal control problem. Once the theoretical foundation was built, subsequent publications present results from numerical simulations where the optimal control for different flow configurations is computed. One such publication is Joslin et al. (1997)[58] where the optimal control of spatially growing two-dimensional disturbances in a boundary layer over a flat plate is computed.

When the number of parameters to analyse are small, direct search methods can be used, but when having many degrees of freedom, gradient based optimization algorithms are usually much more efficient. The gradient information can be computed in many different ways. In this thesis we compute it by solving the adjoint equations associated with the equations modeling the physics. The adjoint formulation is useful when one is seeking to obtain one or a few outputs of a system for a wide range of possible inputs. As said above, there are several such cases in fluid mechanics (and other disciplines), in particular in stability theory as concerning here, but the greatest advantage is obtained in optimization. In fact, the typical optimization problem has a single objective function (possibly combining multiple objectives through suitable weights) that has to be minimized or maximized with respect to a large number, or even a continuum, of input variables. From the solution of the adjoint equations, we obtain information about where the process is most sensitive to small modifications in the control or in the parameters. That information can also be used to compute the gradient in a procedure that is independent of the dimensionality of the optimization problem. The advantage of the adjoint approach, in fact, is that the sensitivity of a disturbance can be obtained by solving the state and adjoint equations once. This means that the adjoint method can provide the sensitivity to external forcing with an extremely low computational cost, if compared to direct search methods.

The first documented use of adjoint equations refers to Lord Lagrange (1763), but the use of adjoint equations in flow instability dates back to the 1990s, Hill (1992,1995)[52, 53], Chomaz (1993) [25] and Airiau (2000,2001) [3, 131], but did not become widespread until the late 2000s, Giannetti and Luchini (2007)[37], Marquet et al. (2008)[76]. We recommended the review articles Luchini and Bottaro (2014)[71] and Airiau (2004)[4] where the concepts of SA are spell out in details.

### 1.4.2 Sensitivity Analysis theoretical background

From a mathematically point of view sensitivity analysis leads to the determination of a gradient function. This gradient can be performed by finite difference or by complex-step derivatives but this is computationally expensive and prone to numerical error. A more efficient and more accurate method is to use adjoint equations.

It's a common notation call $E(\boldsymbol{q})$ cost functional and $\boldsymbol{q}$ state vector. Generally $\boldsymbol{q}$ must verified a constrained equation called state equation. In the following sections we assume that $n$ is the dimensions of $\boldsymbol{q}$ and $E(\boldsymbol{q})$ is a scalar number.

Sensitivity of a function $E$ with respect to a component of the vector $\boldsymbol{q}$, $q_i$, is simply defined as the directional gradient of $E$ with respect to $\boldsymbol{q_i}$, $\nabla E_{q_i}$.

The (scalar) directional derivative $d(\boldsymbol{q}, \boldsymbol{p})$ of a continuous quantity $E(\boldsymbol{q})$ is defined by:

$$d(\boldsymbol{q}, \boldsymbol{p}) = \frac{\partial E(\boldsymbol{q})}{\partial \boldsymbol{q}} \cdot \boldsymbol{p} = \lim_{\varepsilon \to 0^+} \frac{1}{\varepsilon} [E(\boldsymbol{q} + \varepsilon \boldsymbol{p}) - E(\boldsymbol{q})] \tag{1.17}$$

which is the amount $E(\boldsymbol{q})$ changes when $\boldsymbol{q}$ is updated in the direction $\boldsymbol{p}$, scaled by the size of the update, in the limit that the size of the update approaches zero. Note that the computation of $E(\boldsymbol{q})$ itself may involve large numerical simulations such as the marching of an ODE. The (vector) directional gradient $\boldsymbol{g}(\boldsymbol{q})$ of some continuous function $E(\boldsymbol{q})$ is given in each component $i$ by the directional derivative in the direction of the corresponding Cartesian unit vector $\boldsymbol{e}_i$ as:

$$g_i(\boldsymbol{q}) = d(\boldsymbol{q}, \boldsymbol{e}_i) = \frac{\partial E(\boldsymbol{q})}{\partial \boldsymbol{q}} \cdot \boldsymbol{e}_i \Longrightarrow \boldsymbol{g}(\boldsymbol{q}) = \nabla E(\boldsymbol{q}) \tag{1.18}$$

### a- Finite-difference approximation (FD)

One simple way to compute the directional derivate is to consider a Taylor series expansion from which the first order finite difference (FD) formula for the directional derivative is easily obtained:

$$d(\boldsymbol{q}, \boldsymbol{p}) = \frac{E(\boldsymbol{q} + \varepsilon \boldsymbol{p}) - E(\boldsymbol{q})}{\varepsilon} + \mathcal{O}(\varepsilon) \tag{1.19}$$

A second order version, using central differences, of the same approach can be written

$$d(\boldsymbol{q}, \boldsymbol{p}) = \frac{E(\boldsymbol{q} + \varepsilon \boldsymbol{p}) - E(\boldsymbol{q} - \varepsilon \boldsymbol{p})}{2\varepsilon} + \mathcal{O}(\varepsilon^2) \tag{1.20}$$

A drawback with the FD approach when using a computer with finite precision arithmetic is the difficulty to find a suitable value for the step size $\varepsilon$. If it is large then the Taylor series truncation is not valid and when it is small then the subtractive cancellation errors might dominate. For small $\varepsilon$ the error of FD formulas is $\mathcal{O}(1/\varepsilon)$ due to subtractive cancellation errors. This means that when comparing two numbers which are almost the same using finite precision arithmetic, the relative round off error is proportional to the inverse of the difference between the two numbers; thus, if the difference between the two numbers is decreased by an order of magnitude, the relative error with which this difference may be calculated using finite precision arithmetic is increased by an order of magnitude. Note that to evaluate $\frac{\partial E(\boldsymbol{q})}{\partial \boldsymbol{q}}$ as given by equations 1.19 and 1.20 requires $n+1$ and $2n$ computations, respectively. This can certainly be computationally expensive if each evaluation of $E$ requires the solution of an ODE.

### b- Complex step derivative (CSD)

The Complex Step Derivative (CSD) approximation makes use of complex variables in order to compute the directional derivative in a more robust fashion than the FD. If the

complex extension $E(\boldsymbol{z})$ of a real valued function $E(\boldsymbol{q})$ is analytic, it can be expanded with a complex Taylor series. The expansion of $E(\boldsymbol{q}+i\boldsymbol{p})$ can be written

$$E(\boldsymbol{q}+i\varepsilon\boldsymbol{p}) = E(\boldsymbol{q}) + i\varepsilon\frac{\partial E(\boldsymbol{q})}{\partial \boldsymbol{q}}\cdot\boldsymbol{p} + \mathcal{O}(\varepsilon^2) \tag{1.21}$$

and the directional derivative can be found by rearranging the expansion as

$$d(\boldsymbol{q},\boldsymbol{p}) = \frac{\partial E(\boldsymbol{q})}{\partial \boldsymbol{q}}\cdot\boldsymbol{p} = \frac{1}{\varepsilon}\mathrm{Im}[E(\boldsymbol{q}+i\varepsilon\boldsymbol{p})] + \mathcal{O}(\varepsilon^2) \tag{1.22}$$

Note that the error scales with $\varepsilon^2$ and there are no cancellation errors in this approximation. that is, to leading order, the unperturbed part is represented in the real components, and the perturbed part is represented in the imaginary components of the variables. In this approach $\varepsilon$ can be chosen several orders of magnitude smaller than the other numerical values appearing in the problem since we do not have cancellation error all the way to numerical round off error of the finite precision arithmetic. This approach requires $n$ computations, which is similar to the first order finite difference method shown previously. Remember, however, that it is more robust with respect to the choice of the value of $\varepsilon$.

### c- Adjoint based approach

The approach introduced in this section is based on the so called adjoint equations and is shown to be very efficient in cases where the value of $m \ll n$. Before demonstrating this we start by showing a couple of examples. In the first the function $E$ depends linearly on the solution $\boldsymbol{x}$ of a linear system:

$$E(\boldsymbol{x}) = \boldsymbol{c}^t\boldsymbol{x} \tag{1.23}$$

$$A\boldsymbol{x} = \boldsymbol{b} \tag{1.24}$$

where $A$ is a know matrix $A \in \mathbb{R}^{n,n}$ , $\boldsymbol{c}$ and $\boldsymbol{b}$ are the know vectors $\boldsymbol{c} \in \mathbb{R}$, $\boldsymbol{b} \in \mathbb{R}$, respectively. Let us now find the derivative of $E$ with respect to the vector $\boldsymbol{b}$, $\frac{\partial E}{\partial \boldsymbol{b}}$. This can be obtained very efficiently by solving an additional linear system

$$A^t\boldsymbol{y} = \boldsymbol{c} \tag{1.25}$$

The relation between the new linear system 1.25 and the function $E$ is found by some simple linear algebra:

$$E = \boldsymbol{c}^t\boldsymbol{x} = (A^t\boldsymbol{y})^t\boldsymbol{x} = \boldsymbol{y}^tA\boldsymbol{x} = \boldsymbol{y}^t\boldsymbol{b} \tag{1.26}$$

it can be noted that with the new linear system 1.25, $E$ depends explicitly on the vector $\boldsymbol{b}$. After this substitution it is straight forward to compute the derivative as

$$\frac{\partial E(\boldsymbol{b})}{\partial \boldsymbol{b}} = \boldsymbol{y}^t \tag{1.27}$$

In this case the computational cost is 1 since only one solution of equation (9) is needed to evaluate 1.27. In many optimization and control problems it is common to have a cost

function with depends on the square of the linear system. An example of this is given below.

$$E(\boldsymbol{x}) = \frac{1}{2}\boldsymbol{x}^t\boldsymbol{x} \tag{1.28}$$

$$A\boldsymbol{x} = \boldsymbol{b} \tag{1.29}$$

In this case we start by linearising the system, which actually involves only the function $E$. For this purpose we decompose $\boldsymbol{x}$ and $\boldsymbol{b}$ into mean and a perturbation as $\boldsymbol{x} = \bar{\boldsymbol{x}} + \varepsilon\boldsymbol{x}'$ and $\boldsymbol{b} = \bar{\boldsymbol{b}} + \varepsilon\boldsymbol{b}'$. Introducing the decomposition into equations 2.1-2.2 and dropping higher order $\varepsilon$-terms we obtain a system of equations for $\boldsymbol{x}'$ and $\boldsymbol{b}'$. This is written

$$\delta E = \bar{\boldsymbol{x}}^t\boldsymbol{x}' \tag{1.30}$$

$$A\boldsymbol{x}' = \boldsymbol{b}'. \tag{1.31}$$

The additional linear system is now given as

$$A^t\boldsymbol{y} = \bar{\boldsymbol{x}} \tag{1.32}$$

and the function $\delta E$ can be evaluated as

$$\delta E = \bar{\boldsymbol{x}}^t\boldsymbol{x}' = (A^t\boldsymbol{y})^t\boldsymbol{x}' = \boldsymbol{y}^tA\boldsymbol{x}' = \boldsymbol{y}^t\boldsymbol{b}' \tag{1.33}$$

The gradient is then evaluated easily as

$$\frac{\partial E(\boldsymbol{b})}{\partial \boldsymbol{b}} = \boldsymbol{y}^t \tag{1.34}$$

Note that in this case the right hand side of the new linear system 1.32 is a function of the solution of the original linear equation 1.31. This means that the computational cost in this case is 2; first we need to solve 1.31, and successively equation 1.32. Further, this must be done for each dimension of $E$, as in the case of the FD and CSD, that is 1 in this example.

### d- Comparison of computational effort

We can now compare the computational effort of computing the gradient $\nabla E(\boldsymbol{q})$ using the three methods that were outline above. In table 4.1 the number of function evaluations is given as a function of a given method. Here, $n$ and $m$ denote the dimensions of $\boldsymbol{q}$ and $E(\boldsymbol{q})$, respectively. Values for both first order (FD1) and second order (FD2) finite difference method are shown. It is evident that using adjoint equations is computationally efficient. The computational efficiency of the CSD is comparable to the FD1. However, the CSD is more robust since it does not involve any difference operations which means that numerical cancellation errors are avoided. In many applications the number of function values $m$ is much smaller than the parameter or variable that one perturb which has dimension $n$. For example, considering the case of the variation of the total energy of a flow ($m = 1$) is estimated as a function of an external source acting in a localized region of the flow. In this case $n$ are the number of discrete points where the forcing could be placed, typically of the order of $10^2 - 10^3$.

| Approach | $E(\boldsymbol{x}) = \boldsymbol{c} \cdot \boldsymbol{x}$ | $E(\boldsymbol{x}) = \boldsymbol{x} \cdot \boldsymbol{x}$ |
|---|---|---|
| FD1 | $(n+1)$ | $(n+1)$ |
| FD2 | $2 \cdot n$ | $2 \cdot n$ |
| CSD | $n$ | $n$ |
| ADJ | 1 | 2 |

Table 1.1: Number of function evaluations to compute the gradient using Finite Difference approximation (FD), Complex step derivative (CSD) and adjoint equations (ADJ). First and second order FD approach are denoted FD1 and FD2.

### 1.4.3 Some Results

The idea of an adjoint equation assembles together a number of mathematical concepts, physical theories, and computational methods. Historically, it has evolved from a device to lower the order of an ordinary differential equation, more recently, adjoint equations have been identify as a powerful tool in the study of the sensitivity of some global quantity (an objective) with respect to some input data of a complicated problem (e.g., the numerical discretization of an ordinary or partial differential equation). Sensitivity can be simultaneously computed by an adjoint algorithm having approximately the same computation time as a single run of the original simulation. This is much faster than a classical linearisation approach in which one would have to numerically solve a separate linearised problem for the increment in each input variable.

Adjoint based sensitivity analysis is exploited in many different engineering fields not only in fluid dynamics, including nuclear reactor physics, electromagnetism, seismic tomography, dynamic meteorology, illumination computations in computer graphics, inverse design problems, heat conduction, etc.

In this work the main goal is to identify the regions of the flow more sensitive to external perturbations in the momentum forcing and mass or heat injection.

Sensitivity coefficients can be therefore explained as how the response of any variation in the output of a system expressed as a mathematical functional can be apportioned to different sources of variation in the input of the model. Such analysis is common in different fields of engineering and in the field of fluid dynamics since it is closely related to optimization problems and optimal control (Walther et al.[131] and Airiau [3]). In the last 45 years receptivity of boundary layers flows was investigated in different theoretical and computational manners. Recently, [7] has demonstrated that receptivity coefficients and the approach based on adjoint equations [3] can be associated to an optimization problem and therefore they were strongly closed to sensitivity coefficients. Later it was used by [131, 5] to perform optimal control in the laminar boundary layer flow. Sensitivity analysis based on the adjoint of compressible Navier-Stokes were also recently derived [101, 114, 132] and have led to some optimal control studies of the two dimensional shear layer in the aeroacoustic framework. Some other examples of sensitivity can be found in the mesh optimization and in the optimization of structures.

A first sensitivity analysis of jet instabilities associated to compressible jet at low

Mach number has been performed and validated recently by coupling the Parabolized Stability Equations (PSE) and the Adjoint-PSE method[11, 131]. In 2014 Kim et al. [59] used the adjoint solutions of the Euler equations to provide a definitive direction in which adjust a model control actuation in order to reduce turbulent jet noise. In parallel, Tissot et al[127] has proposed, using some PSE-4D-Var approach to investigate the role of the critical layer in jet in presence of non linear wave interactions. Following this previous works, an extension of the compressible laminar flow to turbulent and supersonic flow is made.

In this thesis sensitivity for a subsonic and supersonic flow [134] are implemented as test case for the validation of the model. Finally single and double jet flow has been computed from Large-Eddy-Simulation [12]. In particular the most sensitive zones to some local forcing in the conservation stability equations are identified.

From our knowledge, the sensitivity analysis in the framework of adjoint of PSE stability equations for supersonic jets in relation with aeroacoustic has never been done yet. Investigate flow sensitivities to any external source hopefully will lead to define some new noise control strategies.

# Chapter 2

# Non local jet stability

In this chapter the Parabolized Stability Equations based to the linearised Euler Equations are treated. The PSE were initially proposed by Herbert and Bertolotti (1987)[51] and some other authors during the same period [6] to study the linear and non linear development of Tollmien-Schlichting waves in boundary layers. Later 2000, works from [23, 22, 103] have extended PSE to jet flow. The main advantages of the choice of PSE instead of Local Stability Theory (LST) are at least three:

- the small streamwise variations of the base flow and of the disturbances are directly taken into account in the formulation (contrarily to LST where local parallel flow is assumed).

- the eigenvalue problem no longer exists and the PSE is set of Partial Differential Equations (PDE) mostly parabolic in the streamwise direction

- since PSE are PDE, it is simpler to solve it by adding various boundary conditions and source terms. That means that they are used for receptivity and sensitivity analysis, in optimal flow control approaches and for weakly non linear stability analysis

The equations 2.17-2.19 are developing in cylindrical coordinates, as shown in figure 2.1: $x$ is the streamwise coordinates, ,$r$ is the redial coordinates and $\theta$ the azimuthal direction.

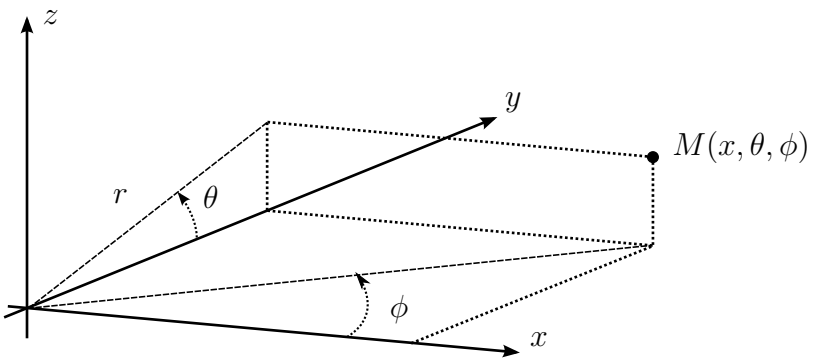


Figure 2.1: The coordinate system used in this thesis

The PSE theory is explained in details as far as the numerical method implemented to solve the PSE system. Finally, validations for subsonic and supersonic cases is reported and results for LES computations is discussed for single and for dual stream jet.

## 2.1 Non local stability theory: PSE approach

### 2.1.1 The conservation equations

Assuming that the evolution of the perturbation in the baseflow are inviscid we start this theory considering the Euler equations written for compressible flow. Cylindrical coordinates system is used, $(r, \theta, x)$, denotes radial, azimuthal and streamwise directions respectively. $t$ is the time. The physics quantities that characterize the state of the flow are the density $\varrho$, the velocity vector $\boldsymbol{U}$, the pressure $P$ and the entropy $S$. The three equations written below are the conservation of the mass flow, of the momentum and the of the energy, respectively.

$$\frac{\partial \varrho}{\partial t} + \boldsymbol{\nabla}\varrho \cdot \boldsymbol{U} + \varrho \boldsymbol{\nabla} \cdot \boldsymbol{U} = 0, \tag{2.1}$$

$$\frac{\partial \boldsymbol{U}}{\partial t} + \boldsymbol{\nabla}\boldsymbol{U} \cdot \boldsymbol{U} = -\frac{1}{\varrho}\boldsymbol{\nabla}P, \tag{2.2}$$

$$\frac{\partial S}{\partial t} + \boldsymbol{\nabla}S \cdot \boldsymbol{U} = 0. \tag{2.3}$$

Using the perfect gas assumption the entropy $S$ is given by

$$S = C_v \ln\left(\frac{P}{\varrho^\gamma}\right), \tag{2.4}$$

where the specific heat capacity at constant volume $C_v$ and the specific heat ratio $\gamma$ being constant.

### 2.1.2 Non dimensional equations

Before considering any kind of theoretical approach is important to normalize the variables of the system by a dimensional analysis. This techniques allows us to determine important non dimensional parameters of the flow and to compare different flows with respect to those parameters. The subscript "j" refers to the conditions at the exit of the nozzle measured in the axis position. The lengths are non dimensionalized by the diameter $D_j$, the velocity by the streamwise exit velocity $U_j$, the density by $\rho_j$, the pressure by $\rho_j U_j^2$, the time by $D_j/U_j$ and other variables by the corresponding jet exit conditions. The Mach, Reynolds and Prandtl numbers are defined as follow:

$$M_j = \frac{U_j}{a_j} \tag{2.5}$$

$$Re_d = \frac{U_j \rho_j D_j}{\mu_j} \tag{2.6}$$

$$Pr = \frac{\mu_j C_p}{\lambda_j} \tag{2.7}$$

where $a_j$ is the sound velocity, $\mu_j$ the dynamic viscosity and $\lambda_j$ is the thermal conductivity coefficient of the flow. Generally, the sound velocity is defines as:

$$a = \sqrt{\gamma \frac{P}{\varrho}} = \sqrt{\gamma \frac{R}{M} T}, \tag{2.8}$$

where $R$ (approximately $8.314,5\ J/(mol \cdot K)$) is the molar gas constant and $M$ is the molar mass of the gas (the mean molar mass for dry air is about $0.028,964,5\ kg/mol$). Under these conditions the non dimensional term of the pressure $P$ can be written as:

$$\frac{P_j}{\rho_j U_j^2} = \frac{1}{\gamma M_j^2} \tag{2.9}$$

To be clear, the dimensionless Euler equations are written with the same notation as in equation 2.1-2.3.

### 2.1.3 Linearisation

A common approach in the analysis of nonlinear systems is linearisation around a given state, in which the full solution is split into a steady term and a small time variant perturbation. The total flow vector $\boldsymbol{Q} = (\boldsymbol{U}, \varrho, P)^t$ is decomposed as follow:

$$\boldsymbol{Q} = \bar{\boldsymbol{q}} + \varepsilon \boldsymbol{q}'(\boldsymbol{x}, t) \tag{2.10}$$

where $\bar{\boldsymbol{q}}$ and $\boldsymbol{q}$ respectively denote the time invariant and the (low energy) fluctuating states. The constant $\varepsilon$ is supposed to be small enough to neglet the non linear terms. Under the normalization introduced in section 2.1.2 the decomposition in equation 2.10 becomes

$$U_x = \bar{u}_x + u'_x, \tag{2.11}$$

$$U_r = \bar{u}_r + u'_r, \tag{2.12}$$

$$U_\theta = u'_\theta \qquad \text{(no mean swirl; } \bar{u}_\theta = 0), \tag{2.13}$$

$$S = \bar{s} + s', \tag{2.14}$$

$$\varrho = \bar{\rho} + \rho', \tag{2.15}$$

$$P = \frac{1}{\gamma M_j^2} + p' \tag{2.16}$$

We proceed by substituting this decomposition into equations 2.1 to 2.3 and subtracting the mean:

$$\frac{\partial \rho'}{\partial t} + \bar{\rho}(\boldsymbol{\nabla} \cdot \boldsymbol{u}') + \rho'(\boldsymbol{\nabla} \cdot \bar{\boldsymbol{u}}) + (\bar{\boldsymbol{u}} \cdot \boldsymbol{\nabla}\rho') + (\boldsymbol{u}' \cdot \boldsymbol{\nabla}\bar{\rho}) = 0 \tag{2.17}$$

$$\bar{\rho}\left(\frac{\partial \boldsymbol{u}'}{\partial t} + (\underline{\boldsymbol{\nabla}\boldsymbol{u}'} \cdot \bar{\boldsymbol{u}}) + (\underline{\boldsymbol{\nabla}\bar{\boldsymbol{u}}} \cdot \boldsymbol{u}')\right) + \boldsymbol{\nabla}p' = \boldsymbol{0} \tag{2.18}$$

$$\frac{\partial s'}{\partial t} + (\boldsymbol{\nabla}s' \cdot \bar{\boldsymbol{u}}) + (\boldsymbol{\nabla}\bar{s} \cdot \boldsymbol{u}') = 0 \tag{2.19}$$

Here we have neglected all nonlinear fluctuating terms (e.g., $u_r u/r$). In this work we restrict our attention to linear disturbances and so do not discuss non linear instabilities components further.

Defining $\boldsymbol{a} = (a_x, a_r, a_\theta)^t$ and $\boldsymbol{b} = (b_x, b_r, b_\theta)^t$ as two general vectors and $c$ a constant, the mathematics operators used above have the following form:

$$\boldsymbol{\nabla} \cdot \boldsymbol{a} = \frac{\partial a_x}{\partial x} + \frac{1}{r}\frac{\partial (r a_r)}{\partial r} + \frac{1}{r}\frac{\partial a_\theta}{\partial \theta} \tag{2.20}$$

$$\boldsymbol{\nabla} c = \left(\frac{\partial c}{\partial x}, \frac{\partial c}{\partial r}, \frac{1}{r}\frac{\partial c}{\partial \theta}\right)^t \tag{2.21}$$

$$\underline{\boldsymbol{\nabla}\boldsymbol{a}} \cdot \boldsymbol{b} = \begin{pmatrix} b_x \dfrac{\partial a_x}{\partial x} + b_r \dfrac{\partial a_x}{\partial r} + \dfrac{b_\theta}{r}\dfrac{\partial a_x}{\partial \theta} \\ b_x \dfrac{\partial a_r}{\partial x} + b_r \dfrac{\partial a_r}{\partial r} + \dfrac{b_\theta}{r}\dfrac{\partial a_r}{\partial \theta} - \dfrac{b_\theta a_\theta}{r} \\ b_x \dfrac{\partial a_\theta}{\partial x} + b_r \dfrac{\partial a_\theta}{\partial r} + \dfrac{b_\theta}{r}\dfrac{\partial a_\theta}{\partial \theta} + \dfrac{b_\theta a_r}{r} \end{pmatrix} \tag{2.22}$$

Substituting these news definitions into equations 2.17-2.19 and considering the perfect gas assumption 2.4 we obtain

$$\frac{D\rho'}{Dt} + \bar{\rho}\left(\frac{\partial u'_x}{\partial x} + \frac{1}{r}\frac{\partial (r u'_r)}{\partial r} + \frac{1}{r}\frac{\partial u'_\theta}{\partial \theta}\right) +$$
$$\rho'\left(\frac{\partial \bar{u}_x}{\partial x} + \frac{1}{r}\frac{\partial (r\bar{u}_r)}{\partial r}\right) + \left(u'_x\frac{\partial \bar{p}}{\partial x} + u'_r\frac{\partial \bar{\rho}}{\partial r}\right) = 0$$
$$\bar{\rho}\left(\frac{Du_r}{Dt} + u'_x\frac{\partial \bar{u}_r}{\partial x} + u'_r\frac{\partial \bar{u}_r}{\partial r}\right) + \frac{\partial p'}{\partial r} = 0$$
$$\bar{\rho}\left(\frac{Du_\theta}{Dt} + \frac{u'_\theta \bar{u}_r}{r}\right) + \frac{1}{r}\frac{\partial p'}{\partial \theta} = 0$$
$$\bar{\rho}\left(\frac{Du_x}{Dt} + u'_x\frac{\partial \bar{u}_x}{\partial x} + u'_r\frac{\partial \bar{u}_x}{\partial r}\right) + \frac{\partial p'}{\partial x} = 0$$
$$\bar{\rho}M_j^2\frac{Dp'}{Dt} - \frac{D\rho'}{Dt} - u'_x\frac{\partial \bar{\rho}}{\partial x} - u'_r\frac{\partial \bar{\rho}}{\partial r} = 0$$

where the derivative $D/Dt$ is defined with respect to the base flow as

$$\frac{D}{Dt} = \frac{\partial}{\partial t} + \bar{u}_x\frac{\partial}{\partial x} + \bar{u}_r\frac{\partial}{\partial r} \tag{2.23}$$

This system of 5 equations and 5 unknowns, $(u'_x, u'_r, u'_\theta, \rho', p')$ is the final system which is finally based the linear PSE analysis.

### 2.1.4 Considerations about the baseflow

The results of stability analysis are sensitive to the choice of mean flow. Typically aircraft jets are highly turbulent and the effects of this on the mean flow must be accounted for. To this end, one could compute the mean flow from experimental measurements of such flows or by time and azimuthal average of computation results (as DNS, LES, RANS etc..). This is particularly attractive as nonlinear effects are then partially included via their effect on the time invariant state. However, Bagheri et al (2009)[13] computed the base flow with respect to the nonlinear Navier-Stokes equations using the selective frequency damping method. With this method an equilibrium state of the jet flow, that it is different to the average to the azimuthal and temporal average of the flow, is identified. This method can not be apply at our analysis because of the high values of the Reynolds numbers in the different cases investigated. Inspired to the work of the many others researcher, just to cite one of them[98, 64, 43], The time average from LES or from RANS computation have been adopted in this work.

Questions regarding the evolution of small perturbations into the equilibrium state may then be addressed via the solution $\boldsymbol{q}'$ of the linearised Euler Equations (LEE). If the linear solution is unstable then the nonlinear solution is also unstable. Linear stability does not necessarily imply nonlinear stability, however, as nonlinear bifurcations to other states may occur.

### 2.1.5 Linear non local theory

PSE approach is based to new hypothesis of the nature of the perturbations that leads to a simplifier system of equations. However, using this approach instead of the classical Linear Stability Theory allow us to take into account the growth of the shear layer. Here we restrict ourselves to the quasi three dimensional flows (base flows which are axisymmetric, independent of the $\theta$ coordinate). Derivation of the non local stability equations can be done by introducing the two following assumption:

1. The first assumption is to divide the perturbation $\boldsymbol{q}'$ into an amplitude and an oscillating part:

$$\boldsymbol{q}' = \boldsymbol{q}(x, r)e^{i\Theta}. \tag{2.24}$$

   with

$$\Theta = \int_{x_0}^{x} \alpha(\xi)d\xi + m\theta - \omega t, \tag{2.25}$$

   where $\boldsymbol{q}$ is the vector with components $\boldsymbol{q} = (u_x, u_r, u_\theta, \rho, p)^t$ and $x_0$ is the minimum streamwise coordinate in the computational domain. Here, as in a spatial theory, $\alpha$ is a complex number. Note that in the non local theory both the amplitude, $\boldsymbol{q}$ and the phase function, $\Theta$, are allowed to varying in the streamwise direction.

2. As a second assumption, a scale separation $\varepsilon = \mathcal{O}(Re^{-1})$ is introduced between the weak variation in the $x$-direction and the strong variation in the $r$-direction, following the approach developing by Herbert (1997)[50]. Here $Re$ is the local Reynold number computed at the initial of the computational domain, $Re = \sqrt{\frac{U_j x_0}{\nu}}$.

For the disturbances $\boldsymbol{q}'(x, r, \theta, t)$ we would like to impose the shape function slowly varying in the $x$-direction, so that all the waviness and growth of the disturbance are absorbed into the exponential term containing the streamwise wavenumber, $\alpha$. This new perturbation is written as

$$\boldsymbol{q}'(r, \theta, t) = \boldsymbol{q}(r, \theta, t)\mathrm{e}^{i\left(\int_{x_0}^{x} \alpha(\xi)d\xi + m\theta - \omega t\right)}$$

where the spatial and temporal partial derivatives are written as

$$\frac{\partial \boldsymbol{q}'}{\partial x} = \left(\frac{\partial \boldsymbol{q}}{\partial x} + i\alpha(x)\boldsymbol{q}\right)e^{i\Theta}$$

$$\frac{\partial \boldsymbol{q}'}{\partial r} = \frac{\partial \boldsymbol{q}}{\partial r}e^{i\Theta}$$

$$\frac{\partial \boldsymbol{q}'}{\partial \theta}) = im\boldsymbol{q}e^{i\Theta}$$

$$\frac{\partial \boldsymbol{q}'}{\partial t} = -i\omega \boldsymbol{q} e^{i\Theta}$$

Substituting equation 2.24 into equation 2.17-2.19 we obtain the PSE equations.

$$L_{PSE}\boldsymbol{q} = \boldsymbol{0}, \qquad \text{with} \qquad L_{PSE} = i\alpha A_1 + imA_2 - i\omega A_3 + B + A_1\frac{\partial}{\partial x} + A_0\frac{\partial}{\partial r} \tag{2.26}$$

$A_0, A_1, A_2, A_3$ and $B$ are matrices function of the base flow quantities and are detailed in the appendix. Following [98, 63] some specific boundary conditions are set on the axis. To avoid the singularity in the axial position, at $r = 0$, the boundary conditions used to the shape function, $\boldsymbol{q}$, are:

$$\begin{aligned} u_r(0,x) &= 0 && \text{for } m = 0 \\ u_r(0,x) + imu_\theta(0,x) = 0, \quad p(0,x) &= 0 && \text{for } m \geq 1 \end{aligned}$$

They are completed by the non singular terms in the PSE equations, expressed at $r = 0$. In the far field $r \to \infty$ assumption of flow at rest are made by considering $\bar{u}_x = \bar{u}_r = \bar{u}_\theta = 0$. Because we are in the far field all the derivatives in the streamwise direction are neglected and equation 2.26 reduces to:

$$\begin{aligned} i\bar{\rho}\alpha u_x + \frac{\bar{\rho}}{r}u_r + \frac{im\bar{\rho}}{r}u_\theta - i\omega\rho + \bar{\rho}\frac{\partial u_r}{\partial r} &= 0 \\ -i\omega\bar{\rho}u_r + \frac{\partial p}{\partial r} &= 0 \\ -i\omega\bar{\rho}u_\theta + \frac{im}{r}p &= 0 \\ -i\omega\bar{\rho}u_x + i\alpha p &= 0 \\ i\omega\rho - i\omega\bar{\rho}M_j^2 p &= 0 \end{aligned} \tag{2.27}$$

and after some mathematical steps

$$\frac{\partial^2 p}{\partial r^2} + \frac{1}{r}\frac{\partial p}{\partial r} + \left(\bar{\rho}\omega^2 M_j^2 - \frac{m^2}{r^2} - \alpha^2\right)p = 0 \tag{2.28}$$

The solution of equation 2.28 are a linear combination of the Hankel functions of the first kind and second kind

$$p = H_m^1\left(\sqrt{\alpha^2 - \bar{\rho}\omega^2 M_j^2}\, r\right) \tag{2.29}$$

where $H_m^1$ is the $m$-th order Hankel function of the first kind. Finally by taking into account the asymptotic behaviour of the Hankel function when $r \to \infty$, we obtain:

$$\frac{\partial p}{\partial r} + \left(\sqrt{\alpha^2 - \bar{\rho}\omega^2 M_j^2} + \frac{1}{2r}\right)p = 0 \tag{2.30}$$

### 2.1.6 Normalization equation

By observing the decomposition of equation 2.24 it can be noticed that the streamwise change of the disturbance $\hat{\boldsymbol{q}}(x,r)$ can be described by the product of the shape function $\boldsymbol{q}(x,r)$ and of the exponential term $\chi(x)$, where $\chi(x) = \exp\left(\int_{x_0}^{x} \alpha(\xi) d\xi\right)$. This ambiguity must be resolved by the introduction of an additional equation, called normalization or closure relation which imposes that the exponential growth of the disturbance is absorbed by the wave function part of the decomposition $\chi(x)$, making sure that the shape function $\boldsymbol{q}(x,r)$ stays slowly varying in $x$. The definition of the normalization is based on the definition of the complex wave number respectively in the local and non local approach and with any component of the perturbation $q'_k$:

$$-i\frac{\partial \ln(q'_k)}{\partial x} = \alpha_{local} \qquad \text{and} \qquad -i\frac{\partial \ln(q'_k)}{\partial x} = \alpha_{PSE} - i\frac{1}{q_k}\frac{\partial q_k}{\partial x} \tag{2.31}$$

Naturally in the local stability theory the wave number is independent of radial direction $r$ contrarily to the PSE theory case if the previous definition is kept. To remove this apparent dependency in $r$ we introduce a weighting in the definition of the complex wave number as following:

$$-i\int_0^\infty |q_k|^2 \frac{\partial \ln(q'_k)}{\partial x}\, m_r\, dr = \alpha(x)\left[\int_0^\infty |q_k|^2\, m_r\, dr\right] - i\int_0^\infty q_k^h \frac{\partial q_k}{\partial x}\, m_r\, dr. \tag{2.32}$$

Where $m_r$, generally, is a metric equal to 1 or $r$. Imposing the following condition is just a way to retrieve for $\alpha(x)$ the same definition as in the local stability theory:

$$\int_0^\infty \bar{q}_k \frac{\partial q_k}{\partial x}\, m_r\, dr = 0 \qquad \text{and more generally} \qquad \mathcal{N}(\boldsymbol{q}) = \int_0^\infty (N\boldsymbol{q})^h \frac{\partial N\boldsymbol{q}}{\partial x}\, m_r\, dr = 0 \tag{2.33}$$

The matrix $N$ can let choose which components of the state vector are used in the closure relation. The choice of another specific normalization would not change the value of the physical disturbance, as soon as this normalization removes the waviness and growth of the disturbance from the shape function to include it in the exponential term as [6, 50, 98] have shown. Concerning the PSE solver used in this thesis a deep analysis of the different normalizations is investigated in [63]. This analysis show how the perturbation value $\boldsymbol{q}'$ is non dependent of the normalization if the problem is well pose. All results presented in the following refer to the normalization of the whole components of $\boldsymbol{q}$ by imposing $N = I$ and $m_r = r$

### 2.1.7 Numerical method for the resolution of the linear PSE system

A compressible PSE solver designed by Léon and Brazier[63] has been used to get perturbation growth rate, wave number and shape function of the perturbation field. The

system of equations 2.26 and 2.33 are solved using a streamwise marching solution starting from the nozzle exit at $x = x_0$ . The system is initialized by the solution of the local approach (LST). The radial direction is discretized using a multidomain spectral collocation approach, or using a sixth order compact difference scheme with sectral-like resolution, see Lele (1992)[62]. The mesh in the radial direction is discretized on a non uniform grid. The first and second derivative of the metric are continuous in order to provide a good accuracy when the radial derivatives of the parameters are computed:

$$\frac{\partial \boldsymbol{q}}{\partial r} = \mathcal{E}\boldsymbol{q} \tag{2.34}$$

where the matrix $\mathcal{E}$ is different if using spectral collocation method or finite-difference compact schemes.

The discretized problem is solved iteratively in the streamwise direction for the shape function $\boldsymbol{q}$ at each axial location. The wavenumber $\alpha$ is updated at each iteration using the classical scheme:

1. Advance $x$-position one step
2. Update the solution for $\boldsymbol{q}(x)$ equation 2.26 by solving a linear system.
3. Update $\alpha(x)$, $\alpha_j^{(p+1)} = \alpha_j^{(p)} + \Delta\alpha\mathrm{j}^{(p+1)}$, where $j$ refer to the position $x_j$ in the discretized streamwise direction and $p$ is the number of iteration
4. Check for convergence on $\alpha(x)$, $\left|\frac{\Delta\alpha_j^{(p)}}{\alpha_j^{(p)}}\right| < \varepsilon$. If not verified go to 2). Otherwise go to 1)

An efficient method to compute $\Delta\alpha_j^{(p)}$ can be obtained following the previous work of Herbert (1993)[49] and Airiau (1994)[2]. The update value of $\alpha_j^{(p+1)}$ at the position $x_j$ is given by

$$\alpha_j^{(p+1)} = \alpha_j^{(p)} - i\frac{N(\boldsymbol{q}_j^{(p)}, \boldsymbol{q}_{j-1}^{(p)})}{A^2(\boldsymbol{q}_j^{(p)})}, \tag{2.35}$$

with

$$N(\boldsymbol{q}_j^{(p)}, \boldsymbol{q}_{j-1}^{(p)}) = \int_0^\infty (\boldsymbol{q}_j^{(p)})^h \cdot \frac{\boldsymbol{q}_j^{(p)} - \boldsymbol{q}_{j-1}^{(p)}}{\Delta x_j} r\, dr \tag{2.36}$$

$$A^2(\boldsymbol{q}_j^{(p)}) = \int_0^\infty (\boldsymbol{q}_j^{(p)})^h \cdot (\boldsymbol{q}_j^{(p)}) r\, dr \tag{2.37}$$

In this thesis $\varepsilon$ is fixed as, $\varepsilon = 10^{-8}$ and needs around $6-8$ iterations when computing close to the exit nozzle and decay until $2-3$ after some diameters far to the nozzle.

The PSE system written in the discretized form leads to:

$$\left(\alpha(x)A_1 + mA_2 + \omega A_3 + B\right)\boldsymbol{q}_j + A_1\left[\frac{(\boldsymbol{q}_j - \boldsymbol{q}_{j-1})}{\Delta x_j}\right] + A_0\left[\mathcal{E}\boldsymbol{q}\right] \tag{2.38}$$

finally, the shape function $\boldsymbol{q}_j$ is computed by solving the following system:

$$\left(\alpha(x)A_1 + mA_2 + \omega A_3 + B + \frac{A_1}{\Delta x_j} + A_0\mathcal{E}\right)\boldsymbol{q}_j = \frac{A_1}{\Delta x_j}\boldsymbol{q}_{j-1} \tag{2.39}$$

Notice that the streamwise derivative, $\frac{\partial \boldsymbol{q}}{\partial x}$, is approximated by the backward finite difference form $(q_j - q_{j1})/\Delta x_j$. Figure 2.2, extracted by Léon (2012)[63] and Airiau (1994)[2], schematically represent the computational approach used to solve the PSE system:

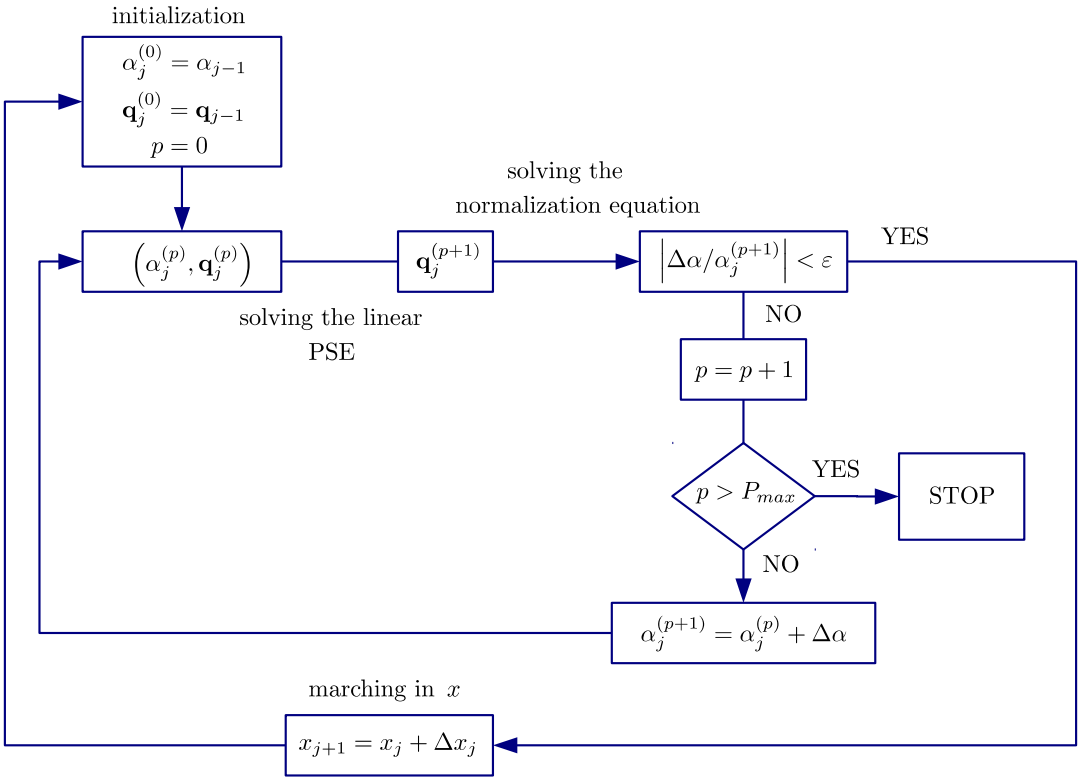


Figure 2.2: Simple scheme of the PSE solver.

### 2.1.8 Stability of the PSE system

Are Parabolic Stability Equations parabolic? The answer is no. There exists a residual ellipticity mainly of acoustic nature which means this system is only partially parabolic, Chang et al. (1991)[21]. Numerically instability would occur in attempting to use a too small marching stepsize in $x$, similar to that observed in applications of the Parabolized Navier-Stokes equation formulation, PNS, Rubin and Tannehill (1992)[108]. Li and Mailik (1996)[65] used Fourier analysis to prove the existence of numerical instability and quantify

the bounds. It is demonstrated that the minimum step size, $\Delta x_{min}$ for numerical stability is, approximately, the inverse of the real part of the streamwise wavenumber:

$$\Delta x_{min} = \frac{1}{\alpha_r} = \frac{\lambda}{2\pi}. \tag{2.40}$$

This implies that a maximum of $2\pi$ steps per disturbance wavelength $\lambda$ are allowed for the marching. To reduce this step size we have at least two ways:

- drop out the $\frac{\partial p}{\partial x}$ term. Li and Mailik (1996)[65] point out that since most of the pressure gradient has been absorbed into the $i\alpha\bar{p}$ term the $\frac{\partial p}{\partial x}$ term is small in comparison. They also demonstrate that the step-size restriction is reduced by at least an order of magnitude.

- Introduce a stabilization term, Andersson et al. (1998)[8], that removes the ellipticity and leads to a well posed parabolic set of stability equations

Both approaches are good with minimal impact on the result. The weak ellipticity of the PSE was in addition analysed trough the Fourier and the characteristic theory by Airiau 1991[2]. If small steps of $\Delta x$ are required, as in presence of shock-cell in the base flow, simply neglect the term $\frac{\partial p}{\partial x}$ may not be enough. Following Andersson et al. [8] we added a stabilizing term which is of the same order as the numerical errors. Since terms of this order were neglected in the original approximation of PSE, the addition of this artificial term does not introduce any extra error at this order of approximation and we can introduce the new set of equations:

$$\begin{aligned} A_1\frac{\partial \boldsymbol{q}}{\partial x} + (i\alpha A_1 + imA_2 - i\omega A_3 + B + A_0\frac{\partial}{\partial r})\boldsymbol{q} = \\ -s(i\alpha A_1 + imA_2 - i\omega A_3 + B + A_0\frac{\partial}{\partial r})\frac{\partial \boldsymbol{q}}{\partial x} \end{aligned} \tag{2.41}$$

With this new configuration the critical step size is now defined as:

$$\Delta x_{min} > \frac{1}{|\alpha_r|} - 2s \tag{2.42}$$

Equation 2.42 implies that the $s$ value giving marginal stability approaches $0.5/\,|\alpha_r|$ when $\Delta x_{min} \to 0$. Consequently, we can stably march PSEs downstream for any arbitrarily small step size by using a suitable $s$. In our PSE code $s$ has been setted as:

$$s = k\frac{\frac{1}{|\alpha_r|} - \Delta x}{2} \tag{2.43}$$

$k$ is a constant value who must be grater then 1, in our computations its value is fixed to $k = \frac{3}{4}$. The stabilization procedure has been validated performing the stability analysis to an incompressible test case, $M_j = 0.01$, developed by Yen and Messersmith (1998)[133]. In figure 2.3 the computation were performed for two different step sizes $\Delta x = 0.02,\ 0.05$.

The results for the original PSEs dropping out the term $\frac{\partial p}{\partial x}$ are presented in red, the results for the stabilized PSE are presented in black. Considering the minimum step size of reference, $\Delta x_{min}$ is around 0.2, as can be seen there, the solution in red become unstable for values of $\Delta x_{min}$ ten times smaller. Otherwise using the stabilizing procedure the solution converge for any value of $\Delta x_{min}$. We can conclude that numerical instability was absent when using the stabilized PSE approach.

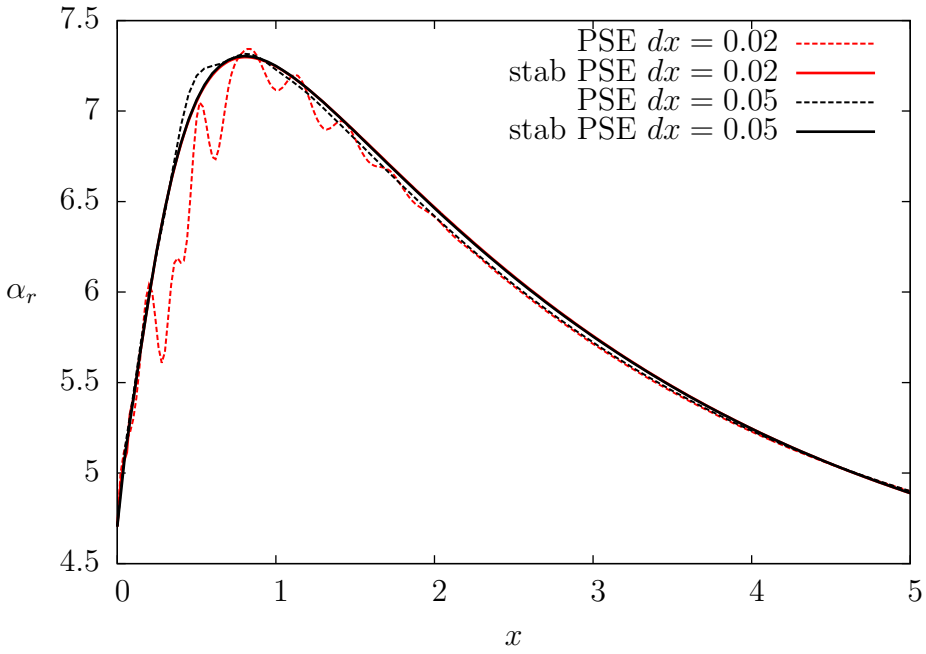


Figure 2.3: Effect of streamwise step size on the growth rates of an incompressible flow[133], $M_j = 0.01$. In full lines the PSE are computed with the stabilization procedure, in dash-lines the PSE are computed dropping out the term $\frac{\partial p}{\partial x}$.

## 2.2 Applications

### 2.2.1 Case I: incompressible semi-empirical single jet

The subsonic base flow is determined from the analytical expression given firstly by Crow and Champagne[27] and found as well in Piot et al. [98] and Yen and Messersmith [133]. The mean flow is given by:

$$\bar{u}_x = \frac{1}{2}\left\{1 + \tanh\left[\frac{1}{8\Theta}\left(\frac{1}{2r} - 2r\right)\right]\right\} \qquad \text{with} \qquad \Theta = 0.03x + 0.02$$

where $\Theta$ is the local momentum thickness.

The non-dimensional mean pressure and density are assumed uniform in the computation domain and respectively equal to $\bar{p} = 1/(\gamma M^2)$ and $\bar{\rho} = 1$. The mean radial velocity $\bar{u}_r(x, r)$ is computed from the continuity equation.

Figure 2.4 shows the computed axial velocity. The edge of the potential core and of the shear layer are identified by the two dash-dot lines. The computational domain, ($\Omega$), is 10 diameters in the streamwise direction and 8 in the radial direction.

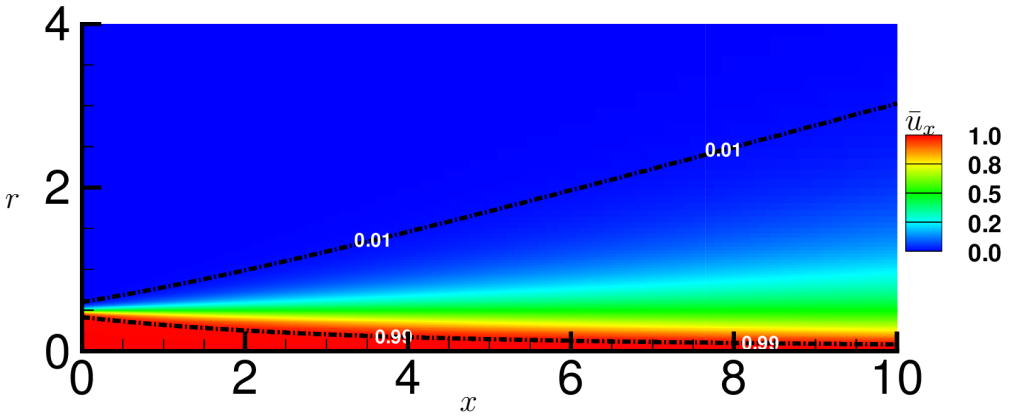


Figure 2.4: Spatial distribution of the mean axial velocity, $M_j = 0.01$. In dash-dot lines the boundary of potential core and the boundary of the shear layer.

The computations were performed for the axisymmetric instability mode, $m = 0$ and a Strouhal number of $St = 0.6$. In figure 2.5 the Local Stability Analysis is computed at the initial position, $x = x_0$. An unstable Kelvin-Helmholtz mode is clearly identified with $\alpha = 4.7 - 4.0i$. This value of $\alpha$ is used to initialize the PSE computation.

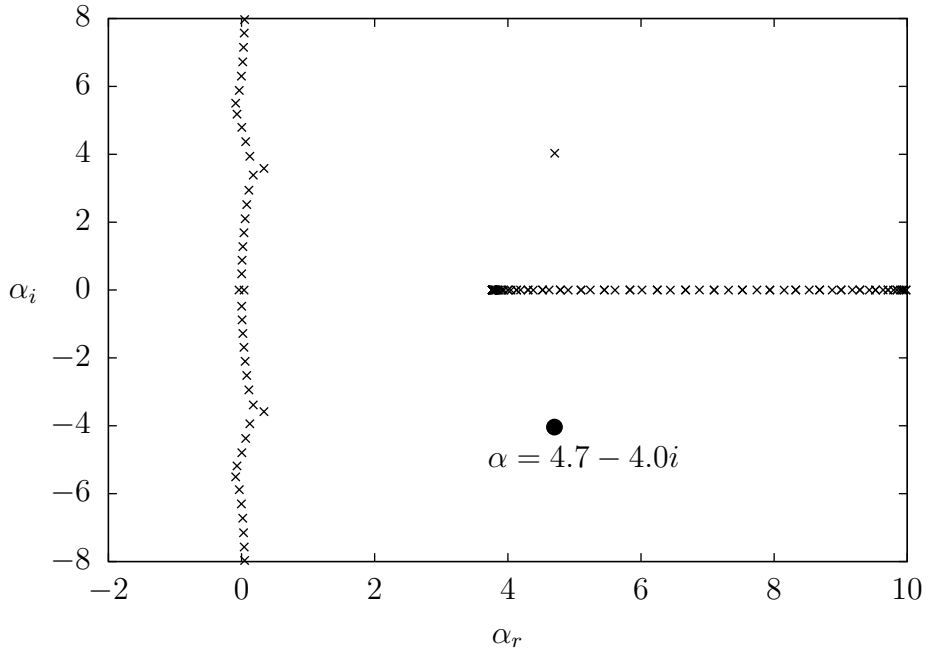


Figure 2.5: Stability spectrum for the incompressible subsonic jet, $M_j = 0.01$ at the axial position $x = x_0$ for Strouhal number $St = 0.6$ and for azimuthal wavenumber $m = 0$. In full circle the unstable modes related to Kelvin-Helmholtz instability.

Results of this configurations are shown in figure 2.6 where a comparison with the pioneer work of [133] is plotted. Figure 2.6 shows the axial evolution of the real and imaginary part of the streamwise wavenumber $\alpha$. The full line displays the results from our computations and black circles come from Yen and Messersmith [133]. The discrepancy between the computations close to the exit of the nozzle vanishes rapidly after few computational steps. This difference is due to different initial conditions. Indeed, in this work the PSE are initialized using LST. The imaginary part of $\alpha$ becomes positive around the value $x = 2.7$.

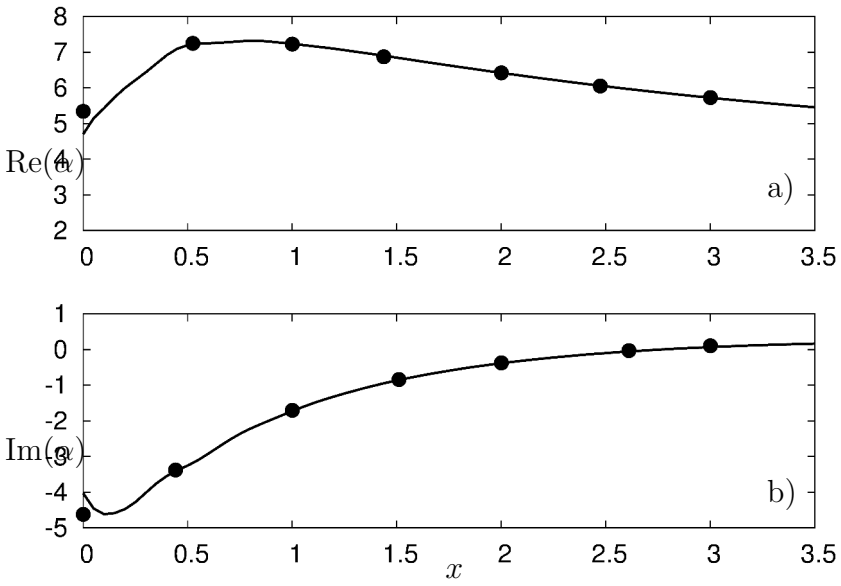


Figure 2.6: Comparison between present PSE and Yen et Messersmith PSE(•), 1998. a) Real part of $\alpha$, b) Imaginary part of $\alpha$ for a subsonic flow with $\omega = 1.2\pi$ and $m = 0$. See also [133].

Figure 2.7 shows the spatial distribution of the modulus of the pressure perturbation $p'$, $|p'|$. The perturbation increases in the unstable regions of the flow ($Im(\alpha(x)) < 0$) until $x = 2.7$ and damp down when the flow becomes stable.

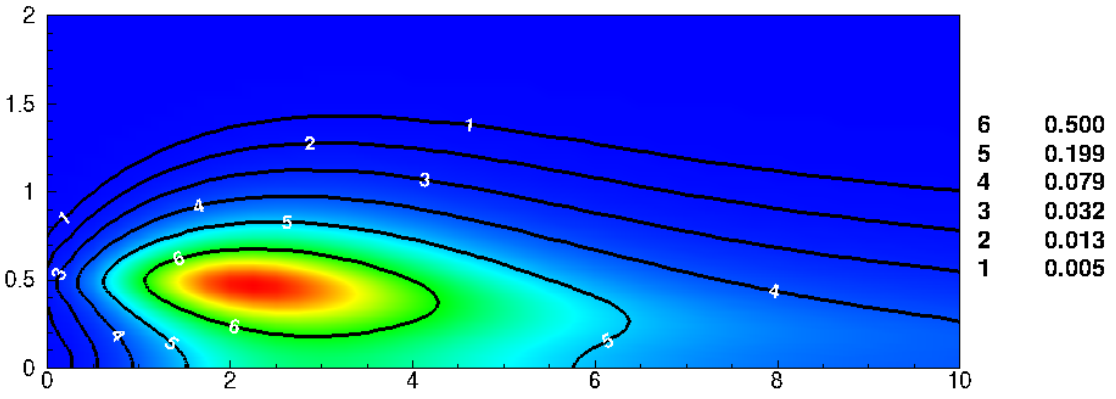


Figure 2.7: Spatial distribution of the modulus of the perturbation $|p'|$ for the Strouhal number $St = 0.6$, and azimuthal wavenumber $m = 0$ the pressure growth in the unstable regions of the jet and fall-down for high values of the streamwise coordinates where the flow is stable.

### 2.2.2 Case II: Supersonic semi-empirical single jet

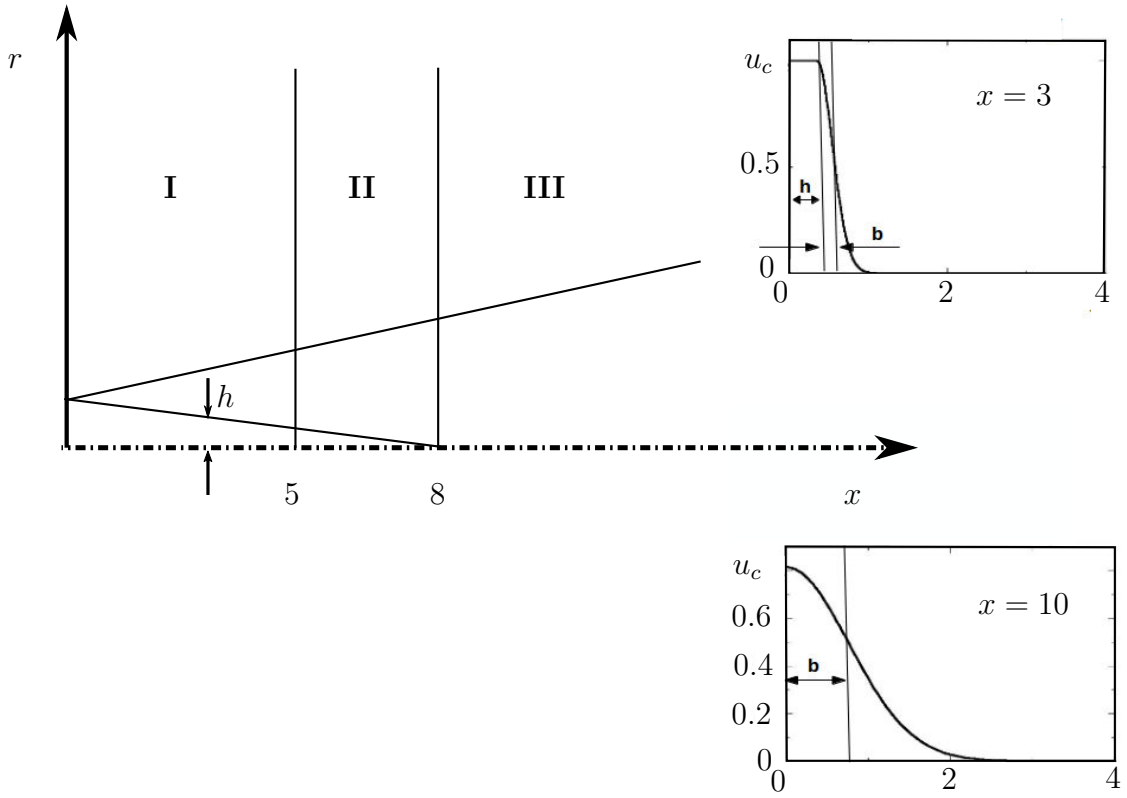


Figure 2.8: The jet has been divided into three regions I, II and III. They are called respectively the core, the transition and the developed regions.

For the supersonic case the based flow refers to a semi-empirical supersonic experimentation introduced by Tam et Burton (1984)[123] and often used in literature [134, 14, 64] for stability studies. The base flow is based to the measurements of Troutt and McLaughlin (1982)[129]. The computational domain, $\Omega$, is 20 diameters in the streamwise direction and 20 in the radial direction.

The computations of this base flow are performed for a perfectly expanded jet at Mach number $M_j = 2.1$. As depicted by Tam and Burton[123], the flow is divided into three regions as following:

1. Region I (or core region): $0 < x < x_t$

$$\bar{u}_x = \begin{cases} 1 & r < h \\ \exp\left[-\ln 2 \left(\dfrac{r - h(x)}{b(x)}\right)^2\right] & r \geq h \end{cases} \tag{2.44}$$

2. Region II (or transitional region): $x_t \leq x < x_d$

$$\bar{u}_x = \begin{cases} u_c(x) & r < h \\ u_c(x) \exp\left[ -\ln 2 \left( \dfrac{r - h(x)}{b(x)} \right)^2 \right] & r \geq h \end{cases} \tag{2.45}$$

3. Region III (or fully developed region): $x \geq x_d$

$$\bar{u}_x = u_c(x) \exp\left[ -\ln(2) \left( \frac{r}{b(x)} \right)^2 \right] \tag{2.46}$$

$h(x)$ is the radius of the uniform core and $b(x)$ is the distance from the half velocity location to the edge of the core. $u_c$ is the centerline velocity. The function $b(x)$ is determined by a cubic spline from the experimental results of McLaughlin (1980) [80], see figure 2.9.

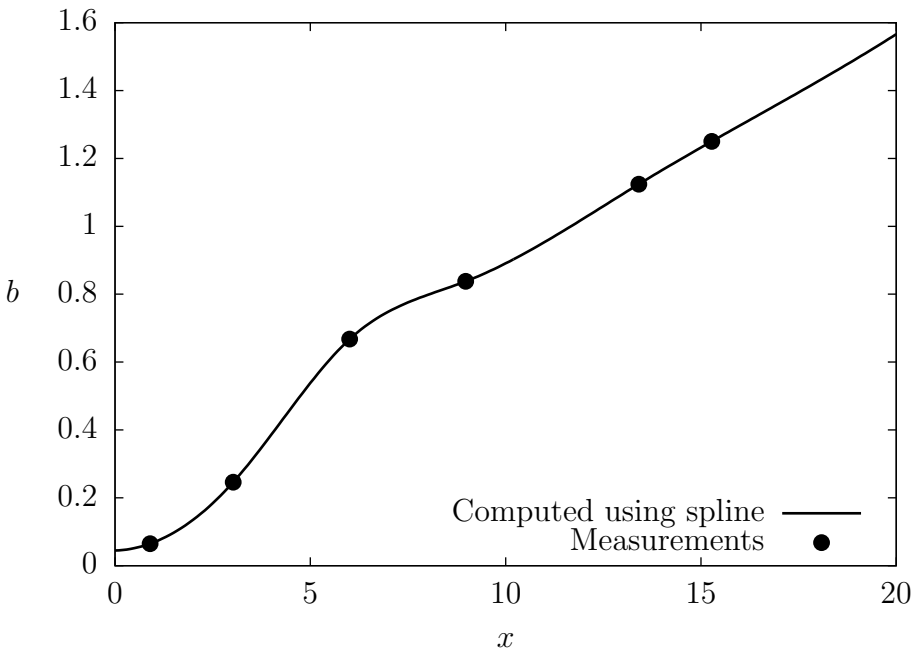


Figure 2.9: Axial distribution of mean velocity profile parameters $b(x)$.

From McLaughlin (1980)[80] work it is also found that the core region extends up to five diameters, $x_t = 5$ and the fully developed region starts at 8 diameters to the end of the nozzle $x_d = 8$. The value of $h$ in the core region and $u_c$ in the fully developed region are obtained imposing the conservation of axial momentum flow:

$$\int_0^\infty \bar{\rho} \bar{u}_x^2 \, r \, dr = \text{constant at all axial stations} \tag{2.47}$$

In region II $h$ and $b$ are determined by a cubic interpolation. The coefficients of the cubic polynomial are chosen such that $h$ and $u_c$ and their first derivatives in $x$ are continuous. The density distribution $\bar{\rho}$ is obtained by solving Crocco-Busemann law:

$$\begin{aligned} \bar{\rho} &= \left[-C_1\bar{u}_x^2 + C_3\bar{u}_x + C_2\right] \\ C_1 &= \frac{\gamma-1}{2}M_j^2, \quad C_2 = \frac{T_a}{T_t}(1+\frac{\gamma-1}{2}M_j^2) \\ C_3 &= C_1 - C_2 + 1. \end{aligned} \tag{2.48}$$

Where $M_j$ is the Mach jet number ($M_j = 2.1$), $T_t$ the total temperature and $T_a$ the ambient temperature. The total temperature is set identical to the temperature of the ambient air ($T_t = T_a$).

The radial velocity $\bar{u}_r$ is obtained by solving continuity equation with integral approach:

$$\bar{u}_r = -\frac{1}{\bar{\rho}r}\int_0^r \frac{\partial\bar{\rho}\bar{u}_x}{\partial x} r dr \tag{2.49}$$

The corresponding distribution of centreline velocity $u_c$, or $\bar{u}_x(x,0)$, of the three empirical velocity profiles eqs. 2.44-2.46, determined by the principle of conservation of momentum flux, is shown in figure 2.10. As can be seen, the calculated value of $u_c$, agrees favourably with the measurements of Troutt (1978)[128] for this particular configuration.

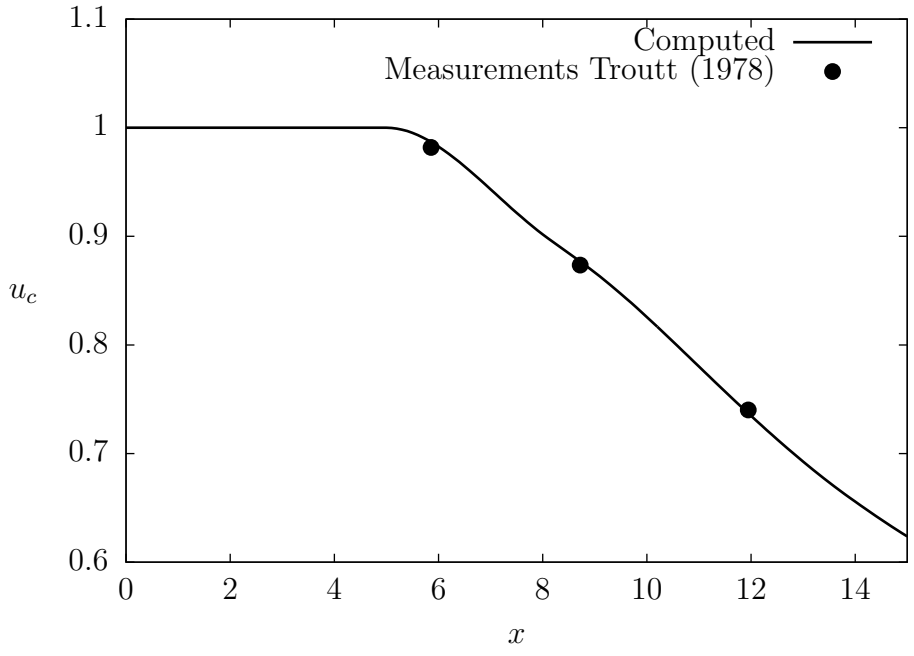


Figure 2.10: Axial distribution of mean centerline velocity $u_c(x)$.

In figure 2.11 illustrates the computed results for the parameters $b(x)$, $h(x)$ and $u_c(x)$. This results are validated by comparison with the previous works of Yen and Messersmith (1999)[134] and Léon (2012)[63].

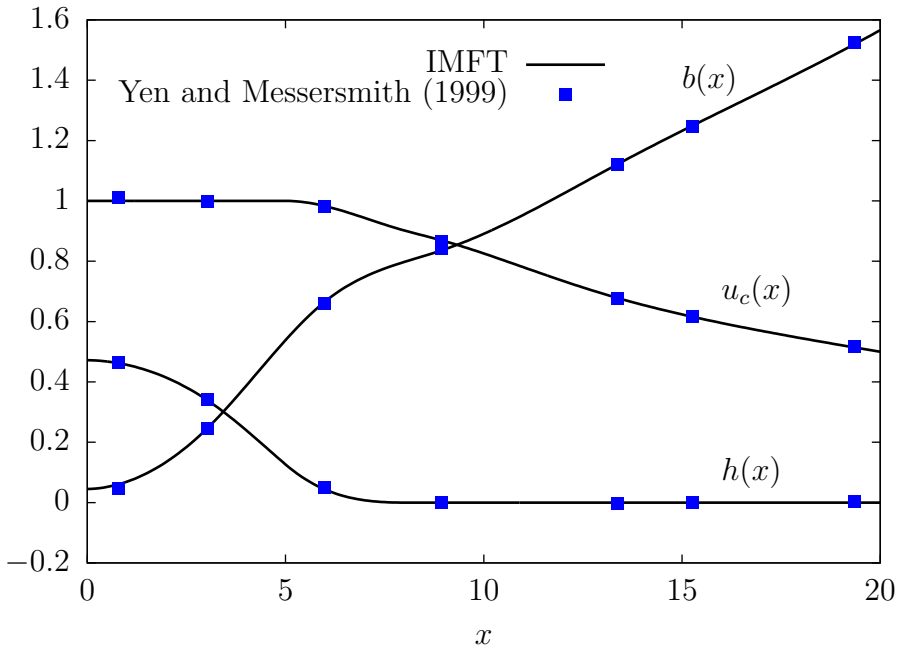


Figure 2.11: Validation of the parameters $u_c$, $b$, $h$ by comparison with Yen and Messersmith (1999)[134] results.

Figure 2.12 shows the computed axial velocity. The edge of the potential core and of the shear layer can be clearly identified by the two dash-dot lines.

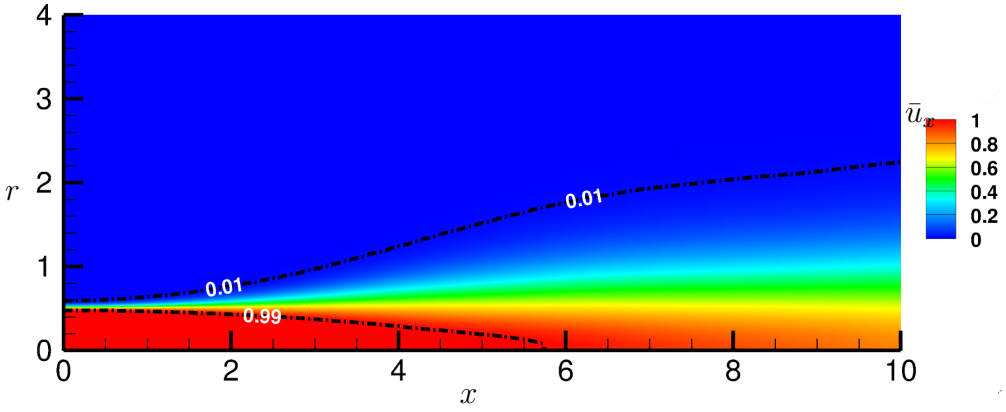


Figure 2.12: Spatial distribution of the mean axial velocity, $\bar{u}_x$, at $M_j = 2.1$. In dash-dot lines the boundary of the potential core and the boundary of the shear layer.

The computed distribution of the mean radial velocity profile at several axial locations, $x = 0, 5, 15, 20$ is shown in figure 2.13. The streamwise variation of the mean radial velocities denotes the spreading of the shear layer. The small amplitude of the radial velocity (less then 3% of the jet exit velocity) is typical for unidirectional flows.

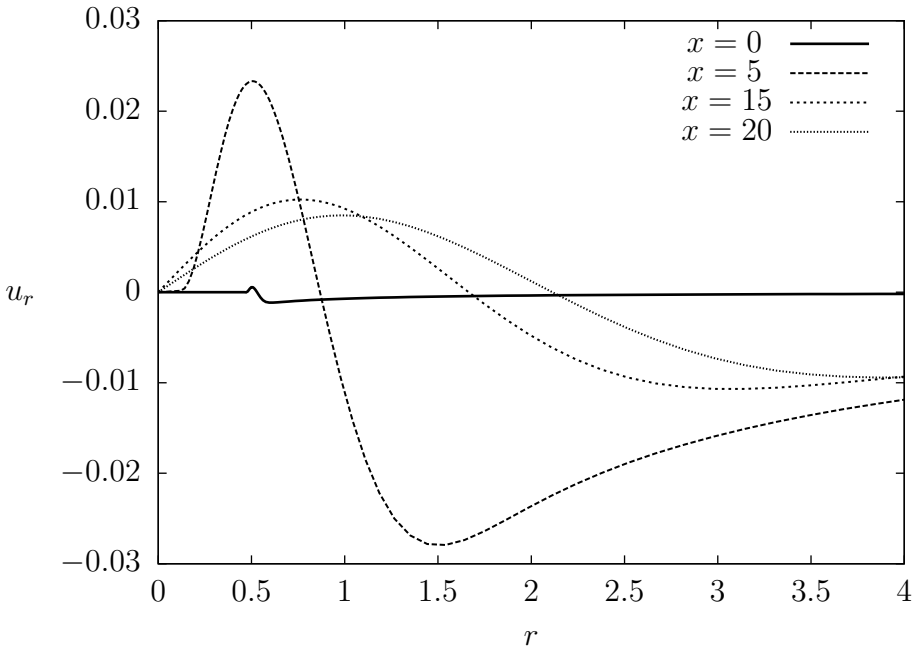


Figure 2.13: The streamwise variations of radial profiles of mean radial velocities, $\bar{u}_r$.

After the mean flow profiles are obtained, the evolution of the disturbances inside the jet is computed using the PSE approach. The instability wave examined include the axisymmetric and first helical modes, which are excited at frequencies $St = 0.2$ and 0.4. The system is initialized by computing the LST at the beginning of the computational domain, in $x = x_0$. Stability spectrum for Strouhal number, $St = 0.2$, is shown in figure 2.14, because of the convention sign used in this thesis the modes related to Kelvin-Helmholtz instability is identified in the second quarter of the Cartesian plane by observing the stability spectrum. The only physical unstable modes at this frequency is $\alpha = (1.50 - 0.45i)$.

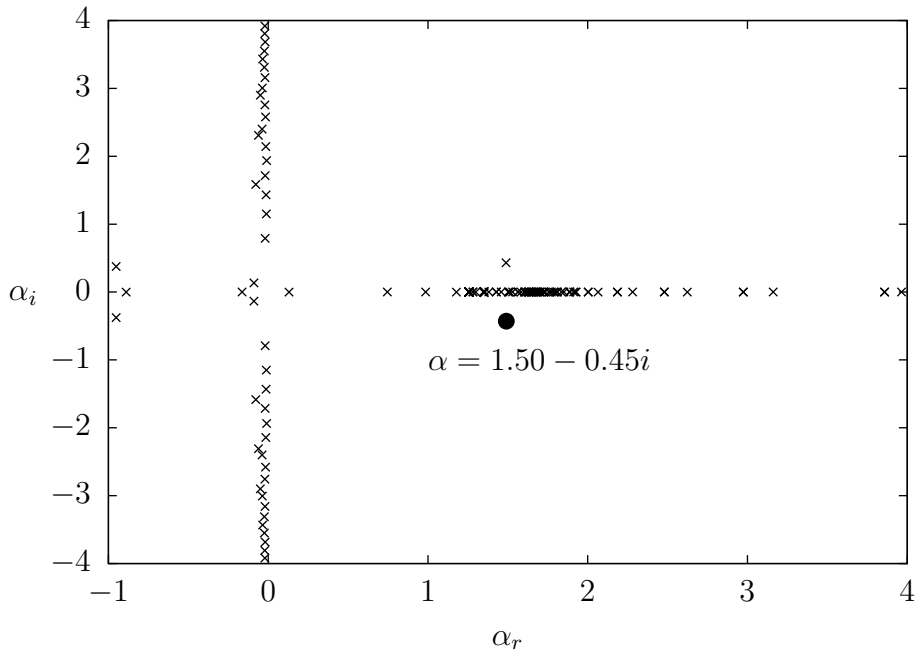


Figure 2.14: Stability spectrum of the semi-empirical supersonic jet, $M_j = 2.1$ at the axial position $x = x_0$ for Strouhal number $St = 0.2$ and for azimuthal wavenumber $m = 0$. In full circle the unstable modes related to Kelvin-Helmholtz instability.

Figure 2.15 shows the amplitude of the axisymmetric pressure distribution in the axial direction inside the shear layer at the radial location $r/D = 0.5$ for Strouhal number $St = 0.2$ and $St = 0.4$. The perturbation $p'$ has been scaled in such a way that $|p'|_{max} = 0.01$ at $x = x_0$. The results shown a reasonable agreement with respect to our results. Differences could be explained considering that Yen and Messersmith[134] used the linearized Navier-Stokes equations to analyse the behaviour of the disturbances $\boldsymbol{q}'$ instead of the Linearized Euler Equations (LEE). We observe the pressure peaks at about $x/D = 7$ and decrease further downstream.

Figure 2.16 show the global evolution of the real part of the pressure wave with $St = 0.2$ and 0.4 for the axisymmetric mode, $m = 0$. The shorter wavelength can be seen when comparing PSE computation at $St = 0.4$, figures 2.16(c)-2.16(d) with respect to the lower frequency $St = 0.2$, figures 2.16(a)-2.16(b). Computation have been done by considering the term $\frac{\partial p}{\partial x}$, thanks to the stabilization procedure, Figures 2.16(a)-2.16(c), and by dropping out the mean pressure streamwise derivative, Figures 2.16(a)-2.16(c). As expected results are quite close each others. The oscillatory behavior of the perturbation pressure waves is clearly shown in both the streamwise and radial directions. The RMS values of the perturbation pressures in figure 2.16 are shown in figure 2.17. In the experiment of Troutt and McLaughlin (1982)[129] three dominant instability wave modes are excited simultaneously, $m = 0$ and $m = \pm 1$. Indeed, to compare with our results additional computation to the first helical modes is required (fig. 2.18). The directivity is estimated from the RMS pressure contours. If the term $\frac{\partial p}{\partial x}$ is not neglected the solution seems to

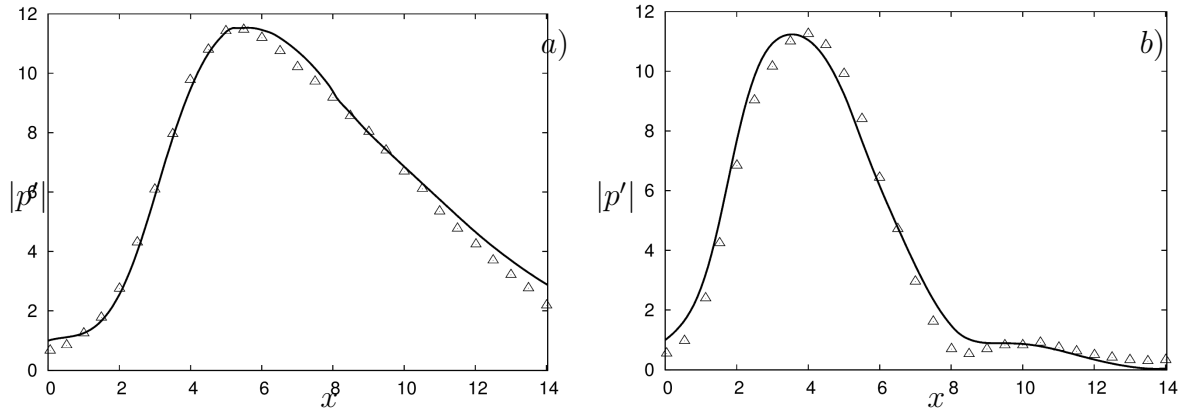


Figure 2.15: Absolute pressure values at $r/D = 0.5$ obtained by PSE computations (full lines) are compared with Yen and Messersmith [134] results (△). Comparisons have been done for azimuthal wavenumber $m = 0$ and for $(a)$ $St = 0.2$ and $(b)$ $St = 0.4$.

| | $m = 0;\ \frac{\partial p}{\partial x} \neq 0$ | $m = 0;\ \frac{\partial p}{\partial x} = 0$ | $m = 1;\ \frac{\partial p}{\partial x} \neq 0$ | $m = 1;\ \frac{\partial p}{\partial x} = 0$ | Exp. [129] |
|---|---|---|---|---|---|
| $St = 0.2$ | 31° | 32° | 32° | 35° | 30° |
| $St = 0.4$ | 30° | 41° | 30° | 42° | 36° |

Table 2.1: Directivity of the pressure instability waves.

have a higher directivity, also if compared with the experimental results, Tab. 2.1. Tab. 2.1 also show that PSE prediction agrees quite well to the experimental results.

Higher accuracy of the predicted directivity can be found by coupling PSE with an acoustic analogy as shown in Chapter 3.

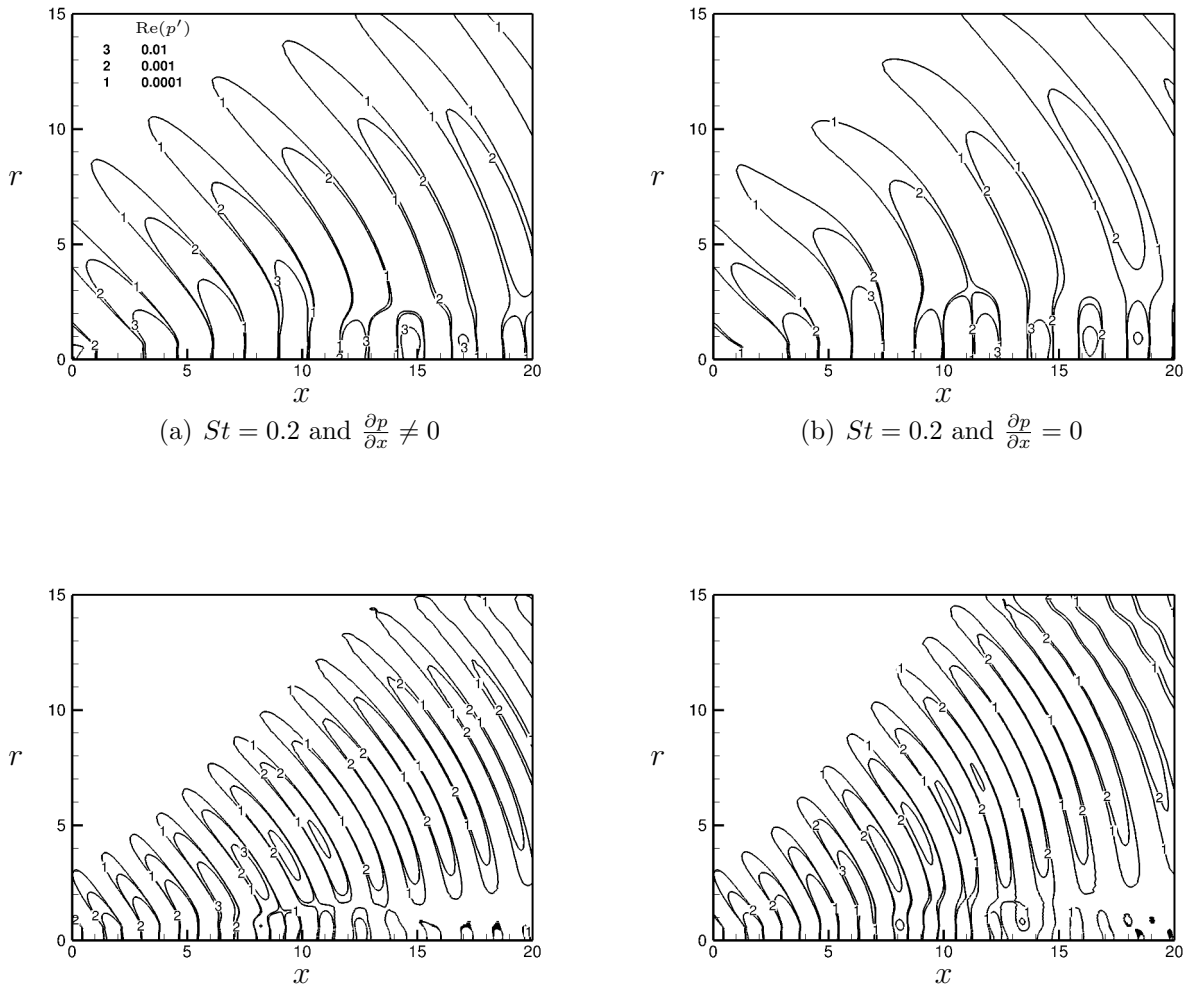


(a) $St = 0.2$ and $\frac{\partial p}{\partial x} \neq 0$

(b) $St = 0.2$ and $\frac{\partial p}{\partial x} = 0$

(c) $St = 0.4$ and $\frac{\partial p}{\partial x} \neq 0$

(d) $St = 0.4$ and $\frac{\partial p}{\partial x} = 0$

Figure 2.16: Contour lines of the pressure waves for azimuthal wavenumber, $m = 0$. Same scale for each plots.

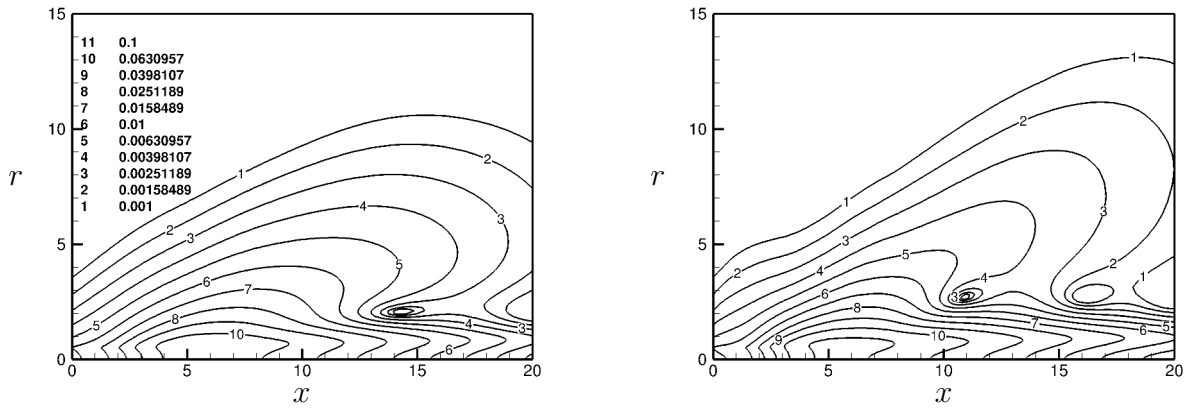


(a) $St = 0.2$ and $\frac{\partial p}{\partial x} \neq 0$ (b) $St = 0.2$ and $\frac{\partial p}{\partial x} = 0$

(c) $St = 0.4$ and $\frac{\partial p}{\partial x} \neq 0$ (d) $St = 0.4$ and $\frac{\partial p}{\partial x} = 0$

Figure 2.17: The RMS values of the pressure waves for azimuthal wavenumber, $m = 0$. Same scale for each plots.

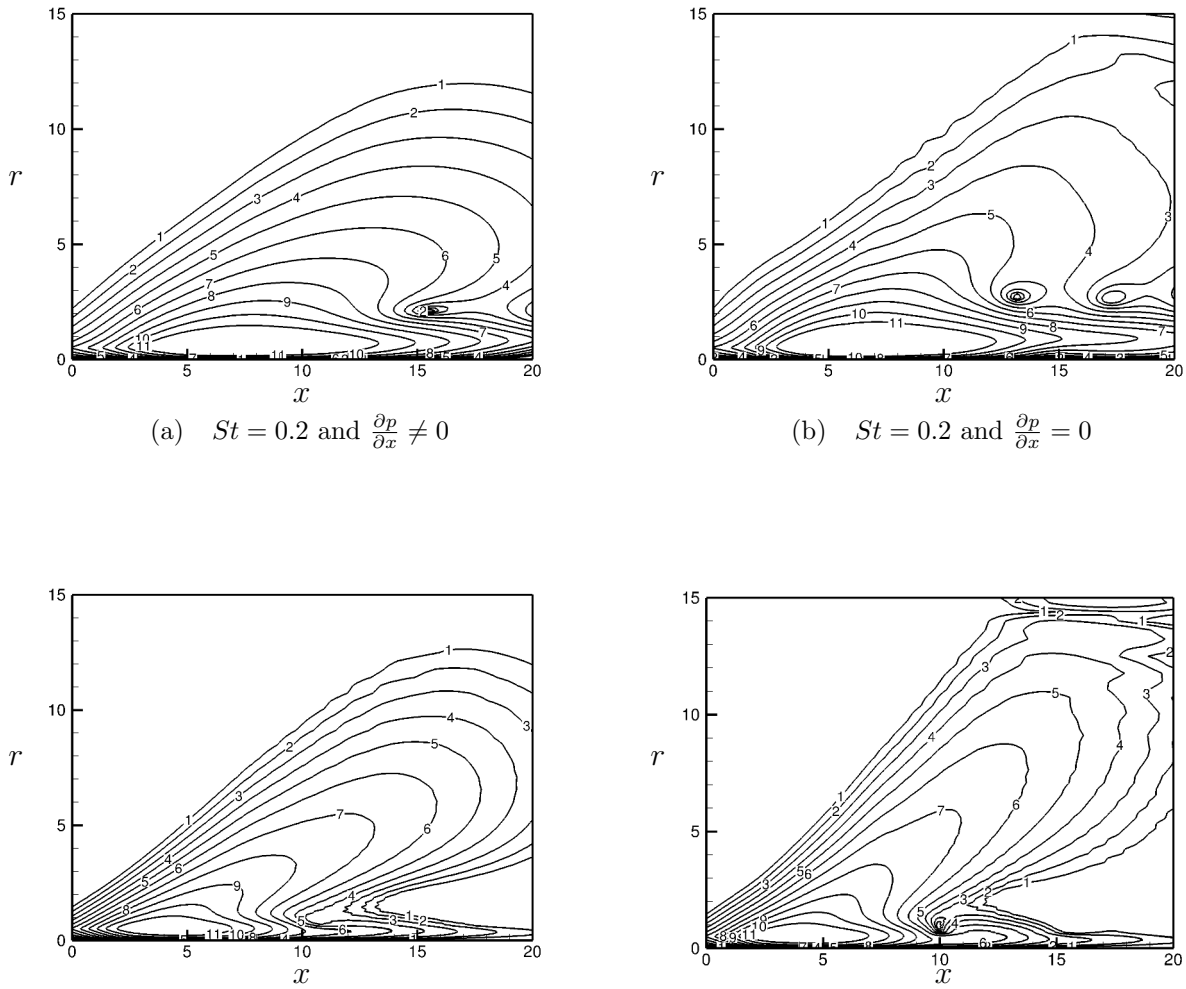


(a) $St = 0.2$ and $\frac{\partial p}{\partial x} \neq 0$

(b) $St = 0.2$ and $\frac{\partial p}{\partial x} = 0$

(c) $St = 0.4$ and $\frac{\partial p}{\partial x} \neq 0$

(d) $St = 0.4$ and $\frac{\partial p}{\partial x} = 0$

Figure 2.18: The RMS values of the pressure waves for azimuthal wavenumber, $m = 1$.

### 2.2.3 Large Eddy Simulations

This section shows how stability analysis is applied to a turbulent supersonic under-expanded single and dual-stream jet. The main characteristic of under-expanded jets is the formation of a system of shock-cells at the exit of the nozzle that allows the jet to progressively expand to ambient conditions. This system is formed by a series of expansion and compression waves that bounce inside the potential core of the jet. The LES simulations have been carried out with the Finite Volume multi-block structured solver *elsA* (Onera's software [18]) and performed by the Early Stage Researcher (ESR3) Carlos Pérez in collaboration with CERFACS team.

### a- Case III: Turbulent single jet (TSJ)

The jet is under-expanded and at Mach number $M = 1.15$. Its Reynolds number is $Re = 10^6$. This configuration has been tested experimentally by André [9]. The shock-cells manifested in the core of the flow, as seen in figure 2.19, interact with the instabilities around the potential core producing an intense noise as explained in Ray (2007)[103].

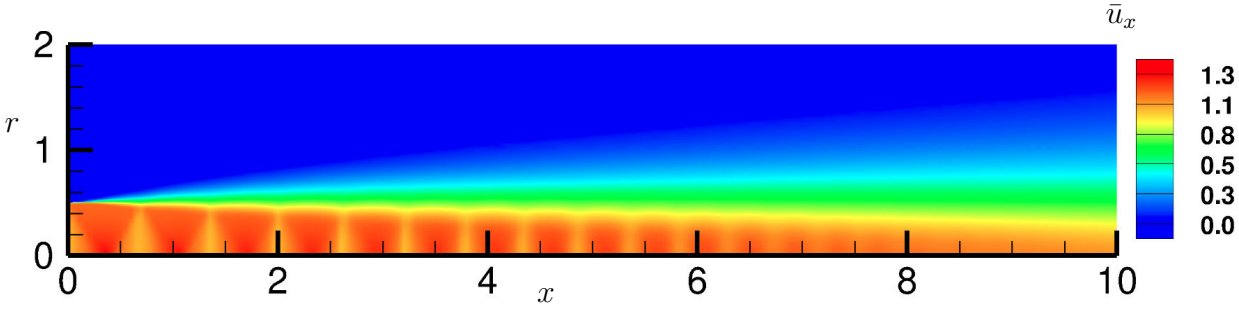


Figure 2.19: Spatial distribution of the mean axial velocity computed by LES. The shock-cells are distributed along the streamwise direction in the core of the jet.

Pressure perturbations are propagated to the far-field by means of the FWH analogy using the data on a topological surface located at $r/D = 3$. The results are shown in figure 2.20 $(a)$ at different angles and compared with the experimental data of André [9].

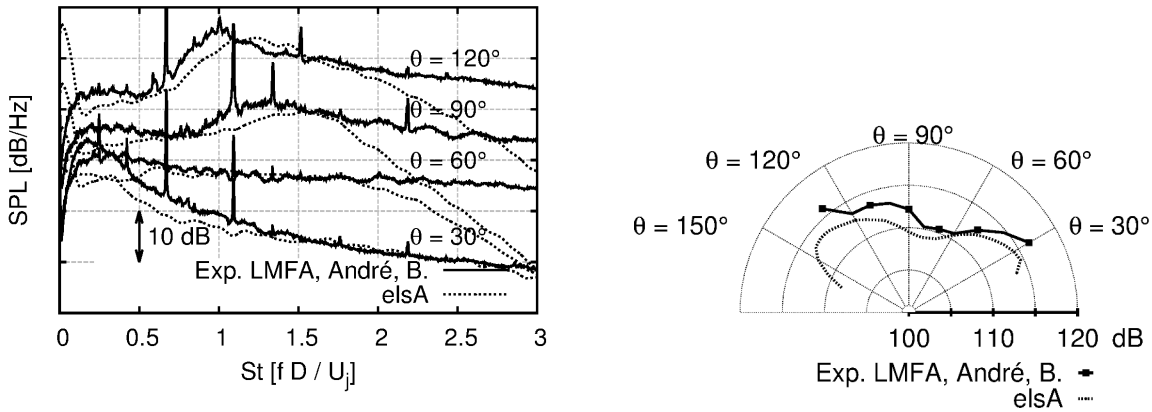


(a) (b)

Figure 2.20: Acoustic spectrum in the far-field (50 diameters) for a $M_j = 1.15$ under-expanded jet. $\theta$ is measured with respect to the jet axis, **(a)** SPL, **(b)** OASPL. From Arroyo (2016)[94]

The SPL is in good agreement up to the mesh cut-off Strouhal. The Overall Sound Pressure Level (OASPL) is computed and compared with the experimental data in figure 2.20 $(b)$. The simulation, being able to capture the main noise contributions of an under-expanded single jet, is a perfect base-flow to compute the stability and sensibility analysis.

From the LES data, temporal and azimuthal means have been done by C.E.R.F.A.C.S. laboratory in order to produce the steady base-flow (fig. 2.19) on which the analysis is performed. A fit procedure was required as well to smooth the small variation of the parameters obtained when means of the LES results is done. This fit procedure has been developed using a Gaussian procedure implemented in the MATLAB function "fit" to avoid strong oscillations in the first derivative of the parameters, but at the same time, the physic and the behaviour of the base-flow stay unchanged.

The stability results presented here refer to axysimmetric instabilities with $m = 0$. The PSE computation has been initialized at the streamwise position $x = x_0$ and for a Strouhal number of $St = 0.890$ using Linear Stability Equations.

Figure 2.21 shows the spatial distribution of the pressure perturbation $p'$ at the nondimensional time $t = n/St$, where $n$ is an integer number. The perturbation increases in the unstable regions of the flow ($Im(\alpha(x)) < 0$) and damp down when the flow becomes stable. The spatial wavelength $\lambda = 2\pi/Re(\alpha)$ can also be guessed in the figure.

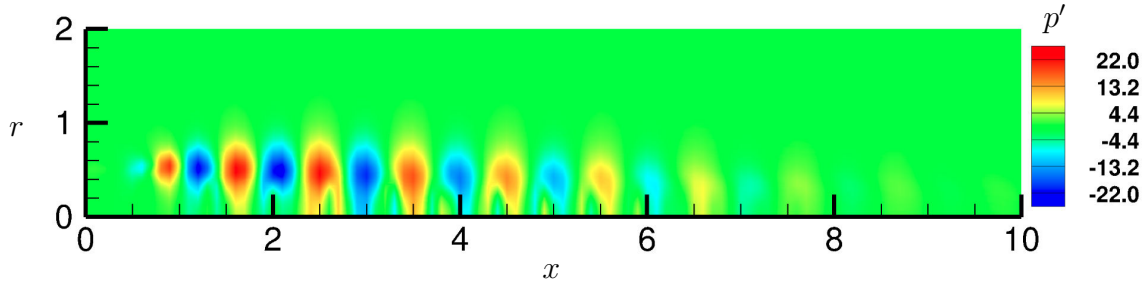


Figure 2.21: Spatial distribution of the real part of the perturbation $p'$, Re($p'$) for the Strouhal number $St = 0.89$, the pressure growth in the unstable regions of the jet and fall-down for high values of the streamwise coordinates where the flow is stable.

The influence of the frequency or Strouhal variations has to be studied since the André's experimental spectrum (fig. 2.20) exhibits two screech noise frequencies [9]. The real and imaginary part of $\alpha$ are plotted on figure 2.22. The frequency dependence on the real wave number is obvious, and the shock cells locations are visible in the range of $x = 2$ to $x = 8$. It is natural since the stability properties are very sensitive to any mean flow variations. The variation of the frequency on the growth rate Im($\alpha$) are quite important close to the nozzle exit. Then, it seems that the growth rate is governed by the shock cells and not by the frequency. Downstream, when shock cells are weak, the growth rate tends to frequency independent (in the range of the study).

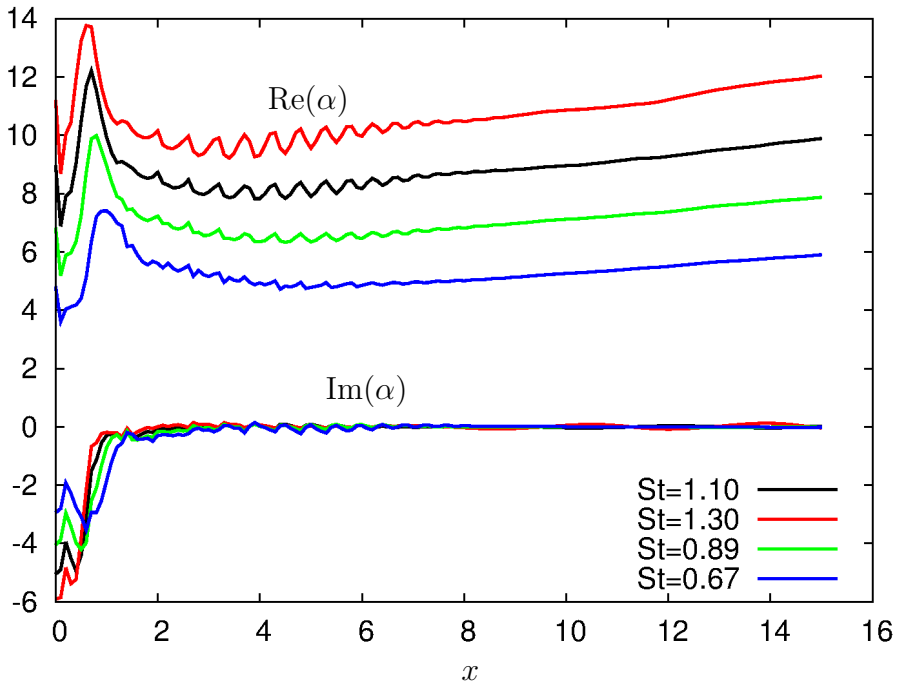


Figure 2.22: Axial distribution of the streamwise wave-number $\alpha$ for different values of the Strouhal number, respectively $1.10, 1.30, 0.89, 0.67$

### b- Case IV: Turbulent dual-stream jet (TDSJ)

The test case proposed is related to an application of interest within the current aeroacoustic research on jet noise reduction from civil aircraft. In figures 2.23 and 2.24 the flow conditions and the geometry of the nozzle are respectively specified. The geometry is the one of a dual stream axial symmetric jet with coaxial nozzles for the primary and secondary flow. Both the primary and secondary stream flow through conical plain convergent nozzles and the exit sections are staggered, with the external and the internal cowl deflecting respectively by a 12° and 14° angle towards the jet axis. The bypass flow exits the nozzle 0.021 $m$ upstream the primary nozzle exit section and the secondary jet diameter is more than double the internal one. The design does not include the use of any plug and the nozzle is conceived with a fixed geometry in mind. As the numerical predictions would be compared with experiments performed at the Von Karman Institute for Fluid Dynamics, the total mass flow rate is dictated by the facility performance of the experiment, giving a value of 1.09 $kg/s$ at target test point. The secondary flow is sonic at the nozzle exit section of the convergent duct, therefore experiencing a considerable degree of under-expansion, causing the jet to be characterised by the of a shock cell system similar to the observed for the single under-expanded test case 2.2.3. The primary flow is also affected by a train of shock cell structures, figure 2.25(a), which prevents the perfectly expanded condition to be reached. Very few examples of stability analysis of dual stream jet can be found in literature. A parameter study was published by Viswanathan (2004)[130] and an investigation on the shock cell system in a dual flux

jet has been performed by Tam et al. (2008)[120]. This test case is of great interest in the current aerodynamic and aeroacoustic research.

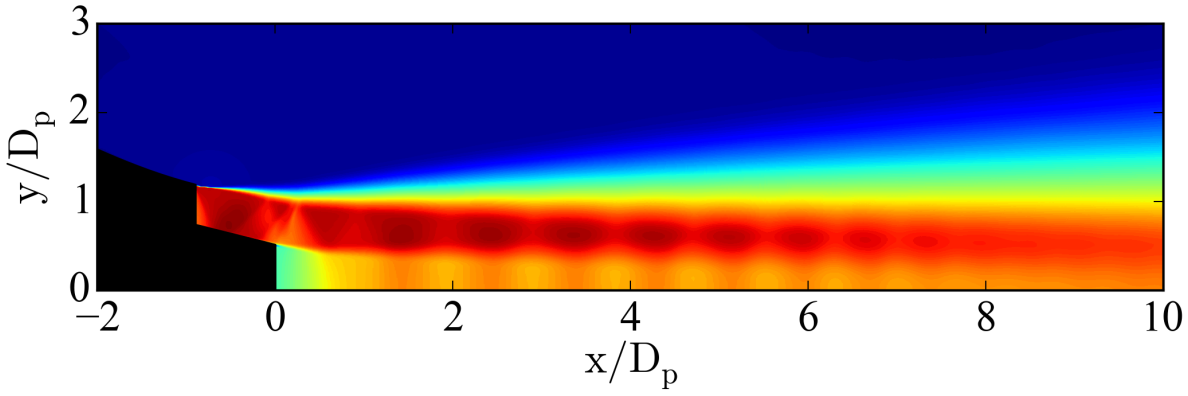


Figure 2.23: Under-expanded supersonic dual-stream jet est case. Flow conditions

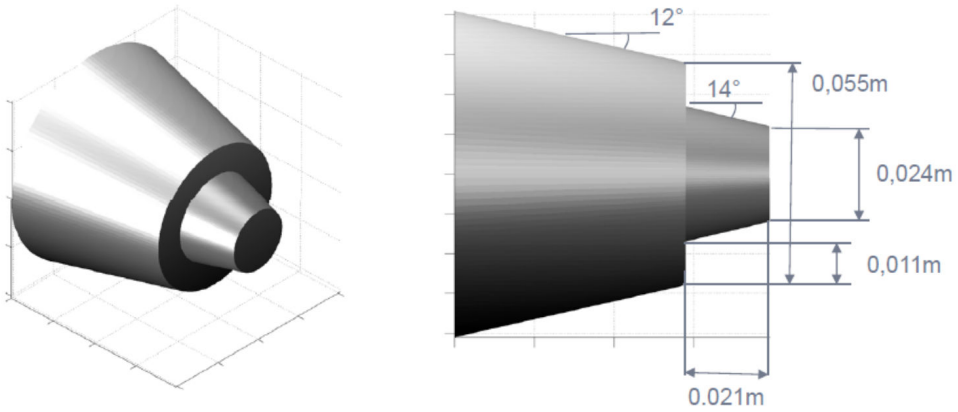


Figure 2.24: Under-expanded supersonic dual-stream jet test case. Nozzle geometry.

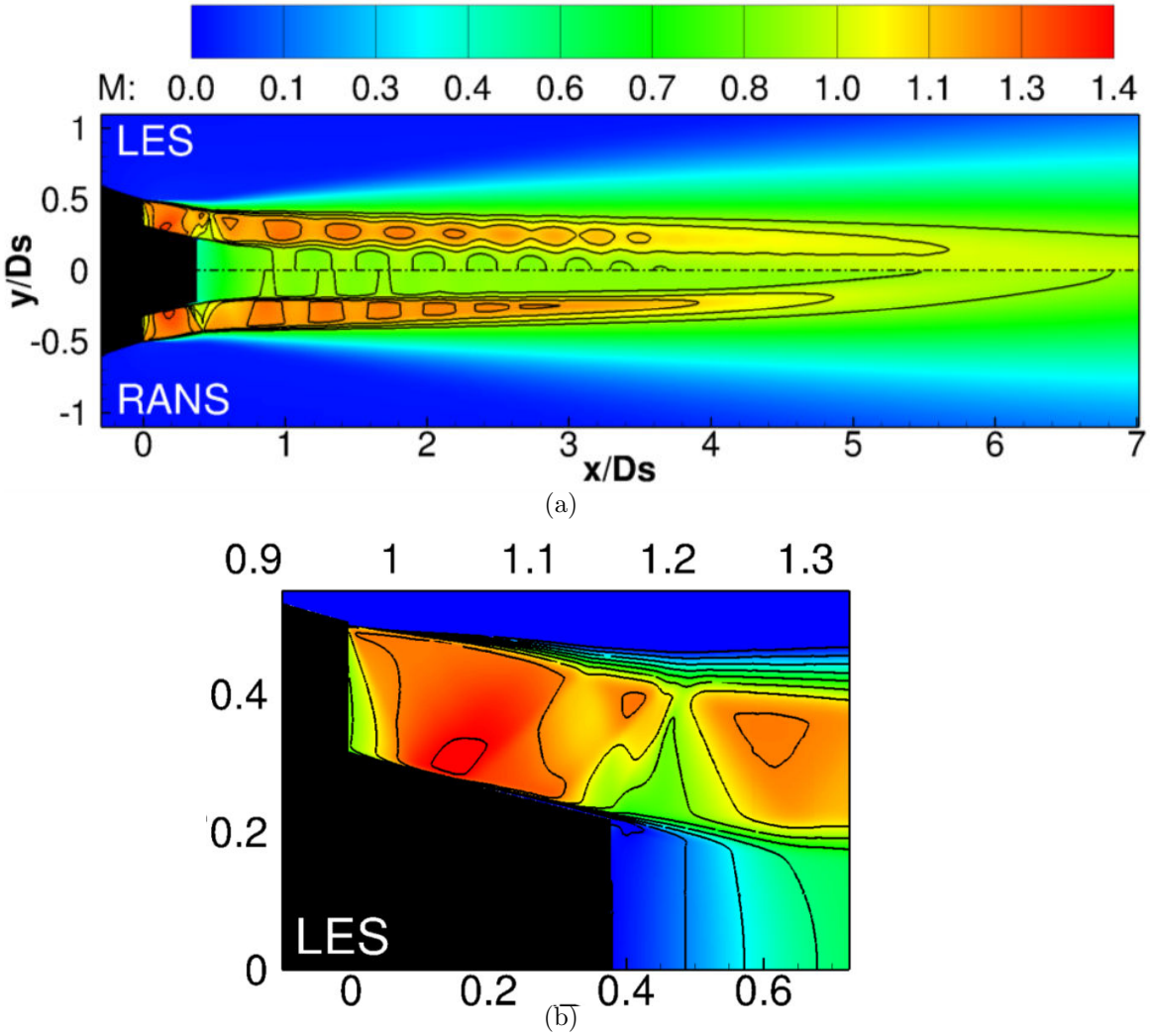


Figure 2.25: Under-expanded supersonic dual-stream jet test case. Time and azimuthal average mean axial velocity $\bar{u}_x$.

The flow conditions of the co-axial jet are: the primary flow is cold and subsonic with an exit Mach number of $Mp = 0.89$ ($CN\ P\ R = 1.675$), the secondary stream is operated at supersonic under-expanded conditions with a perfectly exit Mach number of $Ms = 1.20$ ($F\ N\ P\ R = 2.45$). Here, $CN\ P\ R$ and $F\ N\ P\ R$ stand for Core and Fan Nozzle to Pressure Ratio respectively. The jets are established from two concentric convergent nozzles with primary and secondary diameters of $D_p = 23.4mm$ and $D_s = 55.0mm$ respectively. The thicknesses of the nozzles at the exit are of $0.5mm$. The Reynolds numbers based on the jet exit diameters are $Re_p = 0.57 \times 10^6$ and $Re_s = 1.66 \times 10^6$. The ambient conditions used for this test case are a pressure $P_{amb} = 101325\ Pa$ and a temperature $T_{amb} = 283\ K$. The stagnation pressure or total pressure $P_{tp} = 1.6972 \times 10^5\ Pa$ for the primary stream and $P_{ts} = 2.4825 \times 10^5\ Pa$ for the secondary stream. The total temperature $T_t$ has been kept equal to the ambient temperature $T_{amb}$ for both streams.

The lengths are non-dimensionalized by the primary diameter $D_p$. As in the single stream jet case 2.2.3, the steady base flow is obtained by temporal and azimuthal integral average in the whole computational domain ($\Omega$) figure 2.26(a). The same fit procedure of the data implemented for the TSJ case was used. The computational domain ($\Omega$) is 30 diameters in the streamwise direction and 6 in the radial direction.

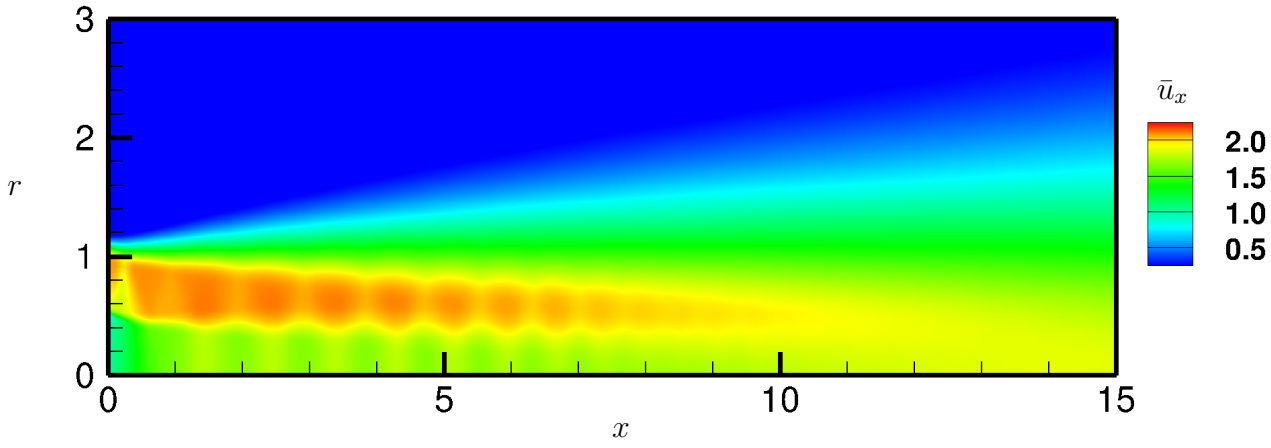


(a)

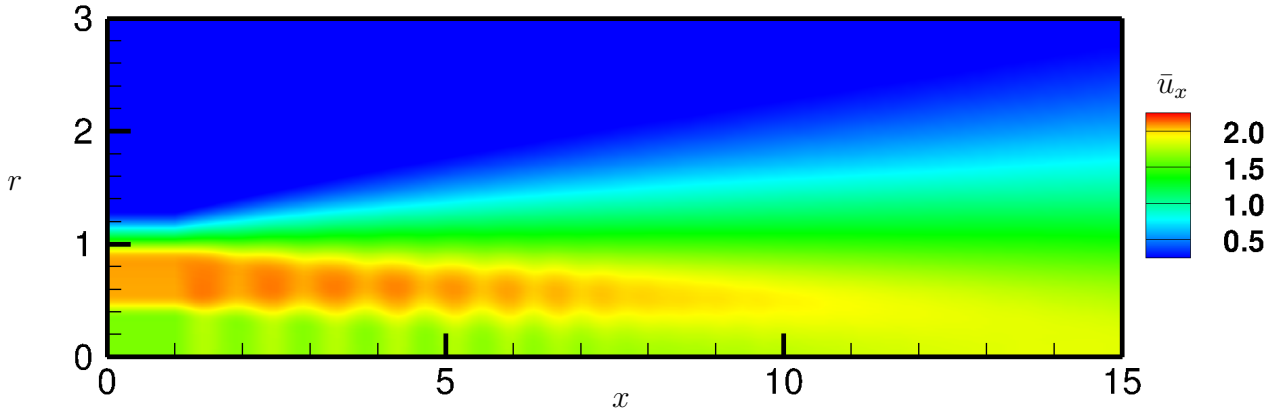


(b)

Figure 2.26: Test case under-expanded supersonic dual-stream jet. Time and azimuthal average mean axial velocity $\bar{u}_x$.

The PSE computation is initialized by a LST analysis. The choice of the initial station $x = x_0$ have been done, firstly, at the exit of the primary nozzle (test 1). Here, as example, we show the results of the eigenvalues problem obtained in the configuration of $St = 1.0$; two very distinct unstable modes are observed in the stability spectrum (fig. 2.27-a). These two modes are the hydrodynamic Kelvin-Helmholtz modes (referred to as "$KH$ modes") of the two mixing layers, $KH_1$ and $KH_2$ referring respectively to the inner and outer mixing regions. However, the strong shock that appears just at the end

of the primary nozzle produce, necessarily, a strong variation of the parameters in the streamwise direction (fig. 2.25(b)). This shock-wave destabilize the PSE computation and, moreover, clearly not satisfy the hypothesis of slow variation of the base flow in the streamwise direction. The second choice (test 2), then, dropped out the strong shock cell by imposing a parallel flow from the exit of the nozzle to $1D_p$ in the axial direction, as shown in figure 2.26(b). In figure 2.27-b is plotted the stability spectrum for this new configuration. Both $KH$ modes are much less unstable and with the imaginary part almost at the same value. The influence of the Stouhal number to those values is analysed in table 2.2

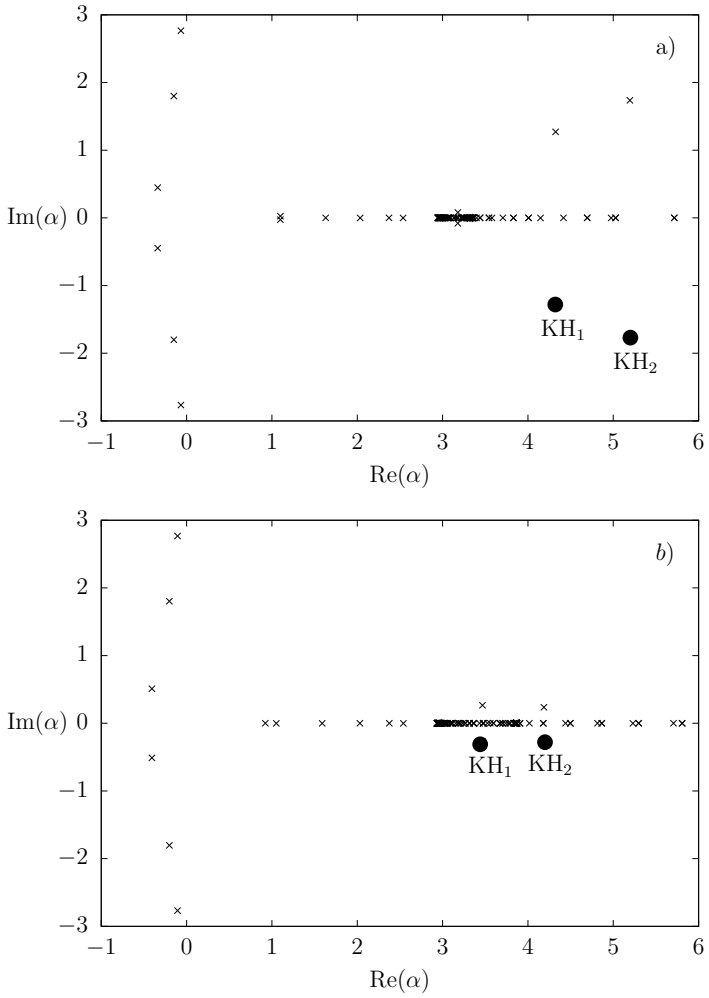


Figure 2.27: Stability spectrum of the turbulent dual-stream jet at the axial position $x = x_0$ for Strouhal number $St = 1.0$ and for azimuthal wavenumber $m = 0$. In dark point the 2 unstable modes related to Kelvin-Helmholtz instability in the primary $KH_1$ and secondary $KH_2$ jet. case a) refers to the local stability at the position $x = 0D_p$ (test 1) and case b) refers to the local stability at $x = 1D_p$ (test 2).

Results of the growth rate with respect to the two different base flows are shown in

figure 2.28. The instability behaviour of the flow and the point where the flow becomes stable, $\alpha_i > 0$ are not changing ($x = 15D_p$). Indeed, the solutions quickly converge to same values after around $3D_p$ in the streamwise direction, showing that the choice of overpass the shock wave will not affect the physics of the instability waves.

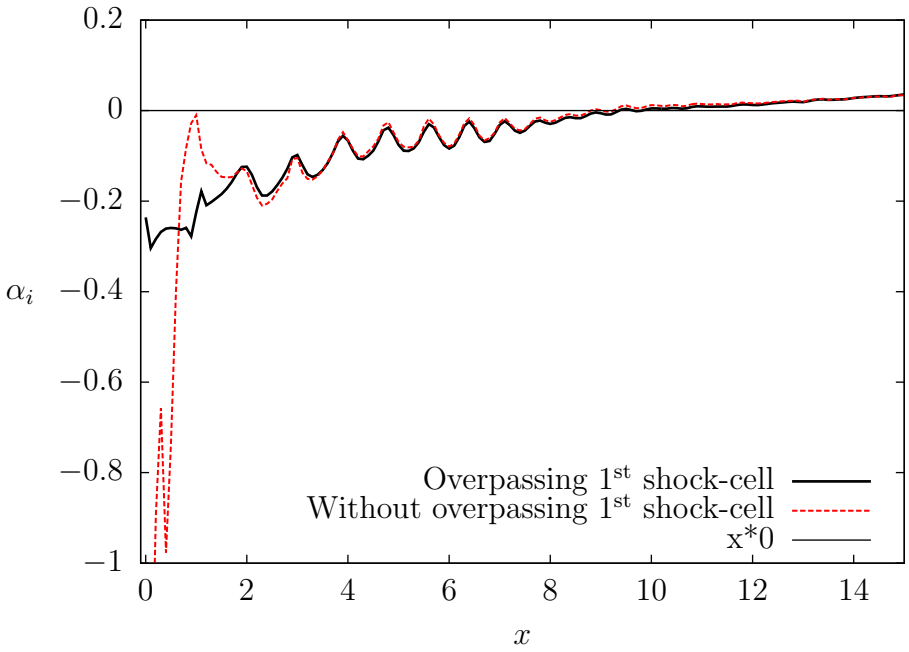


Figure 2.28: Growth rate computed for the two different baseflow. The two solutions quickly converge to the same values.

By considering this new base flow configuration a parametric analysis of the perturbation waves with respect to different values of the Strouhal number, $St$, in the case of axisymmetric instabilities $m = 0$ has been done in the following. First conclusion can be pointed out observing Tab. 2.2, where the LST analysis is computed at the beginning of the computational domain, $x = x_0$. The values of the streamwise wavenumber $\alpha$ function of the Strouhal number, $St$, show that the local growth of the $KH_2$ mode is larger than its related to $KH_1$ mode, which suggest a local dominance of the instability wave developing in the secondary jet. As expected, the real part $\alpha_r$, inversely proportional to the wavelength, decreases with the Strouhal number in the primary and in the secondary jet. The local growth rate $\alpha_i$ in the primary jet decrease with the Strouhal number and opposite behaviour is observed for the unstable modes related to the secondary shear layer, $KH_2$. This first results suggest a crucial role of the secondary jet, moreover, for small values of the Strouhal number.

| | $KH_1$ | $KH_2$ |
|---|---|---|
| $St = 1.0$ | $3.46 - 0.26i$ | $4.18 - 0.23i$ |
| $St = 0.8$ | $2.78 - 0.22i$ | $3.52 - 0.33i$ |
| $St = 0.6$ | $2.10 - 0.18i$ | $2.79 - 0.50i$ |
| $St = 0.4$ | $1.39 - 0.12i$ | $1.74 - 0.63i$ |

Table 2.2: Values of the initializing unstable Kelvin-Helmoltz modes in the inner and in the outer shear-layer for different Strouhal numbers.

Clearly, this first trend, is not fully representative of the disturbances and a PSE analysis is necessary to analyze the axial evolution of them. The frequency dependence of the real and imaginary part of the streamwise wavenumber $\alpha(x)$ are plotted in figures 2.29 and 2.30, respectively. As observed for the single stream case, the shock cells structures, clearly, influence the values of the wavenumber in particular the growth rate. The wave length $\alpha_r$ seems to be more affected by variations of the Strouhal number, $St$, if compared to the growth rate. The position where the flow becomes stable, however, change noticeably varying the Strouhal number.

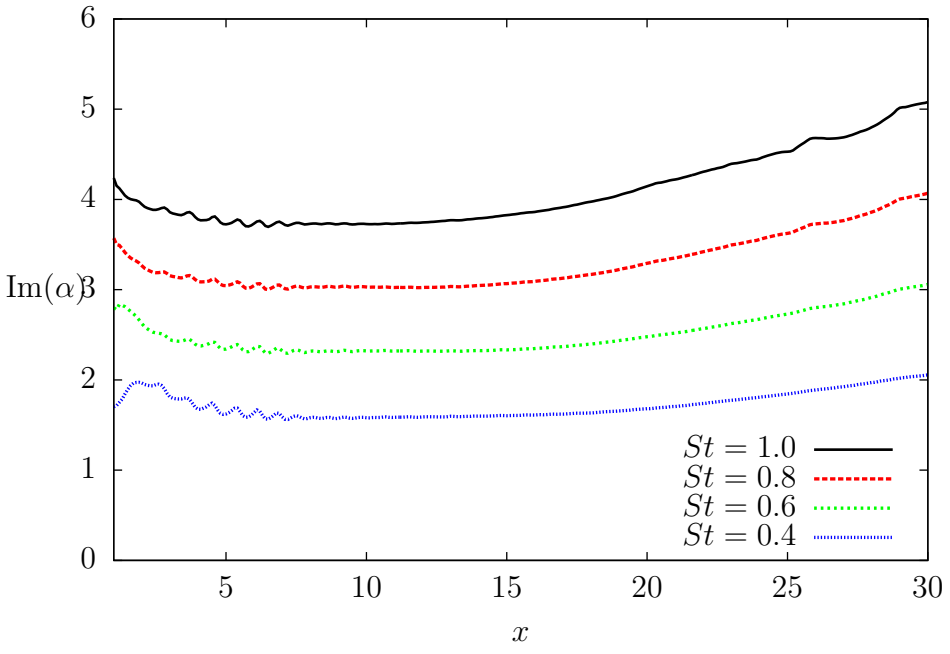


Figure 2.29: Real part of the wavenumber $\alpha(x)$ for different Strouhal values.

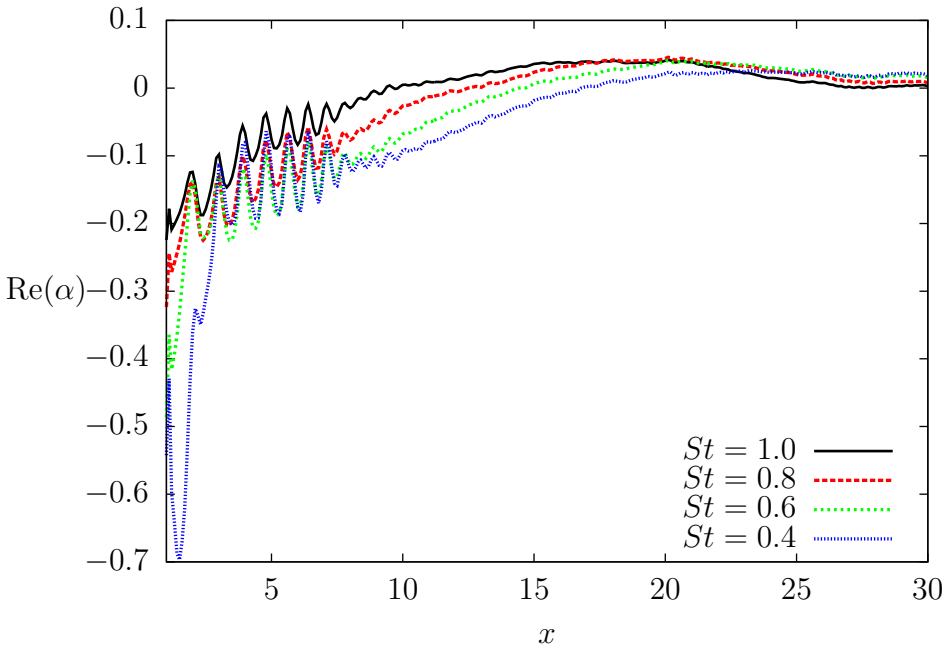


Figure 2.30: Imaginary part of the wavenumber $\alpha(x)$ for different Strouhal values.

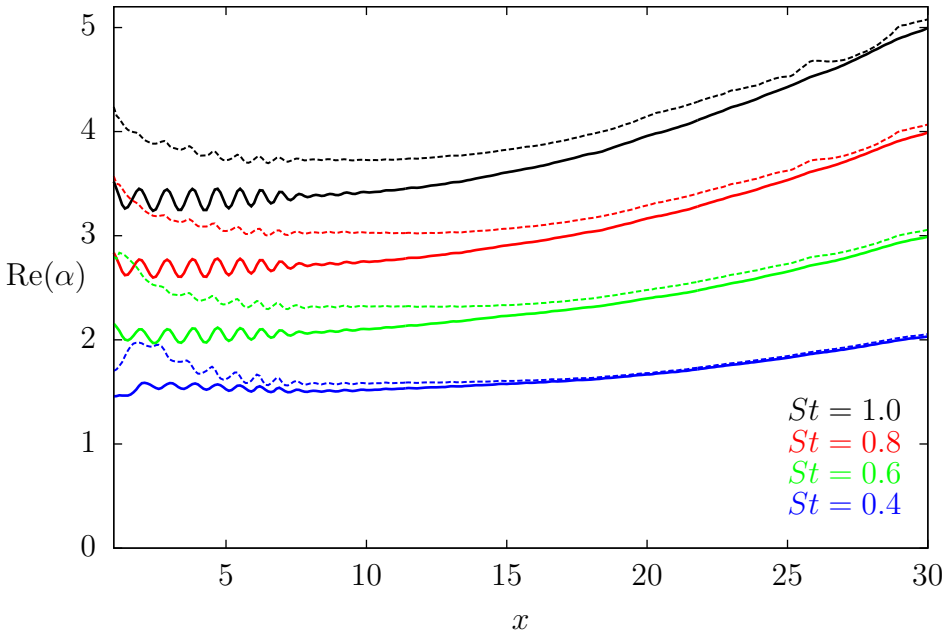


Figure 2.31: Comparison of the real part of $\alpha(x)$ is made for several Strouhal numbers. Computation are obtained by initialising the PSE with the primary unstable mode, $KH_1$, full lines and with the secondary unstable modes, $KH_2$, dot-lines. .

As explained in Léon (2012)[63] whereas the outcome is unambiguous when a single unstable modes is present, the result is confused if the base flow supports multiple instabilities. It almost impossible to separate the two distinct unstable modes $KH_1$ and $KH_2$ computing the PSE without any kind of interaction between them. In particular the modes related to the primary jet, $KH_1$, probably due to his less unstable values, seems to quickly interact with the secondary jet. As observed in Sinha et al. (2016)[111] the instability waves referred to the two modes collapse downstream in the same wave. To elucidate this point, figure 2.31 shows the wavenumber $\alpha_r(x)$ of the outer and inner PSE solutions for different Strouhal number in both cases, $KH_1$ and $KH_2$. The solutions converge into a same values when moving downstream in the streamwise direction.

Qualitatively this mechanism can be observed in figure 2.33 and 2.34. When computing the PSE with respect to the secondary modes, $KH_2$ the pressure perturbation $p'$ stay in the secondary jet ($r/D_p = 1.0$ at the exit of the nozzle) at least, until this distinction can be done ($x = 10 - 11D_p$). The pressure perturbation $p'$ referred to the primary jet start to grow up in the inner shear layer, but then "jump" to the more unstable outer shear layer. This behaviour is exaggerate for $St = 0.4$, see figure 2.34, where the secondary shear layer is much more unstable comparing to the primary one, 2.2.

These evidences demonstrates the coalescence of the outer and inner modes. Also if they start out as distinct instabilities near the nozzle, PSE cannot track them separately. These observations are representative of the range of frequencies studied ($St = 0.4$, 0.6, 0.8, 1.0). The intrinsic interaction between the two modes, $KH_1$ and $KH_2$, put in evidence three observations: (1) the primary and secondary shear layer merge downstream of the nozzle and at least this zone cannot support multiple unstable Kelvin-Helmholtz modes; (2) the more unstable secondary shear layer interact with the unstable modes even if this perturbation is generated in the primary shear layer; (3) it seems that in the interval $[6.5, 8]$ there is a natural exchange of stability. These Observations can be confirmed by a loacal stability analysis.

On figure 2.32 are plotted the most unstable eigen values obtained via the local stability theory from $x = 1$ to $x = 8$. Inside blue circles are emphasized the first KH mode ($KH_1$) at $x = 6$ and $x = 8$, and in red, the second KH modes, $KH_2$, are plotted at the same positions. It is clearly demonstrated that the $KH_1$ becomes less amplified than the $KH_2$ at $x = 8$, contrarily to the case $x = 6$. The $\alpha_i$ axis ends on the figure at $-0.01$ to avoid the numerous modes with neutral amplification. More deep conclusions will be pointed out when computing the sensitivity analysis in Chapter 3.

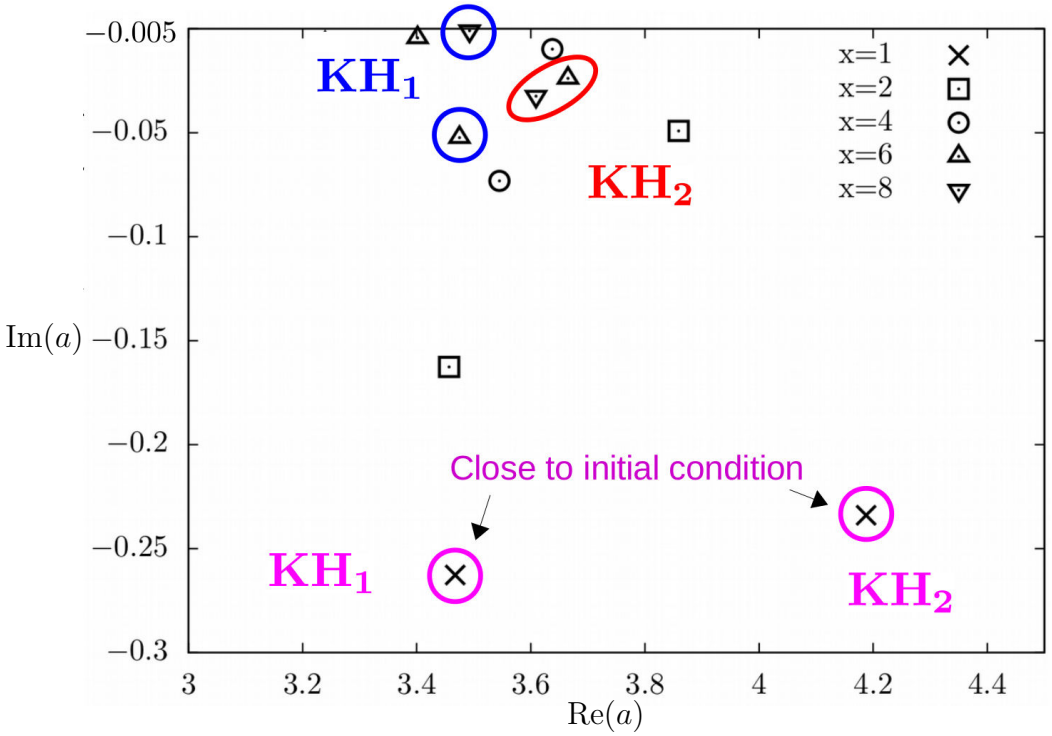


Figure 2.32: LST: part of the spectrum for different $x$. $St = 1$. The vertical axis ends at $-0.01$.

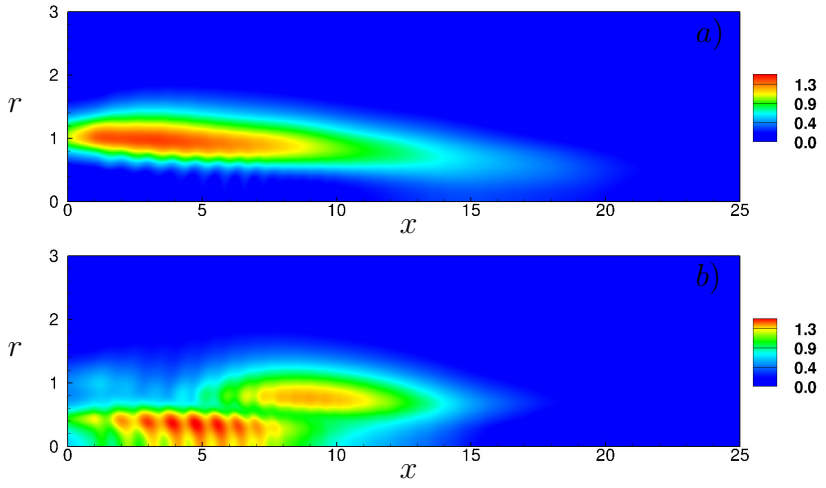


Figure 2.33: Spatial distribution of the absolute value of the pressure disturbance, $|p'|$ for $St = 1.0$. (a) PSE is initialised with the secondary unstable modes, $KH_2$. (b) is initialised with the primary unstable modes..

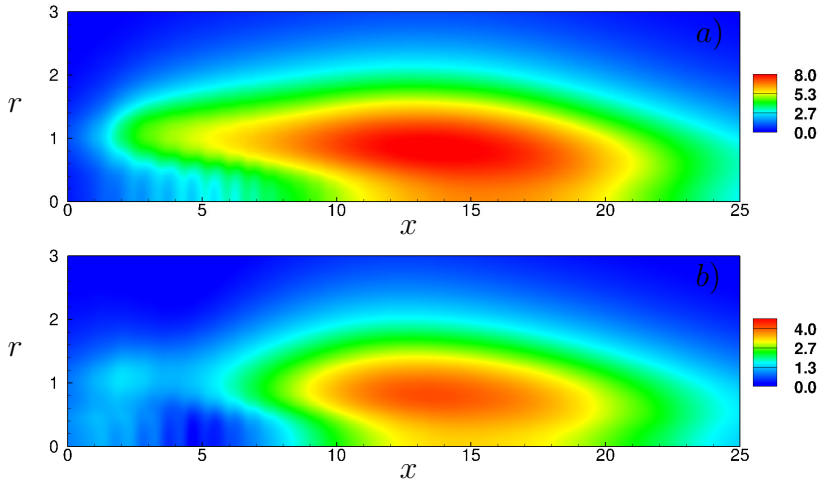


Figure 2.34: Spatial distribution of the absolute value of the pressure disturbance, $|p'|$ for $St = 0.4$. (a) PSE is initialised with the secondary unstable modes, $KH_2$. (b) is initialised with the primary unstable modes.

### 2.2.4 Conclusion

In this chapter we presented the PSE approach. This approach is used in this thesis to analyse the convective instability that grow in the shear layer of the jet. This instability are well known as Kelvin-Helmholtz instability. The code used to investigate this unstable waves has been developed at ONERA by Léon [63]. In this thesis we present four different cases, an analytical subsonic and incompressible flow, a semi-empirical supersonic flow and an under expanded single and dual stream jet obtained by LES computation. We implemented the stabilization of the PSE code, this up-grate aims to the computation of the PSE equations with a smaller discretization in the streamwise direction. Because of the complexity of an under expanded supersonic jet a good discretization in the radial, but as well in the streamwise direction is required. The stabilization procedure, developed by Andersson et al. (1998)[8], has been validated for a supersonic semi-empirical test case. The PSE computation for a specific under expanded dual stream jet configuration has been done. This configuration has an important industrial interest as confirmed by the partnership of Airbus and Alstom at this project. A parametric study of the Strouhal number pointed out as the shock cell play an important role in the growth rate of the instability if compare to the frequency. Finally as observed in previous works, Léon and Brazier[64] and Sinha et al. [111] it is not possible to completely separate the two unstable Kelvin-Helmholtz modes referring to the primary and secondary shear layer.

# Chapter 3

# Sensitivity analysis

Adjoint methods are based on the use of the adjoint operator of a given system of equations. The adjoint equations have a form similar to the direct equations, and so the numerical method required for its implementation is of the same complexity as the method used for the direct algorithm. However, some subtle differences exist which must be considered, and are highlighted in this chapter. The aim of the present work is to derive the adjoint of the Parabolized Stability Equations for a compressible jets in a consistent way, to validate it by performing some test cases as in the previous chapter and to apply sensitivity to the complex case of dual-stream under-expanded jet. At the beginning of this chapter the principles of the adjoint methods are given. After that, the mathematical formulation of the adjoint of the Parabolized Stability Equations is detailed. Then the new code developed is validated and, finally, its numerical implementation is presented. Adjoint methods present a wide range of applications of interest in fluid dynamic problems: sensitivity and receptivity analysis, computation of the optimal perturbation and optimal control, and other optimization problems such as shape and grid optimizations, error minimization and optimal modification of the mean flow. In this thesis the adjoint methods is used to perform sensitivity analysis for compressible jets. Receptivity analysis has not been done in this thesis, but it is closely related to sensitivity analysis and so a brief description is included. The literature search reveals that the adjoint of the PSE for compressible flow have never been applied to investigate external forcing perturbing the system[10, 12]. We decided to perform this study because in our opinion sensitivity analysis (SA) is one of the most successful ways to understand how external disturbances evolve and create unstable waves into a jet.

## 3.1 Deeper knowledge of adjoint approach

This section is inspired by the review of Lucchini and Bottaro (2014)[71]. Adjoint equations can be obtained, basically, in two ways that are intrinsically different:

- the adjoint equations are extracted by the direct equations in the continuous space and then both are discretized to be solved. This method is known as **continuous adjoint**

- the direct equations are discretized and the adjoint method is applied to this new system of equations to obtain the **discretized adjoint**.

The continuous equations are easier to implement because of the similarity with the direct equations and easier to read and to interpret. On the other hand the discretized approach aims the adjoint solution to be non dependent to the discretization. In our works we always approach the first methodology that it is also, traditionally, the choice of IMFT's works.

In this chapter the inner product in the axial direction, radial direction and in the whole computational domain are defined as follows:

$$\langle \boldsymbol{u}, \boldsymbol{v} \rangle_r = \int_0^\infty \boldsymbol{u}^h \boldsymbol{v}\, r dr, \quad \langle \boldsymbol{u}, \boldsymbol{v} \rangle_x = \int_{x_0}^{x_f} \boldsymbol{u}^h \boldsymbol{v}\, dx \quad \text{and} \quad \langle \boldsymbol{u}, \boldsymbol{v} \rangle_\Omega = \int_\Omega \boldsymbol{u}^h \boldsymbol{v}\, d\Omega \tag{3.1}$$

Where $\boldsymbol{u}$ and $\boldsymbol{v}$ stand for generals complex vectors and $d\Omega = rdrdx$.

## 3.2 Pedagogical example of adjoint procedure

We considered the same problem illustrated by Airiau (2004)[4], we show the procedure to evaluate the adjoint equation based on the Lagrange multipliers.

Consider $x$ and $y$ the space variables and $\Omega$ the rectangular domain of our problem, $(x, y) \in \Omega$, $\Omega = [x_0, x_f] \times [0, \infty[$.

We define the **cost functional** as:

$$E = \frac{1}{2}\left(\varepsilon_0 \langle q_0, q_0 \rangle_y + \varepsilon_f \langle q_f, q_f \rangle_y + \varepsilon \langle q, q \rangle_\Omega\right) \tag{3.2}$$

where $\langle q_0, q_0 \rangle_y$, $\langle q_f, q_f \rangle_y$ and $\langle q, q \rangle_\Omega$ are respectively $\int_0^\infty q_0^2 dy$, $\int_0^\infty q_f^2 dy$ and $\int_\Omega q^2 d\Omega$. The cost function is weighted combination of the three terms and we can control it changing the values of $\varepsilon_0$, $\varepsilon_f$ and $\varepsilon$.

The **state equation** is the well known Linear Burger's equation:

$$\frac{\partial q}{\partial x} + U(y)\frac{\partial q}{\partial y} - \frac{\partial^2 q}{\partial y^2} = f(x, y) \tag{3.3}$$

where $U$ and $f$ are known functions. In symbolic form the 3.3 reads:

$$Lq = f \tag{3.4}$$

with:

$$L = \left\{\frac{\partial}{\partial x} + U(y)\frac{\partial}{\partial y} - \frac{\partial^2}{\partial y^2}\right\} \tag{3.5}$$

The initial condition and boundary conditions are respectively:

$$q(x_0, y) = q_0(y), \tag{3.6}$$

$$q\left(x,0\right)=q_w\left(x\right), \tag{3.7}$$

$$\lim_{y\to\infty} q\left(x,y\right)=0 \tag{3.8}$$

Arbitrary we calculate the sensitivity of $E$ with respect to $f$:

$$S_f=\nabla_f E \tag{3.9}$$

Writing the Lagrangian functional, the problem becomes unconstrained:

$$\mathcal{L}=E-\langle q^*, Lq-f\rangle_\Omega \tag{3.10}$$

where $q^*$ is the Lagrangian multiplier.
The gradient $\nabla\mathcal{L}_u$ of the functional with respect to a general variable $u$ is defined as:

$$\mathcal{L}(u+\delta u)-\mathcal{L}(u)=\langle\nabla_u\mathcal{L},\delta u\rangle_\Omega \tag{3.11}$$

All the theory of this approach is concentrated in the next two remarks:

1. because equation 3.4 is always verified $\mathcal{L}=E$.
2. by definition the variation of the functional $\delta\mathcal{L}$ is equal to the sum of any directional derivatives:

$$\delta\mathcal{L}=\langle\nabla_q\mathcal{L},\delta q\rangle_\Omega+\langle\nabla_f\mathcal{L},\delta f\rangle_\Omega+\langle\nabla_{q^*}\mathcal{L},\delta q^*\rangle_\Omega+\langle\nabla_{q_0}\mathcal{L},\delta q_0\rangle_y+\langle\nabla_{q_w}\mathcal{L},\delta q_w\rangle_x$$

.

Imposing to zero all the variations of the functional excepted $\delta\mathcal{L}=\langle\nabla_f\mathcal{L},\delta f\rangle$, considering remark 1 and remark 2 and using integrations by parts rule we find:

$$\begin{gathered} L^*q^*=\varepsilon q \\ q^*\left(x_f,y\right)=\varepsilon_f q_f \\ q^*\left(x,0\right)=0,\quad \lim_{y\to\infty} q^*\left(x,y\right)=0 \end{gathered}$$

and the sensitivity $S_f$ simply is:

$$S_f=q^*$$

To evaluate $S_f$ we only need to solve ones the adjoint equations.

## 3.3 Adjoint PSE theory

This section has the purpose of illustrating a general adjoint based theory for the PSE approach presented in the previous chapter that can be a powerful tool not only for the study of external forcing, but for any other parameter involved on the PSE computation. All the results presented here will refer to axisymmetric perturbations, $m=0$ in a jet.

### 3.3.1 The cost functional

By definition [101] sensitivity is equivalent to a gradient of any functional for instance described by a quadratic integral. This functional called $E$ could be a physical energy associated to the perturbed velocity, temperature and pressure. Mathematically it can be written as a quadratic function of the full disturbance vector. In addition the energy can be defined globally, in the full computational domain or at a given $x$ streamwise location.

So let define the local energy as :

$$E_x(x) = \int_0^\infty \boldsymbol{q}'^h M \boldsymbol{q}' m_r dr.$$

$m_r$ is a metric and $M$ is a diagonal positive matrix which weights the component of the disturbance vector and it allows some various energy definitions.

The global energy is defined from the local energy as:

$$E = \frac{1}{2}\int_{x_0}^{x_f} E_x(x)dx$$

Inspired by the previous work of Walther et al. (2001)[131] the objective function is set as a quadratic function associated to the full disturbance vector. This function can be defined locally in a given streamwise location:

$$E_x(x) = \int_0^\infty \hat{\boldsymbol{q}}^h \hat{\boldsymbol{q}}\, r\, dr \qquad \text{where,} \qquad \hat{\boldsymbol{q}} = \chi \boldsymbol{q}$$

with

$$\chi(x) = \exp\left[i\int_{x_0}^{x} \alpha(\xi)d\xi\right],$$

The new unknown term $\hat{\boldsymbol{q}}(x,r)$ can be read as the spatial distribution of the disturbance $\boldsymbol{q}'(x,r,t)$. In addition it can be defined globally, in the full computational domain:

$$E = \frac{1}{2}\int_{x_0}^{x_f} E_x(x)dx$$

The Adjoint PSE theory is developed for the following general non dimensional cost functional:

$$E = \ell \int_{x_0}^{x_f} E_x\, dx + \ell_f E_f + \ell_0 E_0 \tag{3.12}$$

Where $E_f = E_x(x_f)$ and $E_0 = E_x(x_0)$.

### 3.3.2 State equation (PSE)

Any perturbation $\boldsymbol{q}'$ is assumed to have a wave-like exponential term $\chi(x)\exp(i(m\theta - \omega t))$ and an amplitude function $\mathbf{q}(x,r)$ that varies slowly with $x$ as:

$$\boldsymbol{q}' = \boldsymbol{q}(x,r)\chi(x)\mathrm{e}^{i\ (m\theta - \omega t)}, \tag{3.13}$$

The idea is to explore flow response to external harmonic forcing $\boldsymbol{f}'$ directly acting in the Linearized Euler Equations (LEE):

$$\frac{\partial \rho'}{\partial t} + \bar{\rho}(\boldsymbol{\nabla}\cdot\boldsymbol{u}') + \rho'(\boldsymbol{\nabla}\cdot\bar{\boldsymbol{u}}) + (\bar{\boldsymbol{u}}\cdot\boldsymbol{\nabla}\rho') + (\boldsymbol{u}'\cdot\boldsymbol{\nabla}\bar{\rho}) = f_1' \tag{3.14}$$

$$\bar{\rho}\left(\frac{\partial \boldsymbol{u}'}{\partial t} + (\underline{\boldsymbol{\nabla}\boldsymbol{u}'}\cdot\bar{\boldsymbol{u}}) + (\underline{\boldsymbol{\nabla}\bar{\boldsymbol{u}}}\cdot\boldsymbol{u}')\right) + \boldsymbol{\nabla}p' = \boldsymbol{f_m'} \tag{3.15}$$

$$\frac{\partial s'}{\partial t} + (\boldsymbol{\nabla}s'\cdot\bar{\boldsymbol{u}}) + (\boldsymbol{\nabla}\bar{s}\cdot\boldsymbol{u}') = f_5' \tag{3.16}$$

where the source term $\boldsymbol{f'} = [f_1', \boldsymbol{f_m'}, f_5']$ is applied in the LEE, while $\boldsymbol{f_m'}$ is the momentum forcing with components: $\boldsymbol{f_m'} = [f_2', f_3', f_4']$

Following the PSE approach modal decomposition of the perturbation $\boldsymbol{q}'$ and of the source term $\boldsymbol{f}'$ is applied.

$$\boldsymbol{q}' = \boldsymbol{q}\,\chi\,\mathrm{e}^{i(m\theta - \omega t)} \qquad \text{and} \qquad \boldsymbol{f}' = \boldsymbol{f}\,\mathrm{e}^{i(m\theta - \omega t)} \tag{3.17}$$

Substituting equation 3.17 into equation 3.14-3.16 and using PSE assumption we get the forced Parabolized Stability Equations for jet. In symbolic form reads:

$$\chi L_{PSE}\boldsymbol{q} = \boldsymbol{f} \tag{3.18}$$

$L_{PSE}$ is the same operator shown in equation 2.26.

Normalization equation and the boundary conditions are the same of the unforced PSE equations (Chapter 2).

As the problem is "quasi" parabolic (see previous chapter) we initialize the problem with a known initial condition (i.e. from the local stability eigenvalue problem).

$$\boldsymbol{q}(x_0, r) = \boldsymbol{q}_0 \qquad \text{and} \qquad \alpha(x_0) = \alpha_0. \tag{3.19}$$

### 3.3.3 Sensitivity analysis

#### a- Definitions

The sensitivity $S_{v_k}$ is defined as the gradient of $E$ with respect to any component of a vector $\boldsymbol{v}$, $v_k$ or any scalar variable $b$, $S_b$. Formally it can be written as:

$$S_{v_k} = \nabla_{v_k} E(v_k = v_{k0}) = \left[\frac{\partial E}{\partial v_k}\right]_{v_k = v_{k0}}$$
$$\text{or} \tag{3.20}$$
$$S_b = \nabla_b E(b = b_0) = \left[\frac{\partial E}{\partial b}\right]_b$$

As shown in the previous example, in section 3.2, the technique adopted here to solve the computational gradient is based on the Lagrange multipliers method. The unconstrained Lagrangian functional, $\mathcal{L}$, which operates on the real range, take directly into account of the PSE equations, the normalization equation, the boundary conditions and the variables of the sensitivity. Here the theory is developed for external sources, $\boldsymbol{f}(x,r)$, for variations of the frequency $\omega$ and for variations of the initial condition $\boldsymbol{q}_0(r)$. It is easy to demonstrate that an extension of any other variables is possible with few modifications of the adjoint equations. Under the hypothesis of small variations, all arguments of this new functional are assumed independent of each others. We have

$$\mathcal{L} = E - \langle \hat{\boldsymbol{q}}^*, \chi L_{PSE}\boldsymbol{q} - \boldsymbol{f}\rangle_\Omega - \int_{x_0}^{x_f} n^{*h}\langle \boldsymbol{q}, \frac{\partial \boldsymbol{q}}{\partial x}\rangle_r \, dx - \langle \hat{\boldsymbol{p}}_0^*, \boldsymbol{q}(x_0,r) - \boldsymbol{q}_0\rangle_r + c.c. \quad (3.21)$$

where $\hat{\boldsymbol{q}}^*$, $n^*$ and $\hat{\boldsymbol{p}}_0^*$ are the complex Lagrangian multipliers.
The variation of the functional schematically reads:

$$\delta\mathcal{L} = \frac{\partial\mathcal{L}}{\partial\hat{\boldsymbol{q}}}\delta\hat{\boldsymbol{q}} + \frac{\partial\mathcal{L}}{\partial\alpha}\delta\alpha + \frac{\partial\mathcal{L}}{\partial\hat{\boldsymbol{q}}^*}\delta\hat{\boldsymbol{q}}^* + \frac{\partial\mathcal{L}}{\partial n^*}\delta n^* + \frac{\partial\mathcal{L}}{\partial\hat{\boldsymbol{q}}_0}\delta\hat{\boldsymbol{q}}_0 + \frac{\partial\mathcal{L}}{\partial\hat{\boldsymbol{p}}_0^*}\delta\hat{\boldsymbol{p}}_0^* + \frac{\partial\mathcal{L}}{\partial\boldsymbol{f}}\delta\boldsymbol{f} + \frac{\partial\mathcal{L}}{\partial\omega}\delta\omega + c.c. \quad (3.22)$$

Where the two last terms refers to the sensitivity with respect to forcing, $\boldsymbol{f}(x,r)$ and to the frequency, $\omega$. Because of the identity in equation 3.21, the Lagrangian $\mathcal{L}$ is the cost function $E$ by definition. Imposing all the different directional derivatives must vanish with the exception of the gradient we are looking for, i.e. $\frac{\partial\mathcal{L}}{\partial f_k}\delta f_k$:

$$\delta\mathcal{L} = \frac{\partial\mathcal{L}}{\partial f_k}\delta f_k = \frac{\partial E}{\partial f_k}\delta f_k \quad (3.23)$$

In order to make the equations more readable is more convenient to write the Lagrangian multipliers $\hat{\boldsymbol{q}}^*$ and $\hat{\boldsymbol{p}}_0^*$ in a way similar to the direct variables by the introduction of a wave-like part[3]:

$$\hat{\boldsymbol{q}}^* = \chi^*\boldsymbol{q}^* \quad \text{and} \quad \hat{\boldsymbol{p}}_0^* = \chi^*\boldsymbol{p}_0^* \quad (3.24)$$

where $\chi^*$ is such that $\chi\chi^{*h} = \chi(x_f) = \chi_f$. After integrations by parts and several mathematical steps detailed in the appendix we obtain the adjoint equation with the related closing equation and the sensitivity.

### a- Gradients resolution

1. Imposing equal to zero the gradient with respect to the state vector lead to the so-called adjoint PSE equations where the adjoint state $\boldsymbol{q}$ is solution of:

$$\frac{\partial\mathcal{L}}{\partial\boldsymbol{q}} = \boldsymbol{0}: \qquad \chi_f^h\left[\left(A^h + B^h\right)\boldsymbol{q}^* - \frac{\partial A_1^h\boldsymbol{q}*}{\partial x} - \frac{1}{r}\frac{\partial A_0^h\boldsymbol{q}^*}{\partial r}\right] = \frac{\partial\left(n^*\boldsymbol{q}\right)}{\partial x} - n^{*h}\frac{\partial\boldsymbol{q}}{\partial x} + \ell\chi\chi^h\boldsymbol{q} \quad (3.25)$$

with boundary conditions:

$$\delta \boldsymbol{q}(x_0): \qquad \ell_0 \boldsymbol{q}(x_0) + C_0^h \boldsymbol{q}^*(x_0) + n^*(x_0)\boldsymbol{q}(x_0) - \chi_f \boldsymbol{p}_0^* = \boldsymbol{0} \tag{3.26}$$

$$\delta \boldsymbol{q}(x_f): \qquad \ell_f \chi_f \chi_f^h \boldsymbol{q}(x_f) - C_f^h \boldsymbol{q}^*(x_f) - n^*(x_f)\boldsymbol{q}(x_f) = \boldsymbol{0} \tag{3.27}$$

2. Imposing equal to zero the gradient with respect to the streamwise wavenumber, $\alpha(x)$, leads to the closing equation of the adjoint PSE where $n$ is solution of:

$$\frac{\partial \mathcal{L}}{\partial \alpha} = 0: \qquad \ell E_x + \chi_f \frac{\partial \left\langle \boldsymbol{q}^*, A_0 \boldsymbol{q} \right\rangle_r}{\partial x} = 0 \tag{3.28}$$

with boundary conditions:

$$\int_{x_0}^{x_f} \delta\alpha \, d\xi: \qquad \ell_f E_f - \chi_f \left\langle \boldsymbol{q}_f^*, A_{0f} \boldsymbol{q}_f \right\rangle_r = 0 \tag{3.29}$$

3. The gradient with respect to the external forcing, $\boldsymbol{f}(x,r)$, to the frequency, $\omega$, and to the initial condition, $\boldsymbol{q}_0(x)$, are the sensitivity themselves and respectively reads:

$$\frac{\partial \mathcal{L}}{\partial f_k} \delta f_k = \langle \hat{q}_k^*, \delta f_k \rangle_\Omega + c.c. \tag{3.30}$$

$$\frac{\partial \mathcal{L}}{\partial \omega} \delta\omega = i\chi_f \left\langle \boldsymbol{q}^*, A_2 \boldsymbol{q} \delta\omega \right\rangle_\Omega + c.c. \tag{3.31}$$

$$\frac{\partial \mathcal{L}}{\partial \hat{q}_{0k}} \delta \hat{q}_{0k} = \langle \hat{p}_{0k}^*, \delta \hat{q}_{0k} \rangle_r + c.c. \tag{3.32}$$

**b- The discretization numerical procedure**

A sixth order compact difference scheme [62] is used in the radial direction. The streamwise derivative, $\left.\frac{\partial \boldsymbol{q}^*}{\partial x}\right|_j$, is approximated by the backward finite-difference form $(\boldsymbol{q}_{j+1}^* - \boldsymbol{q}_j^*)/\Delta x$ with integration from $x_f$ to $x_0$. The equation 3.25 and 3.28 are solved with a Newton-Raphson algorithm and convergence is fast, less than 10 iterations with $n^*$ for each streamwise location $x$. The iteration is repeated until a relative error smaller than $10^{-8}$.

## 3.4 Validation of the adjoint PSE theory

### 3.4.1 Sensitivity coefficients for cases I 2.2.1 and II 2.2.2

**a- Case I 2.2.1**

Figure 3.1 shows The variations of the total energy $E$ with respect to forcing acting in the continuity, momentum and energy equation for the incompressible case I 2.2.1.

The normalized sensitivity coefficients that the shape of the sensitivity functions and the location of their maximum are strongly related to the radial and the streamwise variation of the base flow. In particular the maximum of sensitivity is located along the border of the potential cone. In addition the sensitivity increases when the streamwise coordinate decreases. That makes sense since it is natural to act as soon as possible on the noise generation mechanism if reduce noise emission is targeted. Another important point is that sensitivity to axial momentum forcing is much higher than to radial momentum forcing.

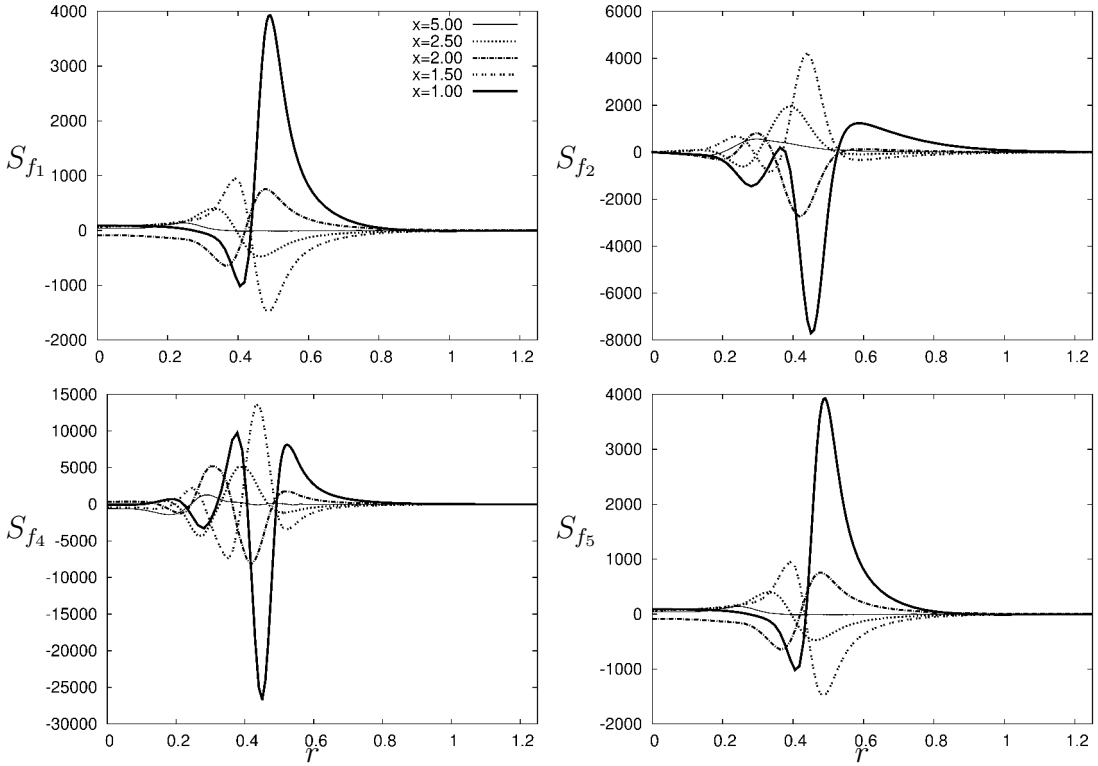


Figure 3.1: Sensitivity of the analytical incompressible jet. From the top to the bottom we have respectively, the gradient of $E$ with respect to the forcing acting in the continuity, $r$-momentum, $x$-momentum and energy equation at different fixed position in the streamwise direction ($x = 5.0$, 2.5, 2.0, 1.5, 1.0)

**b- Case II 2.2.2**

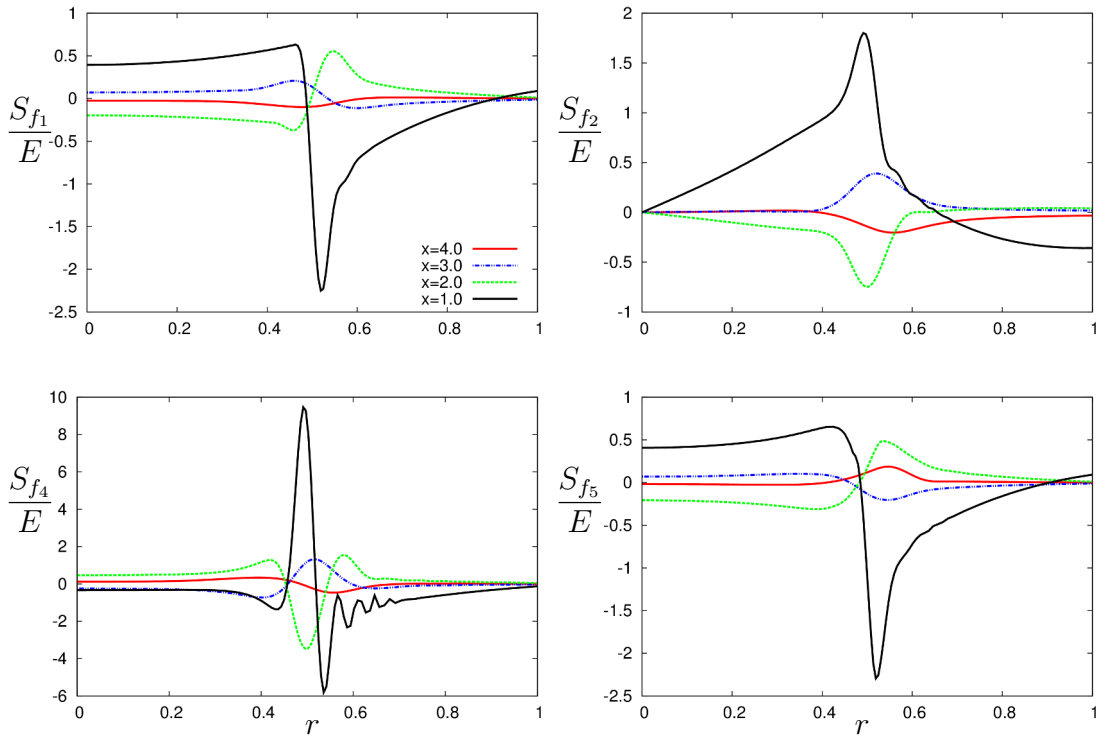


Figure 3.2: Sensitivity of the semi-analytical supersonic jet. From top to the bottom we have respectively, the gradient of $E$ with respect to the forcing acting in the continuity, $r$-momentum, $x$-momentum and energy equation at different fixed position in the streamwise direction ($x = 4.0,\ 2.0,\ 1.0,\ 0.5$). The Strouhal number is $St = 0.4$

The normalized sensitivity coefficients with respect to conservation equation forcing are shown in Fig. 3.2, for Strouhal number, $St = 0.4$. They are strongly dependent on the spatial coordinates $x$ and $r$. As expected, the sensitivity coefficients grow at the positions in the streamwise direction closer to the exit nozzle at $x_0$. The maximum is reached close to the potential core in the shear layer of the jet in the range $x \in [0.45, 0.55]$ approximately. These conclusions are very similar to the ones found in the laminar subsonic jet, figure 3.1.

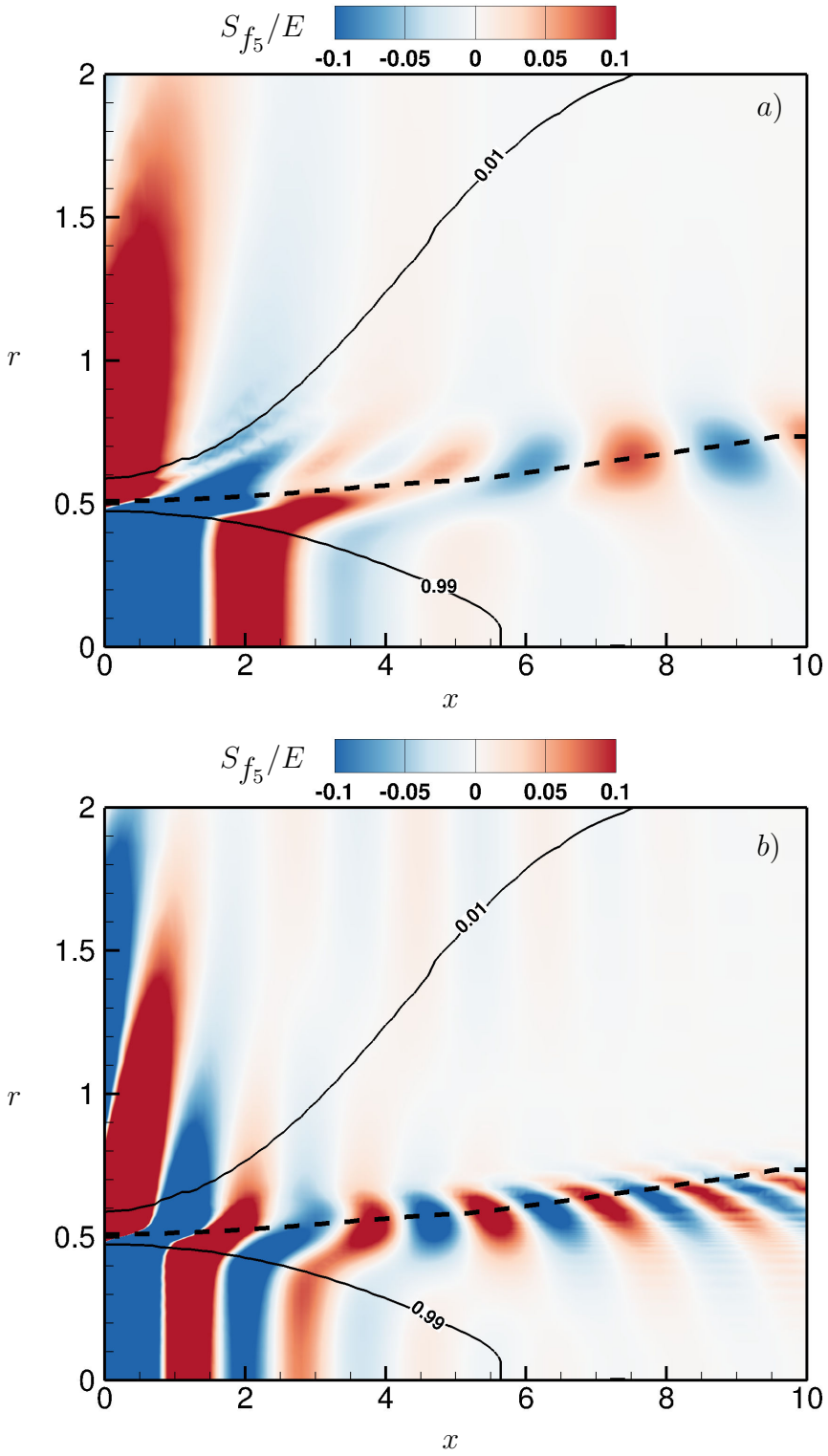


Figure 3.3: The normalized sensitivity with respect to the forcing acting in the energy equation, $S_{f_5}/E$, as a function of the spatial coordinates. The results refer to the supersonic semi-empirical baseflow 2.2.2 with a) $St = 0.2$ and b) $St = 0.4$. Below the isoline $\bar{u}_x = 0.99 \cdot \bar{u}_x(0, r)$ we can assume to be in the potential core otherwise the shear layer is delimited by the isoline $\bar{u}_x = 0.99 \cdot \bar{u}_x(0, r)$ and by the isoline $\bar{u}_x = 0.01 \cdot \bar{u}_x(0, r)$. The dashed line is the inflection point of the baseflow

In figure 3.3 can be observed the spatial distribution of the normalized sensitivity with respect to forcing acting in the energy equation (for the other sensitivities conclusions are the same). Two different Strouhal number are taking into account: a) $St = 0.2$ and b) $St = 0.4$. The figure clearly shows the crucial role of the inflection point ($\frac{\partial^2 \bar{u}_x}{\partial r^2}$=0) in the evolution of the sensitivity. Moreover The maximum of the sensitivity $\max(|S_f/E|)$ is located along this line.

These results are well correlated with the location of the sound generation mechanism as seen in previous works [123, 64].

All these conclusions should be taken into account during the development of some noise reduction strategies. However it is also important to observe that the maximum of sensitivity, for each fixed position in $x$, is located near to a region where sensitivity is almost zero. Therefore the location of any control system must be very accurate to get some good efficiency.

### 3.4.2 Validation procedure

The APSE computations have been validated for cases 2.2.1 and 2.2.2 by following the steps outlined below:

- PSE code have been modified in order to solve:

$$\chi L_{PSE} \boldsymbol{q} = \boldsymbol{f}_k \tag{3.33}$$

  where $\boldsymbol{f}_k$ is the vector with $f_k$ in the $k$-th components and zero otherwise.

- The variation of the quadratic function $\delta E$ is computed as a difference between equation 3.33 and equation 2.26, after two PSE runs:

$$\delta E = E(\delta f_k) - E(0) \tag{3.34}$$

  The small forcing $\delta f_k$ is chosen as:

$$\begin{aligned} \delta f_k &= \frac{\varepsilon}{K} F(x - \tilde{x}, r - \tilde{r}), \qquad \text{with} \\ F(x - \tilde{x}, r - \tilde{r}) &= \exp(-\sigma_x (x - \tilde{x})^2 - \sigma_r (r - \tilde{r})^2) \end{aligned} \tag{3.35}$$

  where $(\tilde{x}, \tilde{r})$ is the central location of the forcing and $K$ is a constant which normalizes $\delta f_k$ such that $\int_\Omega \delta f_k d\Omega = \varepsilon$. This Gaussian function, equation 3.35 is set in the $k$-th line of the equation 2.26 and it acts in a restricted region of the domain (fig. 3.4). Several tests have been done and the range of the different coefficients to define $f_k$ are given in Tab. 3.1.

- The variation of the quadratic function $\delta E$ is computed following APSE theory:

$$\delta E = \int_\Omega \frac{\bar{\chi}(x_f)}{\bar{\chi}(x)} q_k^*(x, r) \delta f_k(x, r)\, d\Omega + c.c. = \int_\Omega \hat{q}_k^*(x, r) \delta f_k(x, r)\, d\Omega + c.c. \tag{3.36}$$

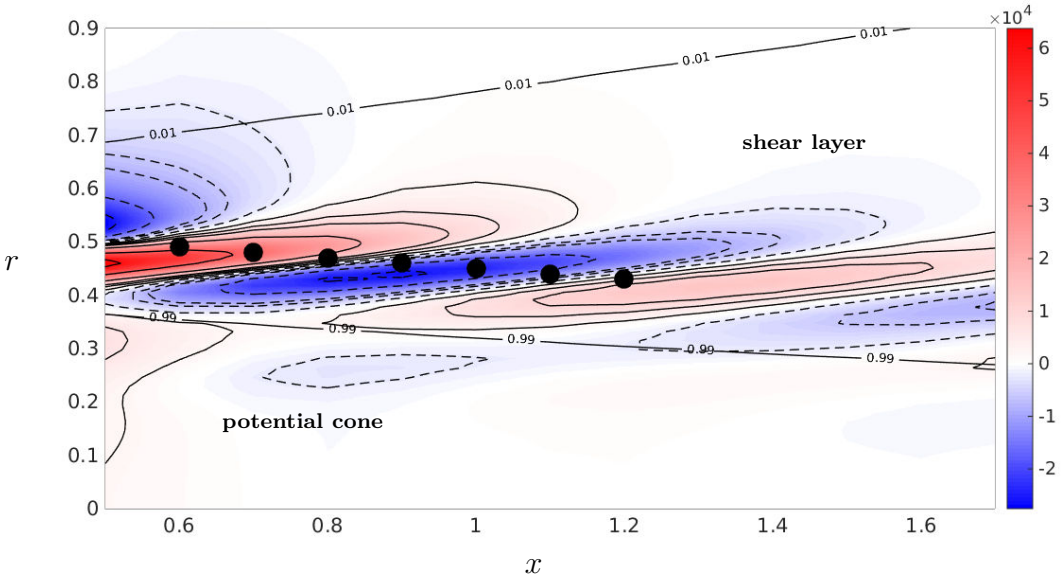


Figure 3.4: Spatial distribution of the gradient of $E$ with respect to a forcing acting in the $x$-momentum, $S_{f_4}$. Below the isolines $\bar{u}_x = 0.99 \cdot \bar{u}_x(0, r)$ and $\bar{u}_x = 0.01 \cdot \bar{u}_x(0, r)$ delimited the potential core and the shear layer regions of the jet. The isolines full line and dashed line indicate respectively positive and negative values of the sensitivity. With • are plotted the $(\tilde{x}, \tilde{r})$ used to validate the A-PSE.

Forcing smaller and more localized in the position nearest from the exit of the nozzle is required in order to avoid modifications of the initial condition $\boldsymbol{q}(0, r)$. The locations of the forcing have been chosen, for both cases, just out of the potential core where the sensitivity is high, see figure 3.4 and, because the arbitrary of the locations tested, they are simply placed along a straight line.

The state perturbation $\boldsymbol{q}(x)$ and the complex wave number $\alpha$ are required and have to be saved when running the PSE problem in the first step .

Results of equation 3.36 shown a very good agreement compared to the direct approach equation 3.34 for the subsonic and supersonic configuration, as displayed in Fig. 3.5*a* and 3.5*b*. The results are obtained by forcing continuity and $x$-momentum equations, similar results have been found forcing the energy and $r$-momentum equations.

| $\tilde{x}$ | $\tilde{r}$ | $\sigma_x$ | $\sigma_r$ | $\varepsilon$ |
|---|---|---|---|---|
| 0.6 | 0.49 | 50 | 50 | $10^{-2}$ |
| 0.7 | 0.48 | 30 | 30 | $10^{-2}$ |
| 0.8 | 0.47 | 30 | 30 | $10^{-2}$ |
| 0.9 | 0.46 | 30 | 30 | $10^{-2}$ |
| 1.0 | 0.45 | 30 | 30 | $10^{-2}$ |
| 1.1 | 0.44 | 30 | 30 | $10^{-2}$ |
| 1.2 | 0.43 | 30 | 30 | $10^{-2}$ |

Table 3.1: Values of the parameters used for the validation at different spatial position

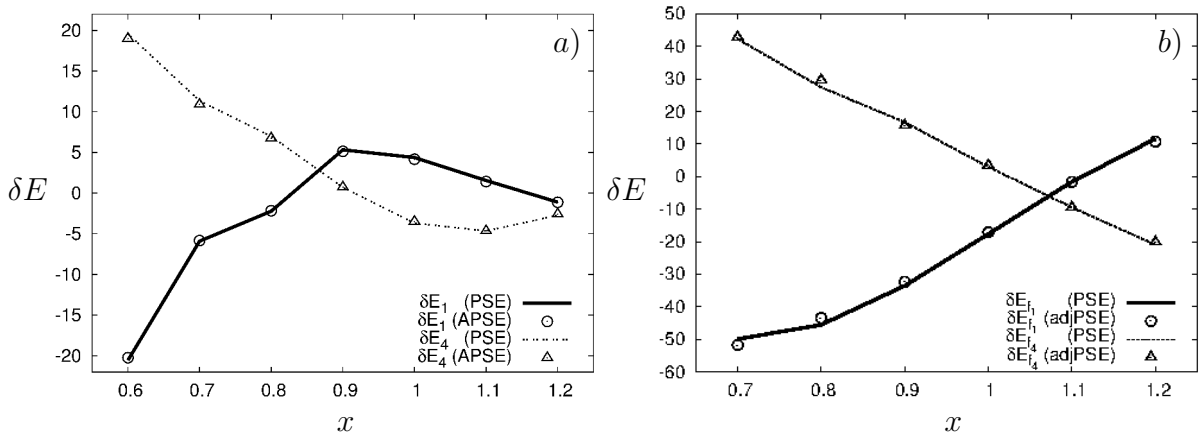


Figure 3.5: Comparison between results from equation 3.34 (lines) and equation 3.36 (symbols) is made for semi-empirical flows ($a$ and $b$ refer respectively to the subsonic and supersonic case.).

## 3.5 Supersonic under-expanded single-stream jet

Figure 3.6 provides the nondimensional sensitivity functions by forcing successively to every conservation equation and is expressed as a function of the adjoint state. It is equivalent to a local (Dirac) forcing. The maximum amplitude are weaker compared to the previous supersonic test case. The location of this maximum is strongly dependent on the streamwise coordinates and the highest sensitivity is closed to the nozzle exit.

The density and energy forcing are quite equivalent, similarly to the other subsonic and supersonic cases. For all the four different forcing the sensitivity is localized inside the shear layer and quickly fall down along the streamwise direction. This results suggest that a flow control mechanism should be applied close to the exit nozzle, definitely before the end of the potential core, and in the shear layer region in order to obtain the highest response of the flow.

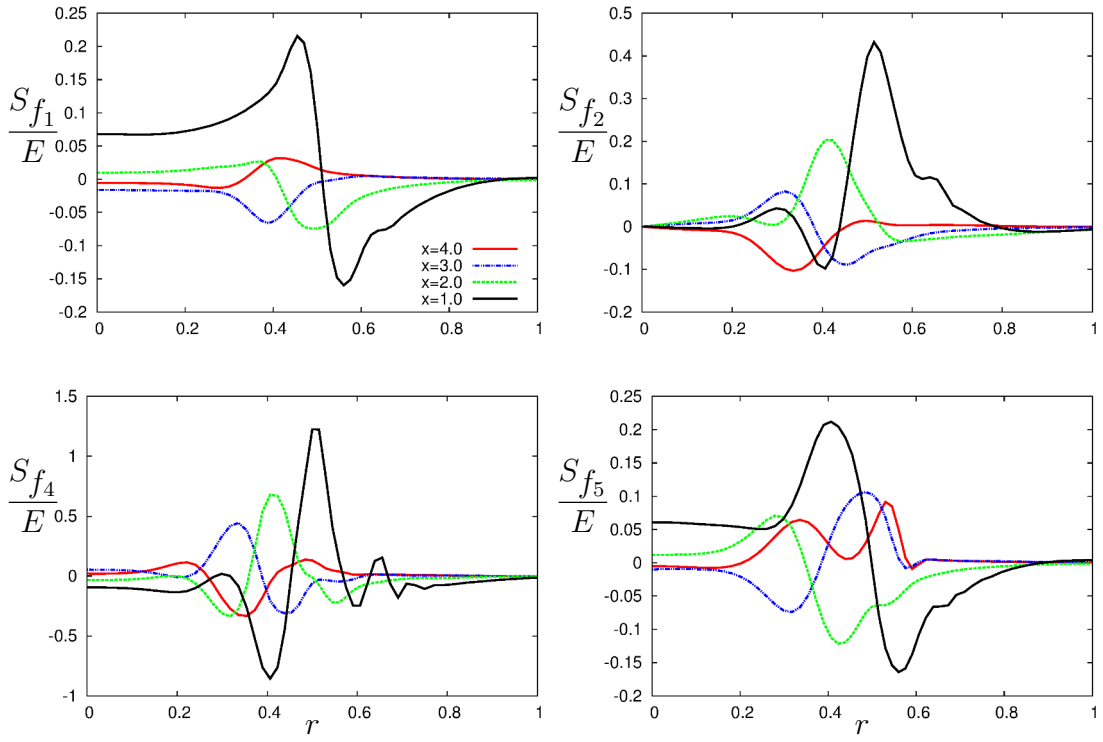


Figure 3.6: From top the bottom we have respectively, the sensitivity $S_f$ computed for the under-expanded supersonic single jet with respect to the forcing acting in the continuity, $r$-momentum, $x$-momentum and energy equation at different fixed position in the stream-wise direction ($x = 4.0$, 2.0, 1.0, 0.5)

### 3.5.1 Supersonic under-expanded dual-stream jet

Results for sensitivity analysis of the dual-stream jet configuration are shown in figures 3.7 and 3.8. The sensitivity is solved for the both unstable modes, $KH_1$ and $KH_2$ (see fig. 2.27) and for the Strouhal number $St = 1.0$. For both cases the sensitivity is spread along the two shear layers and goes to zero for greater values of $r$. The first important result is that the sensitivity is greater in the shear layer related to the unstable modes which initializes the PSE, but the secondary flow has the highest value for any forcing acting in the system. This result emphasizes the role of the secondary jet in this configuration. In figure 3.7 two distinct peaks are located into the primary and secondary shear layer, around $r = 0.5$ and $r \simeq 1.0$, respectively. The same mechanism, but much less prominent, is observed in figure 3.8. These remarks are an additional evidence of the difficulty to clearly separate the two unstable modes, as observed in the previous chapter for the PSE computation. The primary unstable modes $KH1$ is more susceptible to be influenced to the secondary shear layer. This mechanism is probably due to the more unstable nature of the external shear layer. In this configuration, as observed for the single stream jet, the density and energy sensitivity seems to exhibit a similar response along $r$. The total quantity $E$ is affected "qualitatively" in the same way for controls acting in the continuity

or in the energy equations for all jet configurations studied in this thesis; this result is true at least for axisymmetric instabilities. In both figures we still have a strong dependency in the $r$-direction and the local peak of these sensitivities are located at the primary and secondary shear layer radius. The maximum of amplitude are higher compared to the single jet case, suggesting a stronger response to the flow to external forcing.

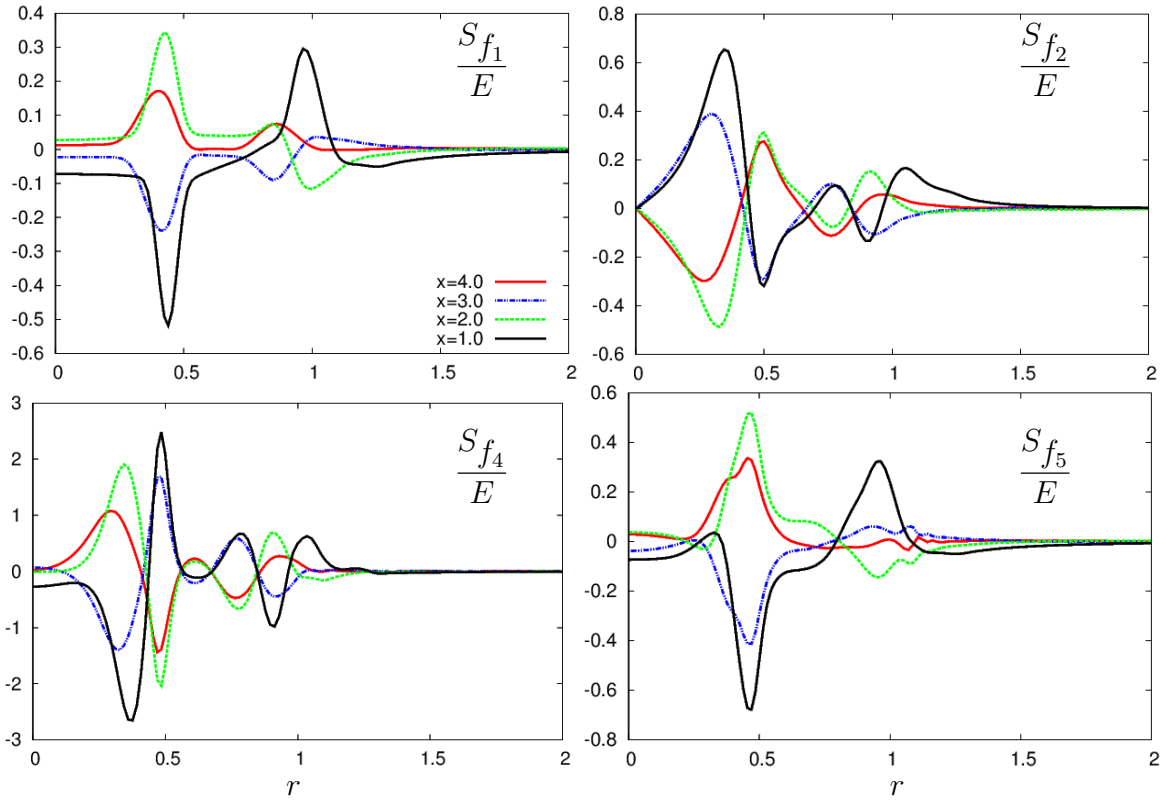


Figure 3.7: The results refer to the unstable mode $KH_1$. From top the bottom we have respectively, the sensitivity $S_f$ computed for the under-expanded supersonic dual-stream jet with respect to the forcing acting in the continuity, $r$-momentum, $x$-momentum and energy equation at different fixed position in the stream-wise direction ($x = 4.0,\ 2.0,\ 1.0,\ 0.5$)

To conclude, instabilities growing in the secondary jet, $KH_2$, are more unstable, less affected to the instability located in the primary shear-layer and with higher values of sensitivities. Focusing to these external disturbances we computed the adjoint PSE for Strouhal number $St = 1.0$ and $St = 0.6$. For both cases the maximum of the sensitivity is reached in the secondary shear layer, denoting a high response of this region to external forcing. The region where the sensitivity is high is not affected from the value of the Strouhal number, see figures 3.9-a and 3.9-b. On the other hand sensitivity decay faster for the $St = 0.6$. After few diameters, $D_p$, in the axial direction the flow is not more sensible to external forcing, see figure 3.9-a. When $St = 1.0$ a not negligible sensitivity is found also for high values of the streamwise position ( fig. 3.9-b), allowing the control to act as well in regions of the flow farther to the exit of the nozzle. This result should be taken into account if the aim of the actuator is to reduce a given frequency of the

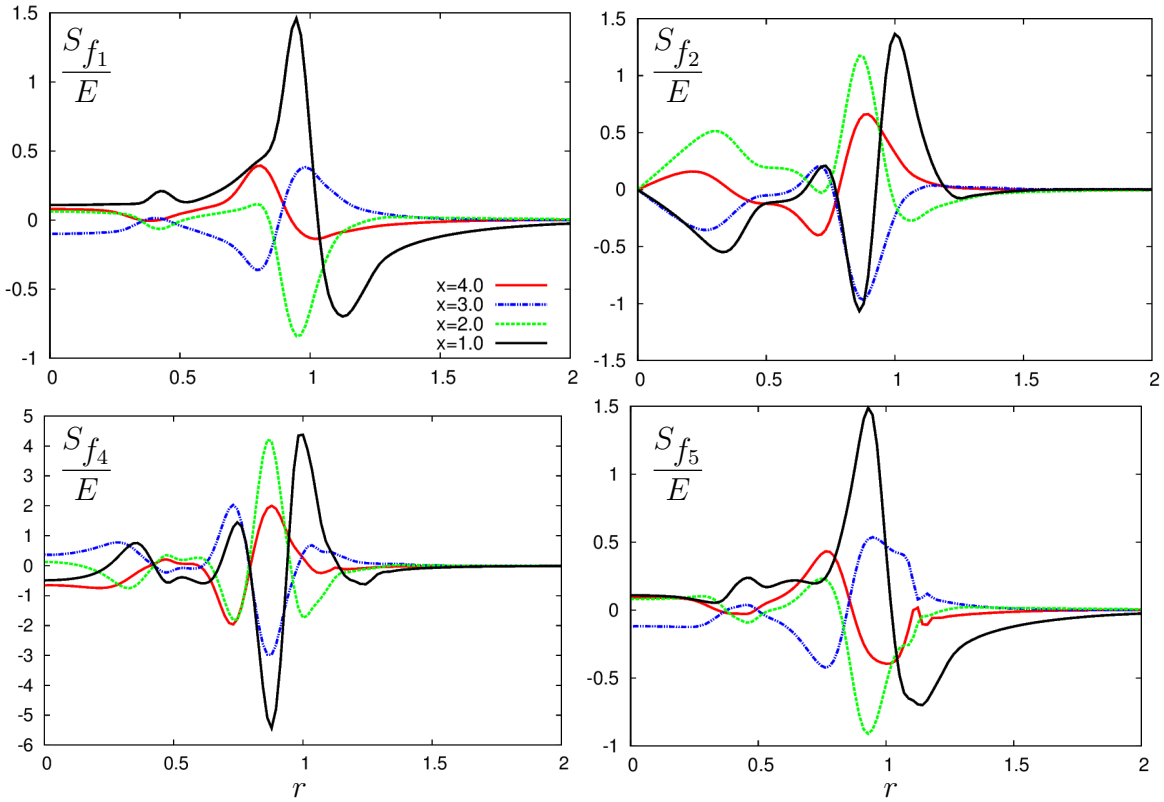


Figure 3.8: The results refer to the unstable mode $KH_2$. From top the bottom we have respectively, the sensitivity $S_f$ computed for the under-expanded supersonic dual-stream jet with respect to the forcing acting in the continuity, $r$-momentum, $x$-momentum and energy equation at different fixed position in the stream-wise direction ($x = 4.0,\ 2.0,\ 1.0,\ 0.5$)

spectral noise. Concluding all these remarks suggest that to implement a new noise control strategy a very careful analysis of the interaction flow/actuator.

### 3.5.2 Conclusion

The sensitivity analysis based on adjoint PSE of subsonic and supersonic single-stream jet flow has been validated. The validated approach has been used for a jet configuration of industrial interest. The sensitivity with respect to under-expanded supersonic single and dual-stream jets has been considered. First configuration outlines a localized region where the response of the flow to external forcing is higher. This region has been identify close to the exit nozzle into the shear-layer in the external boundary of the potential core of the jet. The second configuration present two unstable Kelvin-Helmholtz modes one for each shear-layer. The PSE and Adjoint-PSE computations show the central role of the secondary shear-layer, where the flow is more unstable and the sensitivity is higher. The local peaks of the sensitivity are located at the primary and secondary shear-layer radius highlighting the results of the single- stream jet case. The location of the highest sensitivity seems to be independent of the Strouhal number. However, to implement a new noise control strategy, for both cases, the strong dependence of the sensitivity to

the spatial coordinates of the system suggest a very careful analysis of the interaction flow/actuator. This results have been obtained for both stability and sensitivity analysis, thanks to accurate LES computations from CERFACS. Focus our attention on the physical explanation of the highest sensitivity location we found that the inflection point and the shock-cell positions are crucial in the determination of such a zone.

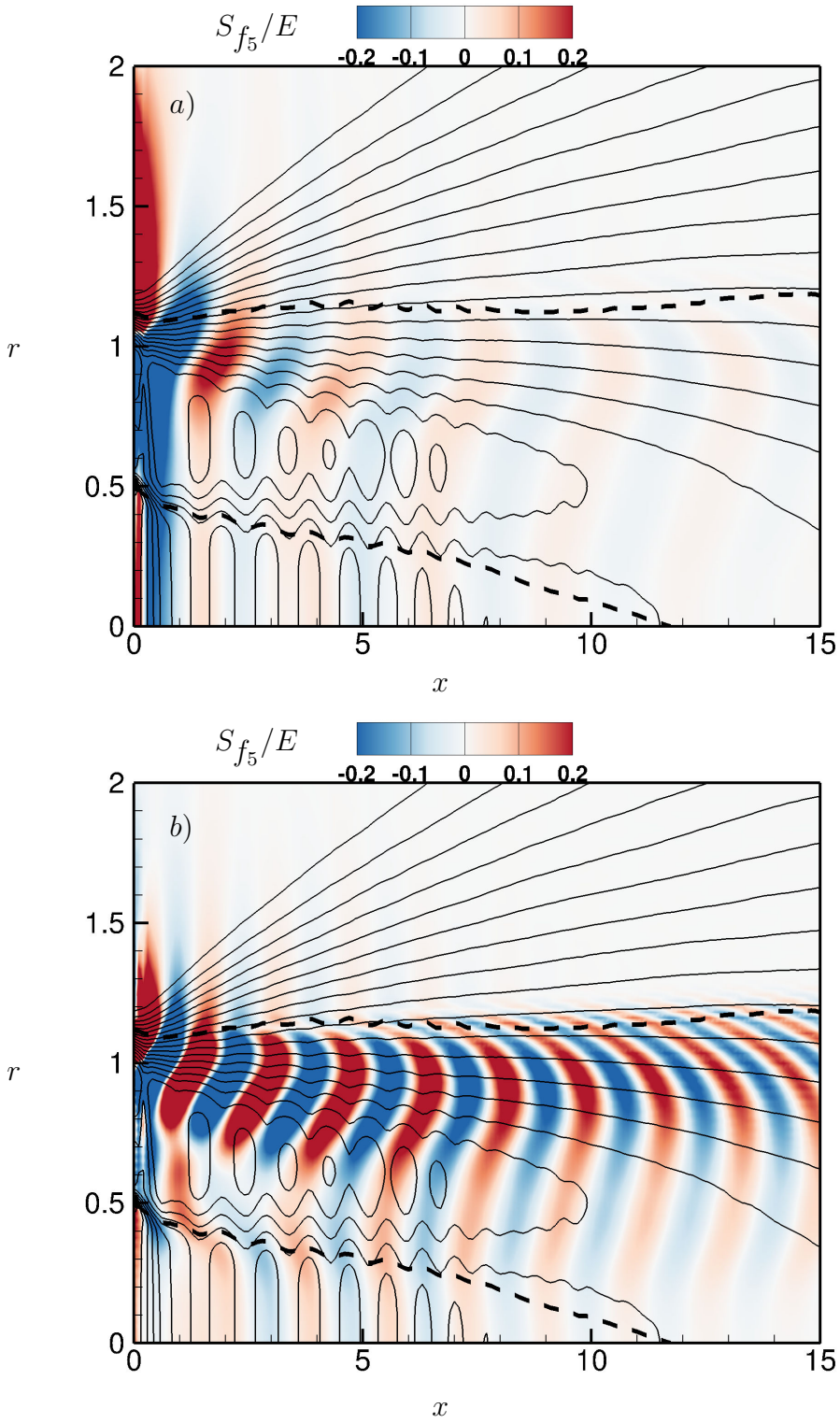


Figure 3.9: The normalized sensitivity with respect to the forcing acting in the energy equation, $S_{f_5}/E$, as a function of the spatial coordinates. The results refer to the under expanded dual stream baseflow 2.2.3 with a) $St = 0.6$ and b) $St = 1.0$. Solid lines are the isoline of the mean axial velocity, $\bar{u}_x$. The dashed line delimits the inflection point of the baseflow.

# Chapter 4

# Uncertainty Quantifications and adjoint PSE

The first objective of this chapter is to validate and compare adjoint-based sensitivity and other sensitivity methods and their possible relation to Uncertainty Quantification (UQ) analysis. Inspired by a simple toy models we have shown how can be a lower cost tool for mathematical analysis of complex problems of industrial interests. The second objective is to propose an Uncertainty Quantification of the incompressible single stream jet stability subjected to frequency variation. The governing equations are the low cost PSE model. This objective is strongly related to the noise sensitivity and control studies since it has been demonstrated that noise is originated from K-H instability in such a flow. Later, the adjoint PSE approach will be used, to make the link between sensitivity and UQ analysis as this quantification for Large Eddy Simulations or Reynolds Average Navier-Stokes simulations can be considerably expensive. Envelope curves of the standard deviation are determined and compared with good agreement for small variations of the input parameters in the first toy model. For the jet stability, it has been found that the growth rate is almost insensitive to small frequency variations and, on the other hand, the phases of the amplitude functions of the disturbance are extremely sensitive to frequency.

This work have been done in collaboration with the University of Greenwich.

## 4.1 Introduction

The generation of noise has been demonstrated to originate from Kelvin-Helmholtz instabilities amplifying in the jet stream. Some noise reduction can not be achieved before a deep analysis of the sensitivity of this instability to any flow perturbations or variations. This work is based on the Linearized Parabolized Stability Equations (LPSE) and their adjoint. Results are linked to uncertainty analysis. The base flow under consideration is the incompressible semi-empirical single jet 2.2.1. An Uncertainty Quantification of the jet flow stability subjected to frequency variation is proposed since noise emission are related to frequency. The remaining question is how sensitivity studies can be related to an Uncertainty Quantification? To answer we first propose a toy model on which both sensitivity and UQ analysis are carried out. UQ analysis is about determining the "reliability"

of the outputs of a problem under investigation when the inputs are not precise (input can varying or are uncertain). Such output uncertainties are represented by the standard deviation. For cases where the determination of uncertainties is of a high interest it is recommended to also look into the probabilistic or cumulate distribution functions. On the other hand, sensitivity analysis is about apportioning the uncertainty in the output with the different input uncertainties (gradients). In the following the gradients are calculated by four ways:

1. exactly calculating the sensitivity coefficients of the governing equations with the adjoint based approach
2. by integrating the standard deviation ratio from many direct computation
3. by a sensitivity indices
4. by a variance based sensitivity analysis.

The approach ii) and iii) can be qualified as One-factor-At-a-Time (OAT), just on component of the parameter vector is modified when the others are kept constant. In addition we present a way to perform local sensitivity using gradient of the direct equations.

A toy model is proposed as a test where the input uncertainties are set arbitrarily. This simple example wants to manifest the relation between adjoint-based sensitivity and other sensitivity methods that can also include an uncertainty analysis. The next section is an application on the stability of compressible single jet flow.

## 4.2 A model toy problem

### 4.2.1 ODE direct equations

The toy model is a set of two coupled ODE formulated as a classical optimization problem. Given the state vector $\mathbf{y} = [y_1, y_2]^t \in \mathbb{C}^2$ and the control or design parameter $\lambda = [\lambda_1, \lambda_2]^t \in \mathbb{C}^2$ , where the exponent $t$ always stands for transpose. The goal is to get, quantitatively or qualitatively, the variation of the cost function $E(\mathbf{y}, \lambda)$ with respect to the variation of the control parameter $\lambda$. Moreover the state vector $\mathbf{y}$ and the control parameter $\lambda$ are directly related by the constrained state equation $F(\mathbf{y}, \lambda) = \mathbf{0}$. The state equation of the toy model, 4.1, includes its initial condition and is given by:

$$F(\mathbf{y}, \lambda) = \dot{\mathbf{y}}(t, \lambda) - A(\lambda)\mathbf{y}(t, \lambda) - \mathbf{b}(\lambda)u(t) = \mathbf{0}, \qquad \mathbf{y}(0) = \mathbf{y}_0 = \begin{bmatrix} 0 \\ 1 \end{bmatrix} \tag{4.1}$$

with

$$A = \begin{bmatrix} -2i & \lambda_1 \\ \lambda_2\lambda_1^2 & -5 \end{bmatrix}, \quad \mathbf{b} = \begin{bmatrix} 1 + \lambda_2 \\ \lambda_1\lambda_2^2 \end{bmatrix}$$

where $i$ stands for the square root of $-1$ and $u(t)$ can be any forcing or control fixed in this simple model as a cosine function, $u(t) = \cos(3t)$.

The quadratic cost function (eq. 4.2) is defined as:

$$E(\lambda) = \frac{1}{2} \langle \mathbf{y}(t,\lambda), \mathbf{y}(t,\lambda) \rangle_t \,. \tag{4.2}$$

Given $\mathbf{v}$ and $\mathbf{u}$ as two arbitrary complex vectors the brackets $\langle \mathbf{v}, \mathbf{u} \rangle_t$ indicates an integral inner product in the complex plane defined by over the time domain $[0, T]$:

$$\langle \mathbf{v}, \mathbf{u} \rangle_t = \int_0^T \mathbf{v}^h \mathbf{u} \, dt,$$

where the superscript $h$ denotes transpose conjugate.

The solution can be integrated numerically or analytically and the stability will strongly depend on the values of $\lambda$ and the eigenvalues of $A$.

In order to perform an UQ or variance based sensitivity analysis a variation of the control parameter $\lambda$ has to be done. We decompose each component of the vector $\lambda$ into a reference value $\lambda_{i0}$ and a small perturbation $\Delta\lambda_i(\eta)$:

$$\lambda_i = \lambda_{i0} + \Delta\lambda_i(\eta), \quad \text{with} \quad i = 1, 2 \tag{4.3}$$

where the parameter $\eta$ is defined in the range $[-1 \;\; 1]$. The small perturbation $\Delta\lambda_i$ is defined by:

$$\Delta\lambda_i = \varepsilon_i f(\eta) \tag{4.4}$$

where the amplitude $\varepsilon_i$ is a constant and $f(\eta)$ is set as a sine or a Gaussian function.

In equation (4.3), and in the following $\eta$ in $\lambda_1$ and $\eta$ in $\lambda_2$ are considered as independent variables.

### 4.2.2 b - Sensitivity Analysis

A possible way to quantify uncertainties is to refer to the standard deviation of a variable under interest. The ratio between the variance of the cost function when varying one component $\lambda_i$ of the parameter $\lambda$, and the standard deviation of such parameter can be written as

$$\frac{\sigma^2_{E_{\lambda_i}}}{\sigma^2_{\lambda_i}} = \frac{\displaystyle\int_{-1}^{1} [E(\lambda_i) - \bar{E}_{\lambda_i}]^2 d\eta}{\displaystyle\int_{-1}^{1} [\lambda_i - \bar{\lambda}_i]^2 d\eta}. \tag{4.5}$$

The idea of using such ratio is to see whether a relation with local sensitivity exists. The over bar denotes the mean value of the function or of the parameter. In the previous equation, $E(\lambda_i)$ is the cost function where the component $\lambda_i$ may vary whilst the other components are kept constant. $\bar{E}_{\lambda_i}$ is the mean value and $\sigma_{E_{\lambda_i}}$ is the variance when considering $\lambda_i$ as the varying parameter.

As a first step, the integrals over $\eta$ are numerically computed over a constant mesh grid for $\eta = (\eta_k)_{k=1,N}$. To evaluate the integral of the numerator of equation (4.5), $N$

computations of the ODE system (eq. (4.1)) and $N$ evaluations of $E$ are required. The ODE is solved with a fourth order Runge-Kutta scheme.

As a second step, the sensitivity is now performed in order to get the gradients of the cost function $E(\lambda)$ with respect to $\lambda_i$, $\frac{\partial E}{\partial \lambda_i}$. The sensitivity $\frac{\partial E}{\partial \lambda_i}$ is calculated by solving the adjoint of the state model, see [7, 11]. The gradients are determined with a Lagrangian functional $\mathcal{L}$ where

$$\mathcal{L} = E - \langle \mathbf{y}^*, F(\mathbf{y}, \lambda) \rangle_t$$

As a result, the gradients and therefore the sensitivity function are the adjoint states:

$$\frac{\partial E}{\partial \lambda_i} = \langle \mathbf{y}^*, \mathbf{z} \rangle_t \,, \quad \text{with} \qquad \mathbf{z} = \frac{\partial A}{\partial \lambda_i} \mathbf{y}(t, \lambda) + \frac{\partial \mathbf{b}}{\partial \lambda_i} u(t) \tag{4.6}$$

where $\mathbf{y}^*$ is the adjoint state solution of:

$$\dot{\mathbf{y}}^*(t, \lambda) = -A(\lambda)^h \mathbf{y}^*(t, \lambda) - \mathbf{y}(t, \lambda), \qquad \mathbf{y}^*(T, \lambda) = \mathbf{0} \tag{4.7}$$

The adjoint equations are solved in reverse time, and a terminal condition at $t = T$ has to be set.

Only two computations of equations (4.1) and (4.7) are required to solve the sensitivity functions with the adjoint approach.

Finally, the numerical results $\sigma_E/\sigma_{\lambda_i}$ of equation (4.5) and the gradients $\frac{\partial E}{\partial \lambda_i}$ from (4.6) are compared and a very good agreement has been found as shown in table 1. It shows that for small uncertainties in the inputs, an adjoint-based sensitivity analysis provides the same numerical results than equation (4.5), which is computationally much more expensive and less exact. These results can be explained by the linearity that the response may have in such a small range. To explore such property, two more sensitivity analysis have been developed: a One-factor-At-a-Time (OAT) with sensitivity indices $SI$, this computation has been done at University of Greenwich, and a Variance-Based Sensitivity Analysis. Sensitivity indices provide a relatively good measure of the sensitivity of an output with respect to the variation in the inputs in the cases that the model is linear additive and the parameters are independent each other. This method also represents an inefficient sampling of the random space, as only the initial and last values of the interval are computed. The sensitivity indices can be obtained by:

$$SI_i = \frac{E(\lambda_{i_{\max}}) - E(\lambda_{i_{\min}})}{\lambda_{i_{\max}} - \lambda_{i_{\min}}} \tag{4.8}$$

In the literature, this coefficient $SI_i$ is often normalized by the mean quantities: $\bar{\lambda}_i/\bar{E}$. In Table 4.1 it can be seen that they are relatively close to the ones calculated by the previous two methods. This is a sign about the linear property our model is experiencing in the small range of uncertainties.

In addition to the previous methods, a Variance Based Sensitivity Analysis has been carried out in order to have a global understanding of the contributions of the input uncertainties. To develop such analysis, a decomposition of the variance is shown in equation (4.9), and sensitivity coefficients, defined differently from the previous approaches, are

| Method | $\frac{\partial E}{\partial \lambda_1}$ | $\frac{\partial E}{\partial \lambda_2}$ |
|---|---|---|
| Adjoint approach | 0.27262 | 1.7992 |
| OAT $\sigma$-ratio | 0.27084 | 1.8006 |
| OAT SI | 0.20670 | 1.3772 |

Table 4.1: Comparison among sensitivity methods.

| $\lambda_1$ | $\lambda_2$ | $\sqrt{S_2/S_1}$ |
|---|---|---|
| $S_1 = 0.0224$ | $S_2 = 0.9776$ | 6.606 |
| $S_{T_1} = 0.0228$ | $S_{T_2} = 0.9772$ | 6.547 |

Table 4.2: Results from Variance Based Sensitivity Analysis.

computed in equation (4.10) from its proportion with respect to the total variance. $S_i$ and $S_{T_i}$, in equation (4.11), are the first order and total sensitivities index respectively. In the following equations the multiple subscripts refer to second, third or higher order interactions, depending on the number of subscripts, see Saltelli et al. (2010)[109].

The results of such analysis are shown in table 2. Note that $m$ represents the dimension of the stochastic space.

$$\sigma_E^2 = \sum_{i=1}^{m} \sigma_{E_{\lambda_i}}^2 + \sum_{i=1,j>i}^{m} \sigma_{E_{\lambda_{ij}}}^2 + \sum_{i=1,k>j>i}^{m} \sigma_{E_{\lambda_{ijk}}}^2 + \ldots \tag{4.9}$$

$$1 = \sum_{i=1}^{m} S_i + \sum_{i=1,j>i}^{m} S_{ij} + \sum_{i=1,k>j>i}^{m} S_{ijk} + \ldots + S_{ijk,\ldots,m} \tag{4.10}$$

$$S_{T_i} = S_i + S_{ij} + S_{ijk} + \ldots + S_{ijk,\ldots,m} \tag{4.11}$$

The value of $\sigma_E^2$ has been calculated by Latin Hypercube Sampling with a total of 5000 samples, as shown in Fig. 4.1, and it has been found that, by comparing with the data from equation (4.5) and with the third columns of table 1 and 2, we get

$$\sigma_E^2 \approx \sum_{i=1}^{2} \sigma_{E_{\lambda_i}}^2 \qquad \text{or} \qquad \sqrt{\frac{S_2}{S_1}} \approx \frac{\partial E}{\partial \lambda_2} \Big/ \frac{\partial E}{\partial \lambda_1}$$

This is reflects the weak interaction of the higher order sensitivities, again due to the linearised behaviour of the model.

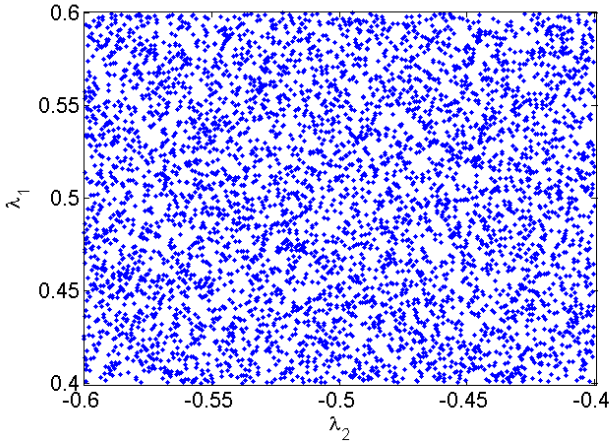


Figure 4.1: Latin Hypercube Sampling with 5000 samples.

### 4.2.3 c - Local sensitivity or gradient

Sensitivity based on global (integral of time or space) value is referred as a global sensitivity and in this section, local sensitivity means variation of a local (at a given time $t$) quantity.

Regarding the representation of the variation of the output, the uncertainty quantification can be localized at each time $t$. It is usual to plot the stochastic response with its mean and its standard deviation to display envelope curves in cases where the probabilistic or cumulate distribution functions are not of a high interest.

To perform this new study, from a sensitivity point of view, we are looking for the variation of $\mathbf{y}$ with respect to $\lambda_i$, that is $\dfrac{\partial \mathbf{y}}{\partial \lambda_i} = \mathbf{w}_{\lambda_i}$. In this case, we have two vectors of dimension two. The local sensitivities can be determined with the same ideas of the adjoint equation, by deriving equation (4.1) with respect to any $\lambda_i$:

$$\dot{\mathbf{w}}_{\lambda_i}(t) = A(\lambda)\mathbf{w}_{\lambda_i}(t) + \mathbf{z}, \qquad \mathbf{w}_{\lambda_i}(0) = \mathbf{0} \tag{4.12}$$

where $\mathbf{z}$ is the same as found in equation (4.6). The initial condition is null since the initial condition of the state $\mathbf{y}$ does not depend on $\lambda$. This equation can be called "gradient" equation and it is not the same as the adjoint or state equations. It is then easy to write the standard deviation ratio:

$$\frac{\sigma^{(n)}_{y_{\lambda_i}}(t)}{\sigma_{\lambda_i}} = \mathbf{w}^{(n)}_{\lambda_i}(t), \tag{4.13}$$

where the exponent $n$ indicates the component of the vector ($n$=1 or 2 here).

The stochastic mean and standard deviation envelopes are plotted in figure 4.2. It is an example, where $\lambda_1$ is fixed and $\lambda_2$ is the varying parameter calculated by ranging $\eta$ from $-1$ to $+1$ in equal step size (see equation (4.3)). The graph are representing the real part, the imaginary part and the modulus of the first component ($n = 1$) of the state vector $\mathbf{y}$ solution of the ODEs (eq. 4.1) for a given value of $\lambda_2$. The black full lines and

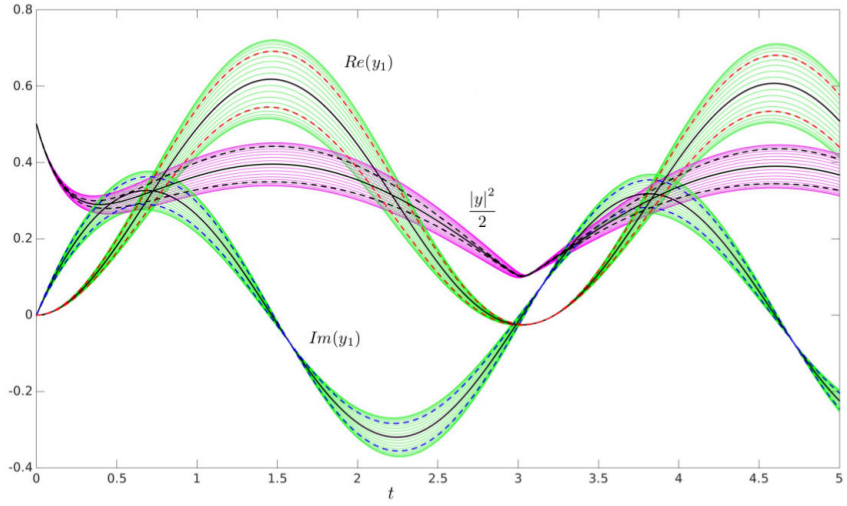


Figure 4.2: Mean and standard deviation envelopes of $y_1$ and $|y|^2/2$ with respect to a number of different values $\lambda_2$ function of time. Dash line: from gradients (sensitivity analysis), green full line: direct computations of equation (1).

the dash lines are respectively the real part, the imaginary part and the modulus of $\bar{y}^{(1)}_{\lambda_2}$ and $\bar{y}^{(1)}_{\lambda_2} \pm \sigma^{(1)}_{y_{\lambda_2}}$. Similar results are found with the second components of $\mathbf{y}$ and for $\mathbf{y}$ when $\lambda_1$ varies.

In conclusion two types of sensitivity or variance sensitivity can be determined:

1. Sensitivity of global function ($E$) or global variance sensitivity $E_\lambda$. One state and one adjoint equation computation are required from one hand. For UQ (and also for the presented Variance Based Sensitivity) at minimum $N$ state equation computations are necessary, when $N$ is normally large and depends on the integration method (Monte Carlo, quadrature, finite difference, etc).

2. Local sensitivity or local variance sensitivity $\mathbf{w}^{(n)}_{\lambda_i}(t)$. Denote $m$ as the dimension of the parameter $\lambda$, one state and $m$ gradient equation computations are required on one hand. For UQ (and Variance Based Sensitivity), a minimum of $N$ computations of the state equation are necessary.

"Gradient" and "adjoint" approaches can be some low computational techniques to analyse sensitivity or uncertainties of a given problem subjected to varying parameters with a given distribution. These cheap approaches remain interesting as soon as the variations of the inputs remain small. For this reason, the aim of future work is to explore the possibility of using a costless model based on adjoint sensitivity theory, to apply UQ sampling techniques. This would represent a very efficient tool.

## 4.3 PSE and UQ in jet stability analysis

In this section, an UQ study is performed by University of Greenwich by considering PSE as a black box with uncertain input and outputs.

The input uncertainty associated to the frequency $\omega$ has been modelled by an Uniform Probabilistic Distribution and then the Stochastic Collocation Method (SCM) with a Clenshaw- Curtis (C-C) Sparse Grid [113] has been implemented. SCM was developed by Mathelin and Hussaini [77] to improve the high costs of the Galerkin Polynomial Chaos method with non linear equations. For each collocation point, the CFD problem is solved deterministically, and the solution can be constructed as an expansion:

$$\Phi(\mathbf{x}, \beta) \approx \sum_{i=1}^{N} \Phi_i(\mathbf{x})\, \ell_i(\beta) \tag{4.14}$$

where $\Phi_i(\mathbf{x})$ with $\mathbf{x} = (x, r)$ stands for the deterministic solutions and $\ell_i$ are the Lagrange interpolant polynomials. Statistical moments can be obtained by applying quadrature rules and SCM represents a very efficient option for lower dimension problems in comparison with sampling techniques such as Monte-Carlo. For higher dimension problems, sampling techniques use to be more suitable.

In this paper, the collocation points of the sparse grid have been determined according to the C-C quadrature nested rule. Special attention must be paid in the Probabilistic Density Function of the random variable, $\xi \in \Xi$, as we have to perform a mathematical transformation from the physical random variable space to an artificial stochastic space, called $\alpha$-domain but here referred to as $\beta$-domain ( $\beta = \mathcal{S}_\xi(\xi)$), as $\alpha$ is used for the wavenumber. This transformation is an important difference with respect to other UQ methods.

Regarding the source of uncertainty, it has been based on a 10% of variation of the frequency, whose deterministic base value is imposed to $\bar{\omega} = 1.2\pi$, the mean value. An uniform distribution $\omega \sim U(-0.1\bar{\omega}, 0.1\bar{\omega})$ is set.

In Figure 4.3, the mean and standard deviation of the real and imaginary parts of $\alpha = \alpha_r + i\,\alpha_i$, the complex axial wavenumber, is plotted for 33 Clenshaw-Curtis quadrature nodes. It can be observed that the imaginary part is not very sensitive with respect to the uncertain frequency in long distances, whilst the real one is very slowly changing along the $x/D$ axis of the jet. In conclusion a small uncertainty on the frequency wave will modify the wavelength of the sound wave but the instability (growth rate) of the flow will remain almost unchanged.

In Figure 4.4, the mean value and envelopes of the real part of the amplitude function of the streamwise and radial velocity are displayed for $r/D_j = 0.51$. The uncertainty on the frequency generates strong variation on the phases of the amplitude functions, so that the real or imaginary parts are very sensitive to frequency variations. This results have been confirmed by the sensitivity analysis based on adjoint PSE.

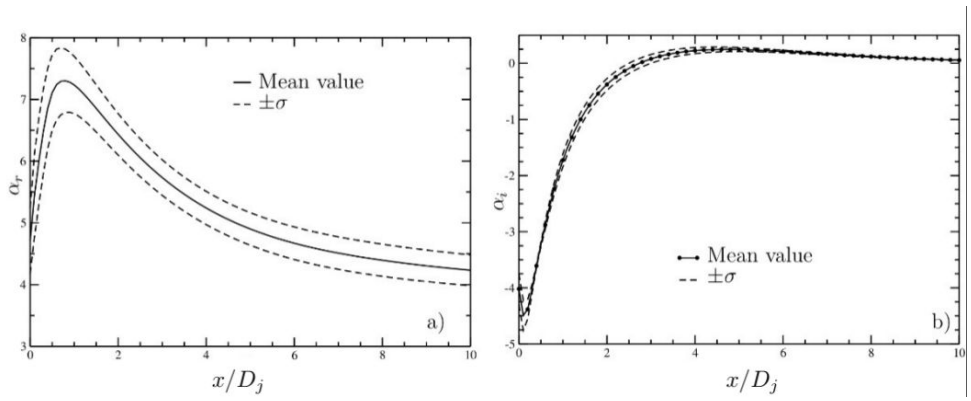


Figure 4.3: Mean and standard deviation envelopes of the wavenumber $\alpha_r$ (a) and of the growth rate $\alpha_i$ (b).

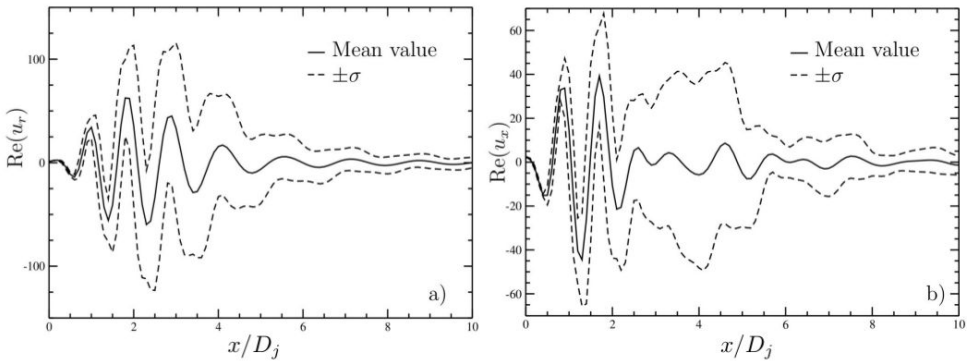


Figure 4.4: Mean and standard deviation envelopes of the real part of the amplitude functions $u_r$ (a) and $u_x$ (b), $r/D_j = 0.51$.

## 4.4 Conclusions

The relationship between a Uncertainty Quantification (standard deviation ratio) and a adjoint-based sensitivity analyses have been demonstrated, first on a toy ODE model and after on a PDE stability problem. The use of adjoint equations required few computations comparing to some general usual UQ method, since if $m$ is the number of parameters with uncertainties, only $m + 1$ computations are necessary to get the standard deviation and the envelope curves. It has also been noticed that an uncertainty frequency wave modify the wavelength of the sound wave but the growth rate will remain insensitive.

The next step will be to perform a propagation of instability by taking into account uncertainties of the mean flow into the stability of single and double-stream jet and to propagate the uncertainties to the far field noise emission. Also, as here has been demonstrated that the sensitivity coefficients can be quickly obtained by the adjoint approach, the next step is to explore the possibility of quantify uncertainties by using a costless surrogate model based on the exactly calculated adjoint-based sensitivity coefficients.

# Chapter 5

# Acoustic field analysis

## 5.1 Introduction

As explained in Section I, the acoustic analogy can be considered as a hybrid approach (Casalino (2003)[19]). In the current section the FW-H equation and integral solution are reported (see appendix for details). The FW-H acoustic analogy represents a generalization of Lighthill's acoustic analogy for flows including bodies in arbitrary motion. In this generalization the fluid is unbounded but partitioned into regions by an integration surface, as schematically shown in fig 5.1 . This surface does not need to coincide with a physical body and can be permeable [16, 32]. The surface requirements are discussed in details by Brentner and Farassat (1998)[16].

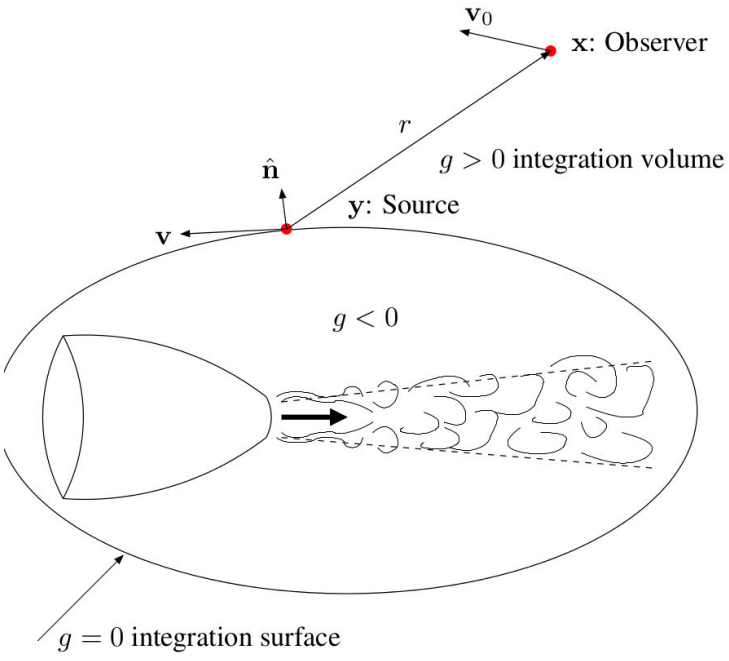


Figure 5.1: Radiation in an unbounded flow.

Let $g(\boldsymbol{x},t)=0$ be the equation describing the moving control surface, whose points move at velocity $\boldsymbol{v}(\boldsymbol{x},t)$[19]. $g$ is defined to satisfy the property $\nabla g=\hat{\boldsymbol{n}}$ on the surface, where $\hat{\boldsymbol{n}}$ is the outward pointing unit normal vector. Following this procedure, the flow is partitioned into three regions according to the value of $g$. A point enclosed by the integration surface satisfies $g<0$ and this flow field portion can be replaced by a quiescent fluid. Mass and momentum sources are then distributed on the surface $g(\boldsymbol{x},t)=0$, which allows the conservation laws across $g(\boldsymbol{x},t)=0$ to be satisfied. This process is carried out from the time-resolved estimates of pressure, density and velocity on the FW-H integration surface, obtained independently by CFD. The mass and momentum conservation equations are recast to obtain the FW-H equation. A more compact form of this equation is given by Casalino (2003)[19] and reported here:

$$\Box\left\{(\rho-\rho_0)c_0^2H(g)\right\}=\frac{\partial^2\left\{T_{ij}H(g)\right\}}{\partial x_i\partial x_j}-\frac{\partial\left\{L_i\delta(g)\right\}}{\partial x_i}+\frac{\partial\left\{Q_i\delta(g)\right\}}{\partial t}, \tag{5.1}$$

where $H(g)$ is the Heaviside function and in the first source term on the right hand side $T_{ij}$ is the Lighthill stress tensor [66]. The second and third contributions are, respectively, the surface source distributions of momentum (dipole) and mass (monopole). Expressions for these source terms are reported here:

$$T_{ij}=\rho u_iu_j+(p'-c_0^2\rho')\delta_{ij}-\tau_{ij}, \tag{5.2}$$

$$L_i=P_{ij}\hat{n}_j+\rho u_i(u_n-v_n),\quad P_{ij}=(p-p_0)\delta_{ij}-\tau_{ij}, \tag{5.3}$$

$$Q=\rho_0U_i\hat{n}_i, \tag{5.4}$$

with

$$U_i=\left(1-\frac{\rho}{\rho_0}\right)v_i+\frac{\rho u_i}{\rho_0}, \tag{5.5}$$

where $u_n$ and $v_n$ are the flow and surface velocity in the outward normal direction $\hat{n}$. The three source terms in equation 5.1 are referred to respectively as quadrupole, dipole and monopole sources. The monopole and dipole contributions are often referred to as respectively thickness and loading noise for analogy with helicopter rotor applications. While the quadrupole term represents a volume distribution and is computationally the most expensive to estimate, the loading and thickness noise are surface distributions as indicated by the presence of the Dirac delta function multiplying these contributions, which shifts the value of the variables on the FW-H integration surface. The volume source distribution accounts for all the non-linearities in the flow. The effects of convection with variable speed, non linear wave propagation and steepening, variable speed of sound, generation of noise by shocks, vorticity and turbulence in the flow field are all included in this source term[16]. When the integration surface is taken coincident with a solid body, a physical interpretation of loading and thickness noise is available. The loading noise takes into account the effect of the interaction of the flow with vibrating surfaces, reproducing

the net unsteady forcing acting on the fluid as a result of the presence of the body. The thickness noise is originated by the motion of the surface in the normal direction[31] and it represents a displacement effect [35]. It is determined completely by the geometry and kinematics of the body[16]. The FW-H integral solution [35] is given by the following integral:

$$\begin{aligned} 4\pi c_0^2(\rho(\boldsymbol{x},t)-\rho_0) = &\int_V \nabla_x \cdot \nabla_x \cdot \left[\frac{\boldsymbol{T}J}{r|1-M_r|}\right]_{ret} d\eta - \\ &\int_{g=0} \nabla_x \cdot \left[\frac{\boldsymbol{P}\cdot\hat{\boldsymbol{n}}A}{r|1-M_r|}\right]_{ret} dS(\eta) + \\ &\int_{g=0} \frac{\partial}{\partial t}\left[\frac{\rho\boldsymbol{u}\cdot\hat{\boldsymbol{n}}}{r|1-M_r|}\right]_{ret} dS(\eta). \end{aligned} \tag{5.6}$$

Expressions for the terms in equation 5.6 are given in equations 5.7-5.10.

$$\boldsymbol{y} = \boldsymbol{\eta} + \int_{\infty}^{\tau_e} c_0 \boldsymbol{M}(\boldsymbol{\eta},\tau')d\tau', \quad \hat{\boldsymbol{n}} = \frac{\nabla_x f}{|\nabla_x f|}, \tag{5.7}$$

$$J = \exp\left(\int_{\infty}^{\tau_e} \nabla \cdot c_0 \boldsymbol{M}(\boldsymbol{\eta},\tau')d\tau'\right), \quad A = \frac{\nabla_y f}{|\nabla_\eta f|}, \tag{5.8}$$

$$\boldsymbol{P} = p\boldsymbol{I} - \tau, \quad M_r = \boldsymbol{M}\cdot\boldsymbol{r} \tag{5.9}$$

$$\tau_e = t - \frac{r}{c_0} \tag{5.10}$$

Where $\boldsymbol{M}$ is a vector with components the mach number in the three spatial directions.

### 5.1.1 Advanced time formulation AFW-H

Casalino [19] reports the integral solution of the FW-H equation in the advanced time formulation, which is here referred to as AFW-H. In this solution, the acoustic pressure fluctuation $p' = p - p_0$ perceived by an observer located at the vector position $x$ at time $t$ is given by:

$$p'(\boldsymbol{x},t) = p'_Q(\boldsymbol{x},t) + p'_L(\boldsymbol{x},t) + p'_T(\boldsymbol{x},t), \tag{5.11}$$

where subscripts $Q$, $L$, and $T$ are, respectively, the quadrupole, loading, and thickness noise contributions to $p'$ from the source field located at $\boldsymbol{y}$ generated at retarded time $\tau_{ret} = t - c_0^{-1}|\boldsymbol{x} - \boldsymbol{y}(\tau_{ret})|$. $\tau_{ret}$ accounts for the time of flight of the noise propagating from $\boldsymbol{y}$ to $\boldsymbol{x}$ at the constant speed of sound $c_0$. Expressions for these contributions are given in Casalino[19] and are reported in the appendix.

### 5.1.2 Implementation of AFW-H analogy

A discretized form of equation 5.11 is implemented in a code developed at the University of Leicester. The quadrupole source term is neglected. It is often possible in CAA to neglect the volume source distribution of $T_{ij}$, primarily due to the quadrupole term representing the smallest contribution to noise radiation at low Mach numbers. One further advantage of this approach is the considerable decrease in the computational cost of the simulation, by reducing a three dimensional numerical integration to a two dimensional one. The FW-H algorithm is structured in the following way: at each discrete acoustic time $\tau^n$, a loop over the observer positions $x_i$ is performed; for each $x_i$, the contribution from the FW-H surface is estimated, by looping over the $S_j$s; finally, for each $S_j$, a loop is performed over the surface elements $dS_k$ of $S_j$ , on which the discretized form of the $L$ and $T$ terms is evaluated. The advanced time relative to the $dS_k$s is also estimated from the retarded time equation [19] in order to save the $p'$ contribution at the correct observer time. This process is then repeated at different discrete acoustic times $\tau^n$. Advancing in time, a pressure fluctuation history is reconstructed and the final output of the tool is a matrix storing, for each observer position, the pressure fluctuation $p'(x_i, t)$ as a discretised time array. For each discrete acoustic time $\tau^n$, the acoustic analogy post processor reads the CFD solution and retains the flow field data relative to the previous iteration $\tau^{n1}$. This enables the estimation of the source time derivatives using the backward finite difference approximation

$$\dot{z} = \frac{\partial z}{\partial \tau} \approx \frac{z^n - z^{n-1}}{\Delta \tau} \tag{5.12}$$

where $z$ is a source term variable. Considering the different characteristic time and length scales between the hydrodynamic and the acoustic fields, the acoustic simulation usually requires a lower resolution in time. For this reason, the new tool is designed such that it can perform the numerical integration every $m$ CFD time steps. For the jet test case from Bogey and Bailly (2006)[15], the following relationship between the acoustic and the CFD time steps is adopted:

$$\Delta \tau = 10 \tau_{CFD} \tag{5.13}$$

This choice allows the CAA simulation to use less computer time and memory.

## 5.2 PSE coupled with AFW-H analogy

as observed by Cheung et al. (2007)[22] PSE are accurately computed inside the jet, but fail to capture the acoustic radiation outside the mixing layer region. Acknowledging this limitation, several ways are possible to reconstruct the acoustic radiation outside the jet, i.e: techniques based to Kirchhoff surface strategy[64, 14, 123], by solving the Linear Euler Equation or by using an acoustic analogy. In the present study, the latter approach is employed, an AFW-H solver is used in this thesis. The solver has been developed at the University of Leicester and tested on noise source fields of increasing complexity (monopole, dipole and supersonic single stream jet). For the supersonic single stream

jet case the predictions are compared with the ones from the elsA CFD solver by Onera, DiStefano et al. [116] (2015). The elsA CFD solver contains the same acoustic analogy formulation (AFW-H) of the code used in this theses, which provides an opportunity for verifying the implementation of the advanced time algorithm on the same CFD data set.

In this chapter we compute the noise radiated from the jet in two steps:

1. the evolution of the instability waves inside the jet is computed using the PSE method

2. the noise radiated from these waves is calculated by solving the wave equation using the AFW-H solver (University of Leicester).

This methodology has been, first, validated by a test case which the result is compared with those found in the literature and then applied to the dual stream jet (case IV 2.2.3).

## 5.3 Validation

### 5.3.1 Supersonic single stream jet

The numerical results presented here refers to the semi-empirical supersonic single stream jet (case II 2.2.2). Once the PSE is computed the integration surface is set, inspired by the work of Léon and Brazier (2011)[64], in an almost uniform region where the mean axial velocity is less than 0.5% of $\bar{u}(0,0)$. The surface start at $1.9D$ in the axial position $x = 0$ with an angle of $4°$. We present the results for the Strouhal number $St = 0.4$ and for helical mode $m = 1$ which is the instability wave mode used to excited the jet in the experiment of Troutt and McLaughlin (1982)[129].

In order to compare our results to those found in the experiment we reconstruct a 'greed' of observers outside the integration surface, (see fig. 5.2).

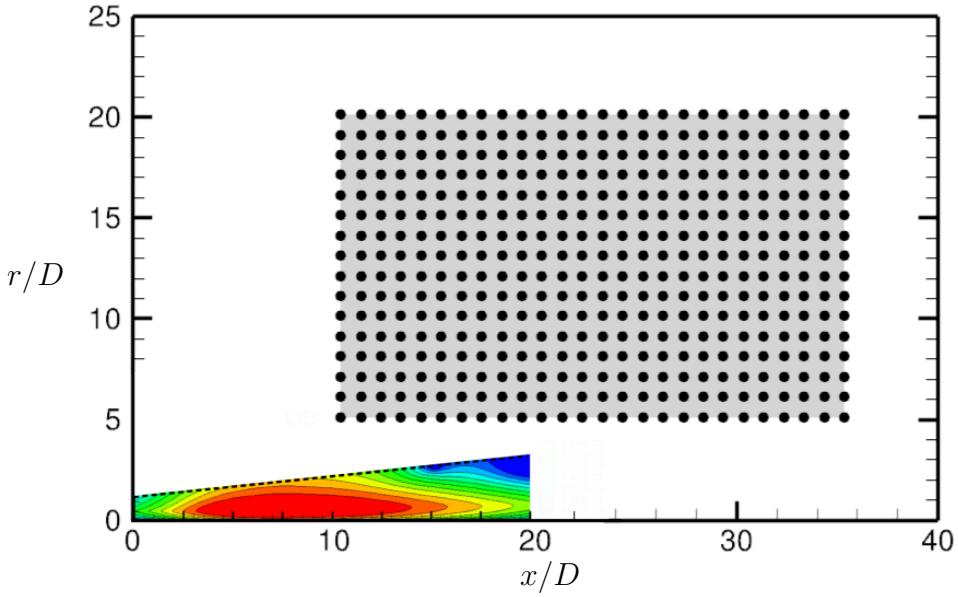


Figure 5.2: A schematically representation of the inner and outer solution. The PSE computation (in colour) is projected in the integration surface (dot line). The outer solution is arranged in the gray zone made up by a greed of observers (dark circles).

In the figure are put in evidence the inner solution obtained by solving the PSE (delimited by the integration surface) equations and the outer solution computed in the greed of observers by solving the AFW-H acoustic analogy.

In figure 5.3-a is shown the SPL contours levels filtered around the fundamental excitation frequency. This results confirm as the noise from coherent structures tends to propagate in the downstream direction. In fact, in the experiment the noise is radiated at an angle of 36°. Figures 5.3-b shows the sound pressure levels (in dB) radiated from the instability waves with the frequency $St = 0.4$ and $m = 1$ to the far field. The result is obtained with the AFW-H solver (developed at the University of Leicester). We see that the noise is radiated in a confined region and an intense noise is radiated in a fixed direction which is inclined at 35°. On comparing the preferred radiation of the noise and as well, simply, the two figures we observe an excellent agreement between the experiment and the computation results. The agreement between the calculated and the measured 150 dB and 148 dB contours is almost perfect. The lobed nature of the contours, the direction of the lobe and the spacings of the contours are correctly predicted.

Notice that since the PSE results have an unknown multiplicative constant (see eq. 2.10), the absolute pressure level can not be predicted. The magnitude of the constant is chosen such that the computed SPL at the point marked by a black bullet in figure 5.3-a is 148 dB.

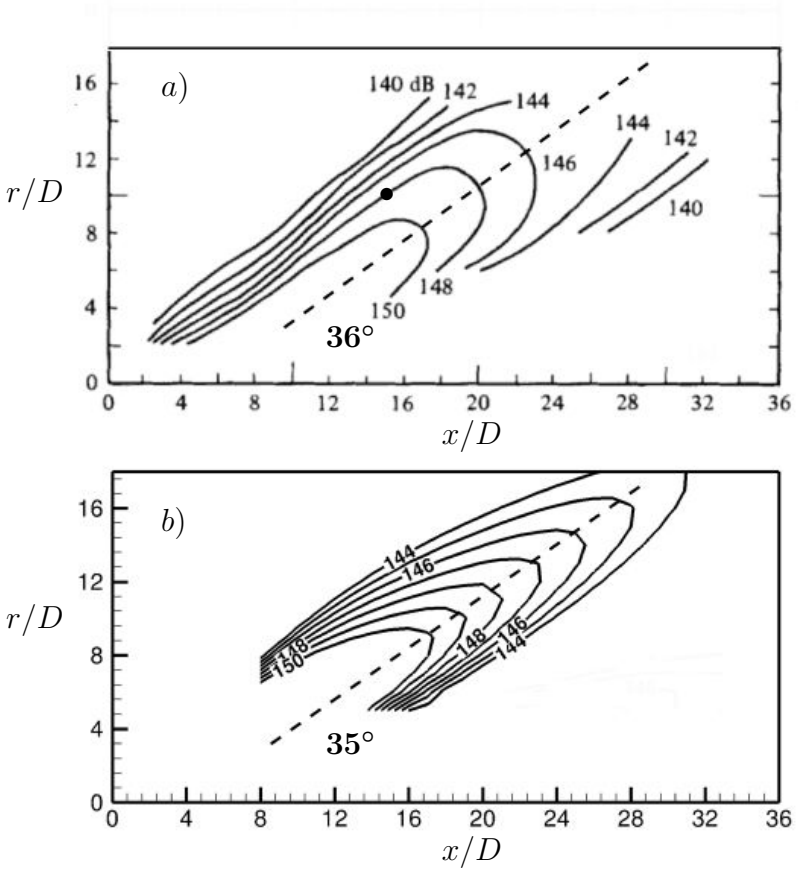


Figure 5.3: Sound Pressure Level contours for jet excited at $St = 0.4$ and $m = 1$: a) measured Troutt and McLaughlin (1982)[129]; b) calculated (IMFT).

### 5.3.2 Turbulent under-expanded dual-stream jet

In this section the noise emitted from the axisymmetric instabilities, $m = 0$, in the dual stream jet (case IV 2.2.3) is investigated. The results obtained from the PSE/FW-H computations are compared to those found by directly coupling the LES with the FW-H acoustic analogy.

Four different Strouhal numbers are taken into account, $St = 0.4, 0.6, 0.8, 1.0$. All the computations were initialized with the secondary mode ($KH_2$) which is the most unstable mode. The cone integration surface intersect the initial streamwise coordinate, $x = x_0$, at the radial value $r = 1.22D_p$ and the angle with respect to the axial axis is equal to 7.69°. This choice allow the solution to propagate in an almost uniform region where the mean axial velocity is less than 0.5% of $\bar{u}(0, 0)$. In figure 5.4 the spatial distribution of the sound pressure level, SPL, is obtained by running the acoustic analogy in the domain $[0, 30] \times [6, 20]$. The SPL is higher for small values of the Strouhal number. The sound

propagate mainly in two distinct directions for Strouhal $St = 1.0$, 0.8 while one of them vanish for Strouhal numbers $St = 0.6$, 0.4.

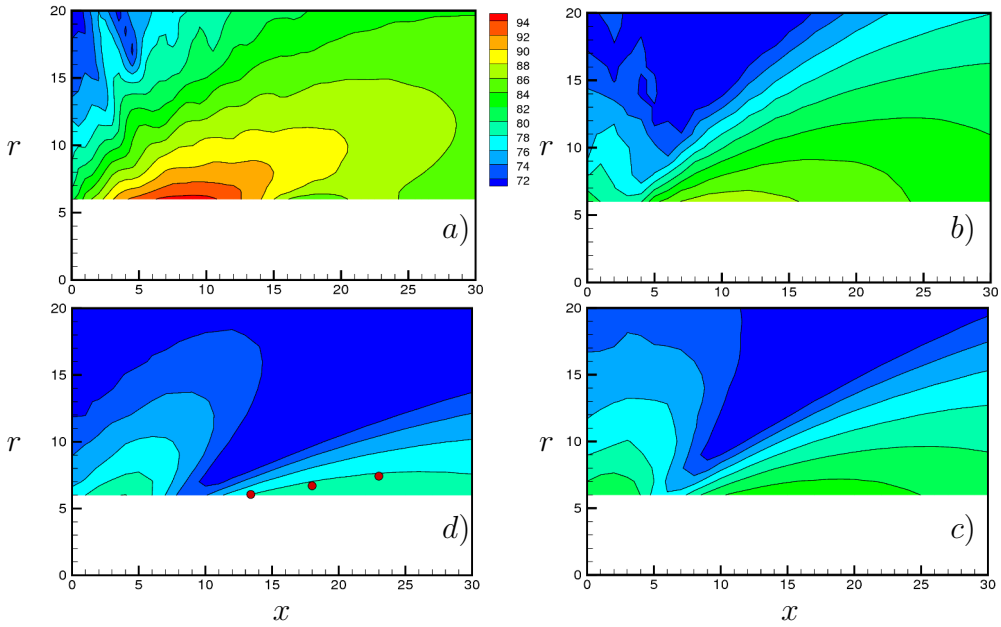


Figure 5.4: Spatial distribution of the Sound Pressure Level. Turning clockwise from the top left the Strouhal number is 0.4, 0.6, 0.8, 1.0, respectively.

In the work of Perez et al. (2016)[94] the noise emitted by case 2.2.3 is investigated. The FW-H analogy is computed along three points $P_1 = (13.4, 6.05)$,$P_2 = (18.0, 6.70)$ and $P_3 = (23.0, 7.42)$, see figure 5.4-d. The component of the sound associated to the axisymmetric instability is computed by a modal decomposition of the signal. The intensity of the sound can not be directly extracted by the PSE approach, in fact in equation 2.10 the unknown value $\varepsilon$ has to be defined. The parameter $\varepsilon$ has been set by imposing the SPL value for Strouhal $St = 0.8$ in the $P_1$ position, the green point in figure 5.5-a. The remaining positions are computed by imposing such value of $\varepsilon$. The SPL computed coupling the LES to the FW-H analogy (Perez et al. (2016)[94]) in the three positions $P_1$, $P_2$ and $P_3$ are plotted in red full line in figure 5.5-a, -b and -c respectively. The results of the PSE/FW-H are in black circles. The dot lines refers to the linear regression of the data. For the position $P_1$ the dependence of the SPL to the Strouhal number is over estimated if compared to the LES/FW-H results. For the positions farther to the exit of the nozzle the match is almost perfect.

More calculations should shown that the PSE results will however be approximately aligned while the LES results exhibit some oscillations not captured by the stability analysis. This discrepancies could be attributed to the nonlinearities and small-scale instationnarities present in the flow and not solved by the mean flow operator associated to a linear stability analysis. However one can be satistied to get the good trend with this latter low-cost model.

Concluding, the physics of propagation of the sound is very well captured by our model showing the consistence of this approach.

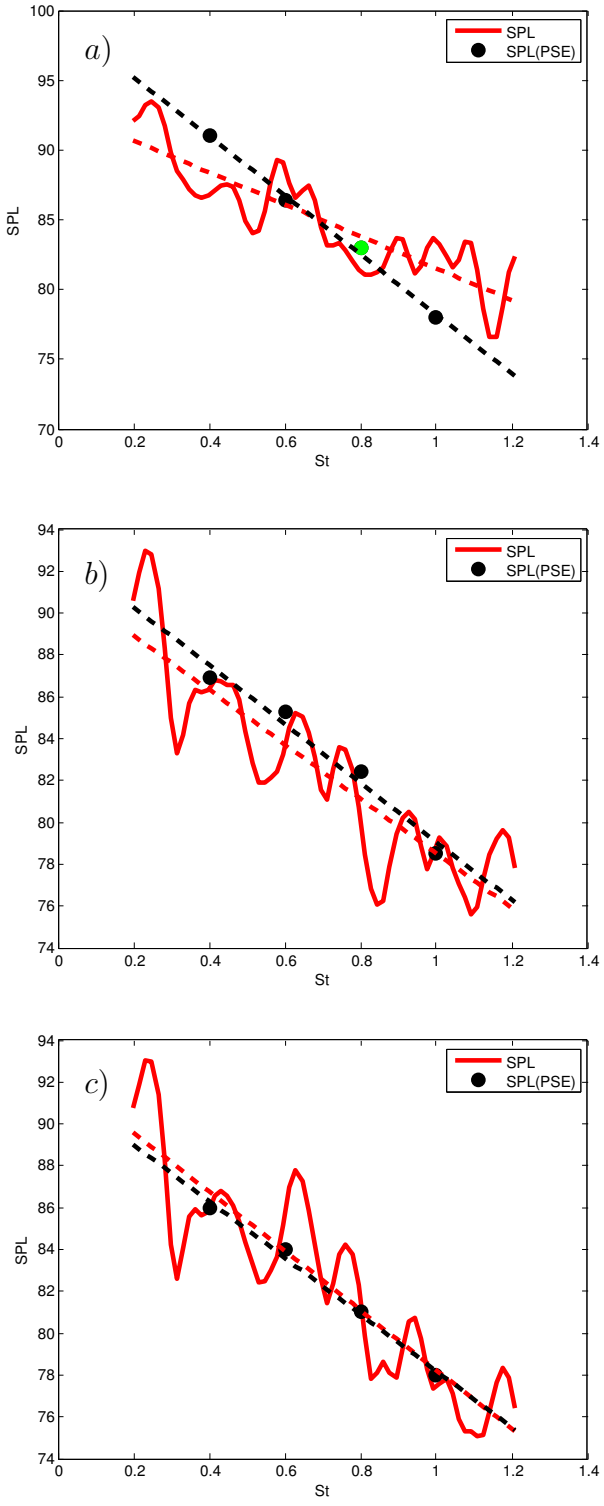


Figure 5.5: The SPL is computed for the three different positions $P_1$, $P_2$ and $P_3$ in figure a), b) and c) respectively. The red line refers to the SPL obtained by coupling the FW-H acoustic analogy with the LES computation (see Perez et al. (2016)[94]). The dark bullet are the SPL estimated by our appraoch (developed in collaboration with the University of Leicester). The dot lines refers to the linear regression of the two computations.

## 5.4 Conclusion

In this chapter has been presented a low cost computational model able to predict the noise emitted by the evolution of a small disturbance with a single frequency and a fixed azimuthal wavenumber. The solution is the results of a coupling between the PSE solver and the acoustic analogy solver; this development has been done in collaboration with the University of Leicester. The model allows to a low cost study of the noise emission in turbulent jet and can be applied in future for many cases of industrial interest. The total computations is very efficient and take about 20 minutes running in a normal laptop. The application shown in this chapter a very good agreement is found between the computed and the measured Sound Pressure Level. The model predict very accurately the noise emission also for jets with high complexity, like the turbulent under-expanded dual stream jet studied in this thesis work. This methodology leave open the possibility to investigate noise in jet with high complexity efficiently.

# Conclusions

## Summary of main results

In this thesis many configurations are investigated. For PSE and the corresponding sensitivity of the jet flow to noise the main objective was to investigate the complex configuration of a dual stream under-expanded jet of industrial interest, obtained thanks to the accurate LES computation from CERFACS[94].

In the first part of this work (chapter I and more in details in chapter II) the PSE approach is presented. The PSE solver, developed by the ONERA's team[63] was upgrade by a stabilization procedure in order to investigate more complex flows. A parametric study with respect to the Strouhal number pointed out that the shock cell play a crucial role in the growth rate of the instability, otherwise variations in the frequency of the instability seems to have a less effect in the growth rate. This study emphasize the role of the two unstable Kelvin-Helmholtz modes. The K-H modes related to the secondary shear-layer is the most unstable mode. The instabilities that grow in the secondary shear layer present a weakly interaction to the primary shear layer. On the other hand the instabilities that grow in the primary jet highly interact with the secondary jet, confirming that for PSE is very difficult to distinguish between the two unstable modes. This result is in agreement with those found in the previous works of Léon and Brazier(2011) [64] and Sinha et al. (2016)[111].

Then, a sensitivity analysis of the instabilities is made in chapter III. Validation of the sensitivity analysis based on adjoint PSE for subsonic and supersonic single-stream jet flow has been carried out. Especially, the sensitivity obtained by adjoint-based approach and by Finite-Difference method are compared. The most sensitive region with respect to external forcing has been identified close to the exit nozzle into the shear-layer in the external boundary of the potential core of the jet. For the dual stream jet case a new application about the interaction betweens the Kelvin-Helmholtz instabilities and the shock-cells has been presented. During the identification of the highest sensitivity location a crucial role of the inflection point has been pointed out. Furthermore, the results show a strong dependence of the sensitivity to the spatial coordinates. These remarks should be taken into account before proposing a new noise control strategy by a very deep analysis of the interaction flow/actuator.

In chapter IV the relationship between sensitivity and Uncertainty Quantification (UQ) has been investigated, firstly, by a toy model and then directly applied on the PSE stability problem in collaboration with the University of Greenwich. Make a link between

sensitivity and UQ could be an objective of industrial interest because, generally, the sensitivity solver are much less expensive in term of computational cost if compared with the classical UQ approach. The UQ applied to the PSE model shows that the uncertainty in the value of the instability frequency wave modifies the wavelength of the sound wave, but finally and astonishingly the growth rate will remain quite insensitive.

An important step of this work is to couple the stability and sensitivity solvers to a far-field sound propagation approach, Chapter V. Validation of this methodology for cases II 2.2.2 and IV 2.2.3 have been performed, in collaboration with the University of Leicester, showing encouraging results for the prevision of the noise emission in jets.

# Perspectives

A low computational cost model of the shear-layer instability modes in the co-axial jet, which takes into account the shock-cell system in the bypass stream, based on the Parabolized Stability Equations has been developed. In addition, a far field acoustic simulation coupled with PSE results has been validated for cases II 2.2.2 and IV 2.2.3 and can be use to deeper investigate the noise in the dual stream jet configuration. The next step will be to develop a global sensitivity study for the full model (PSE + APSE + sound propagation) in the near and far field. Moreover, we should be able to provide in the base of adjoint equations an extension to sensitivity of the noise to various possible perturbations or forcing, related to aeroacoustic control. This numerically low-cost tool can be used for predicting shock-cell noise. As discussed in [131, 23, 64] many questions remains relative to the location and the quality of the coupling between the PSE pressure disturbance and the far-field zone.

In parallel, the propagation of instability should be taken into account uncertainties of the mean flow variations. These uncertainties of the mean flow, probably, are propagated into the far field noise emission. Finally, the implementation of the 'gradient' PSE solver (see eq. 4.12) could be a good alternative to investigate parameters dependences that adjoint PSE are not able to solve efficiently (i.e. $\frac{\partial \alpha}{\partial \omega}$). Because the sensitivity coefficients can be quickly obtained by the adjoint approach, a future step is to explore the possibility of quantify uncertainties by using a costless surrogate model based on the exactly calculated adjoint-based sensitivity coefficients, as done for the toy model in chapter IV.

# List of Tables

# List of Figures

# Bibliography


[1] Abergel, F., and Temam, R. On some control problems in fluid mechanics. *Theoret. Comput. Fluid Dyn. 1* (1990), 303–325.

[2] Airiau, C. *Stabilité linéaire et faiblement non-linéaire d'une couche limite incompressible par un système d'équations parabolique.* PhD thesis, Ecole Nationale Supérieure de l'Aéronautique et de l'Espace, Toulouse, France, Juin 1994.

[3] Airiau, C. Non-parallel acoustic receptivity of a Blasius boundary layer using an adjoint approach. *Flow Turbul. Combust. 65*, 3/4 (2000), 347–367.

[4] Airiau, C. Stabilité, réceptivité et contrôle optimal d'écoulements cisaillés: approches adjointes. In *Habilitation á diriger des recherches* (Toulouse, France, 2004).

[5] Airiau, C., Bottaro, A., Walther, S., and Legendre, D. A methodology for optimal laminar flow control: Application to the damping of tollmien-schlichting waves in a boundary layer. *Phys. Fluids 15*, 5 (2003), 1131–1145.

[6] Airiau, C., and Casalis, G. Boundary layer linear stability using a system of parabolic equations. *Rech. Aérosp. 5* (1993), 57–68.

[7] Airiau, C., Walther, S., and Bottaro, A. Boundary layer sensitivity and receptivity. *C.R. Mecanique 330* (2002), 259–265.

[8] Andersson, P., Henningson, D., and Hanifi, A. On a stabilization procedure for the parabolic stability equations. *Journal of Engineering Mathematics 33* (1998), 311.

[9] André, B., Castelain, T., and Bailly, C. Broadband shock-associated noise in screeching and non-screeching underexpanded supersonic jets. *AIAA Journal 51 (3)* (2013), 665–673.

[10] Ansaldi, T., and Airiau, C. Non viscous sensitivity analysis of noise generation mechanism in a low mach number jet. In 50th 3AF international conference (Toulouse, France, 2015), no. FP59.

[11] Ansaldi, T., and Airiau, C. Sensitivity analysis for subsonic jet using adjoint of non local stability equations. No. AIAA 2015-2219.

[12] Ansaldi, T., Airiau, C., Pérez, C., and Puigt, G. PSE-based sensitivity analysis of turbulent and supersonic single stream jet. No. 16-3052 in AIAA-paper.

[13] Bagheri, S., Schlatter, P., Schmid, P. J., and Henningson, D. S. Global stability of a jet in crossflow. *J. Fluid Mech. 624(1)* (2009), 33–44.

[14] Balakumar, P. Prediction of supersonic jet noise. No. AIAA 98-1057.

[15] Bogey, C., and Bailly, C. Computation of a high Reynolds number jet and its radiated noise using Large Eddy Simulation based on explicit filtering. *Computers and Fluids 35(10)* (2006), 1344–1358.

[16] Brentner, K. S., and Farassat, F. Analytical comparison of the acoustic analogy and Kirchhoff formulation for moving surfaces. *AIAA Journal 36 (8)* (1998), 1379–1386.

[17] Brentner, K. S., and Holland, P. C. An efficient and robust method for predicting helicopter rotor high-speed impulsive noise. *J. Sound. Vib. 203* (1997), 97–100.

[18] Cambier, L., Heib, S., and Plot, S. The Onera elsA CFD software: input from research and feedback from industry. *Mechanics and Industry 14* (2013), 159–174.

[19] Casalino, D. An advanced time approach for acoustic analogy predictions. *J. Sound. Vib. 261 (4)* (2003), 583–612.

[20] Cavalieri, A. V. G. *Wavepackets as sound-source mechanisms in subsonic jets.* PhD thesis, École doctorale : Sciences et ingénierie en matériaux, mécanique, nergétique et aéronautique - SIMMEA, Poitiers, France, Juin 2012.

[21] Chang, C. L., Malik, M. R., Erlebacher, G., and Hussaini, M. Y. Compressible stability of growing boundary layers using parabolised stability equations. No. AIAA 1991-1636.

[22] Cheung, L. C., Bodony, D. J., and Lele, S. K. Noise radiation predictions from jet instability waves using a hybrid nonlinear PSE-acoustic analogy approach. No. AIAA 2007-3638.

[23] Cheung, L. C., and Lele, S. K. Acoustic radiation from subsonic and supersonic mixing layers with nonlinear PSE. No. AIAA 2004-0363.

[24] Cheung, L. C., and Lele, S. K. Linear nd nonlinear precesses in two-dimensional mixing layer dynamics and sound radiation. *J. Fluid Mech. 625* (2009), 321–351.

[25] Chomaz, J. M. Linear and non-linear, local and global stability analysis of open flows. *Turbulence in spatially extended systems 5* (1993), 245–257.

[26] Colonius, T., and Lele, S. K. Computational aeroacoustics: progress on nonlinear problems of sound generation. *Prog. Aerosp. Sci. 40* (2004), 345–416.

[27] Crow, S. C., and Chamapagne, F. H. Orderly structure in jet turbulence. *J. Fluid Mech. 48* (1971), 547–591.

[28] Curle, N. The influence of solid boundaries upon aerodynamic sound. vol. 231 of *Proceedings of the Royal Society of London*, pp. 505–514.

[29] Day, M., Mansour, N., and Reynolds, W. Nonlinear stability and structure of compressible reacting mixing layers. *J. Fluid Mech. 446* (2001), 375–408.

[30] Farassat, F. Theory of noise generation from moving bodies with an application to helicopter rotors. In *NASA technical report* (1975), NASA.

[31] Farassat, F. Introduction to generalized functions with applications in aerodynamics and aeroacoustics. In *NASA technical report* (1994).

[32] Farassat, F. Derivation of formulations 1 and 1a of Farassat. In *NASA technical report* (2007), NASA.

[33] Farassat, F., and Myers, M. Extension of Kirchhoffs formula to radiation from moving surfaces. *J. Sound. Vib. 3* (1988), 451–460.

[34] Ffowcs Williams, J. The noise from turbulence convected at high speed. *Philosophical Transactions of the Royal Society of London 255*, 1061 (1963), 469–503.

[35] Ffowks williams, J., and Hawkings, D. Sound generetion by turbulence and surfaces in arbitrary motion. *Mathematical and Physical Sciences 264* (1969), 321–342.

[36] Francescantonio, P. D. A new boundary integral formulation for the prediction of sound radiation. *J. Sound. Vib. 202* (1997), 491–509.

[37] Giannetti, F., and Luchini, P. Structural sensitivity of the first instability of the cylinder wake. *J. Fluid Mech. 581* (2007), 167–197.

[38] Glowinski, R. Finite element methods for the numerical solution of incompressible viscous flow. introduction to the control of the Navier-Stokes equations. vol. 28 of *Lectures in Appl. Math.*, pp. 219–301.

[39] Godrèche, C., Menneville, P., and Castaing, B. Hydrodynamics and non linear istabilities. Cambrige University Press.

[40] Goldstein, G. A generalized acoustic analogy. *J. Fluid Mech. 488* (2003), 315–333.

[41] Goldstein, M. A unified approach to some recent developments in jet noise theory. *Int. J. Aeroacoustics 1*, 1 (2002), 1–16.

[42] Gudmundsson, K., and Colonius, T. Parabolized Stability Equation models for turbulent jets and their radiated sound. No. AIAA 2009-3380.

[43] Gudmundsson, K., and Colonius, T. Instability wave models for the near-field fluctuations of turbulent jets. *J. Fluid Mech. 689* (2011), 97–128.

[44] Gunzburger, M., Hou, L. S., and Svobodny, T. P. Numerical approximation of optimal control problem associated with the Navier-Stokes equations. vol. 2 of *Appl. Math. Lett.*, pp. 29–31.

[45] Gunzburger, M., Hou, L. S., and Svobodny, T. P. Boundary velocity control in incompressible flow with an application to viscous drag reduction. *SIAM J. Control Optim 30* (1992), 167–181.

[46] Hardin, J. C., and Lamkin, S. L. Aeroacoustic computation of cylinder wake flow. *AIAA Journal 22(1)* (1984), 51–57.

[47] Hawkings, D. L. Noise generation by transonic open rotors. *Mechanics of Sound Generation in Flows 1* (1979), 294–300.

[48] Herbert, T. Boundary-layer transition analysis and prediction revisited. No. AIAA 91-0737.

[49] Herbert, T. Parabolized Stability Equations. *AGARD REPORT* (1993).

[50] Herbert, T. Parabolized Stability Equations. *Annu. Rev. Fluid Mech. 29* (1997), 245–283.

[51] Herbert, T., and Bertolotti, F. Stability analysis of non-parallel boundary layers. *Bull. Am. Phys. Soc. 32* (1987).

[52] Hill, D. C. A theoretical approach for analyzing the re-stabilization of wakes. In *NASA technical memorandum* (1992), NASA.

[53] Hill, D. C. Adjoint systems and their role in the receptivity problem for boundary layers. *J. Fluid Mech. 292* (1995), 183–204.

[54] Howe, M. S. Contributions to the theory of aerodynamic sound, with application to excess jet noise and the theory of the flute. *J. Fluid Mech. 71 (4)* (1975), 625–673.

[55] Howe, M. S. Theory of vortex sound. vol. 33 of *Cambridge University Press.*

[56] Huerre, P., and Monkewitz, P. A. Local and global instabilities in spatially developing flows. *Annu. Rev. Fluid Mech. 22 (1)* (1990), 473–537.

[57] J. M. Seiner, T. R. S. B., and Ponton, M. K. Relationship between instability waves and noise of high-speed jets. *AIAA Journal 30* (1992), 1747–1767.

[58] Joslin, R. D., Gunzburger, M. D., Nicolaides, R. A., Erlebacher, G., and Hussaini, M. Y. A self-contained, automated methodology for optimal flow control validated for transition delay. *AIAA Journal 35 (5)* (1997), 816–824.

[59] Kim, J., Bodony, D. J., and Freund, J. B. Adoint-based control of loud events in a turbulent jet. *J. Fluid Mech. 741* (2014), 28–59.

[60] Kirchhoff, G. Zur theorie der lichtstrahlen. vol. 254 of *Annalen der Physik*, pp. 663–695.

[61] Ladeinde, F., Alabi, K., Colonius, T., Gudmundsson, K., Schlinker, R., and Reba, R. An integrated RANS-PSE-wave packet tool for the prediction of subsonic and supersonic jet noise. No. AIAA 2010–4021.

[62] Lele, S. K. Compact finite difference schemes with spectral-like resolution. *J. Comput. Phys. 103* (1992), 16–42.

[63] Léon, O. *Étude du rayonnement acoustique des instabilités hydrodynamiques de jets double-flux avec les Équations de stabilité parabolisées (PSE).* PhD thesis, Université de Toulouse, INPT, Toulouse, France, April 2012.

[64] Léon, O., and Brazier, J.-P. Application of linear Parabolized Stability Equations to a subsonic coaxial jet. In *AIAA/CEAS, 32nd Aeroacoustics Conference* (2011).

[65] Li, F., and Malik, M. R. On the nature of PSE approximation. *Int. J. Comput. Fluid D. 8* (1996), 253–273.

[66] Lighthill, M. On sound generated aerodynamically. I. General theory. *Proc. R. Soc. Lond. A. 211* (1952), (1107),564–297.

[67] Lighthill, M. On sound generated aerodynamically. II. Turbulence as a source of sound. *Proc. R. Soc. Lond. A. 222* (1954), (1148),1–32.

[68] Lilley, G. On the noise from jets. *AGARD REPORT* (1974).

[69] Lowson, M. The sound field for singularities in motion. vol. 286 of *Proceedings of the Royal Society of London*, pp. 559–572.

[70] Lowson, M. V., and Ollerhead, J. B. Visualization of noise from cold supersonic jets. *J. Acoustics Soc. Am. 44* (1968), 624.

[71] Luchini, P., and Bottaro, A. Adjoint equations in stabilty analysis. *Annu. Rev. Fluid Mech. 46* (2014), 1–30.

[72] Lyrintzis, A. S. review: the use of Kirchhoffs method in computational aeroacoustics. *J. Fluid Eng. 116 (4)* (1994), 665–676.

[73] Lyrintzis, A. S. Surface integral methods in computational aeroacoustics. From the (CFD) near-field to the (acoustic) far-field. *Int. J. Aeroacoustics 2* (2003), 95–128.

[74] Lyrintzis, A. S., and Mankbadi, R. R. Prediction of the far-field jet noise using Kirchhoffs formulation. *AIAA Journal 34 (2)* (1996), 413–416.

[75] Mankbadi, R. R., Hayder, M. E., and Povinelli, L. A. Structure of supersonic jet flow and its radiated sound. *J. Fluid Mech. 32 (5)* (1994), 897–906.

[76] Marquet, O., Sipp, D., and Jaquin, L. Sensitivity analysis and passive control of cylinder flow. *J. Fluid Mech. 615* (2008), 221–252.

[77] Mathelin, L., and Hussaini, M. A stochastic collocation algorithm for uncertainty analysis. In *NASA technical report/CR-2003-212153* (2003), NASA.

[78] McLaughlin, D. K., Morrison, G. L., and Toutt, T. R. Experiments on the instability waves in a supersonic jet and their acoustic radiation. *J. Fluid Mech. 69* (1975), 73–95.

[79] McLaughlin, D. K., Morrison, G. L., and Toutt, T. R. Reynolds number dependence in supersonic jet noise. *AIAA Journal 15* (1977), 526–532.

[80] McLaughlin, D. K., Seiner, J. M., and Liu, H. On the noise generated by large scale instabilities in supersonic jets. No. 80-0964 in AIAA-paper.

[81] Michalke, A. Instability of a compressible circular free jet with consideration of the influence of the jet boundary layer thickness. In *NASA technical memorandum, TM-75190* (1977).

[82] Mitchell, B. E., Lele, S. K., and Moin, P. Direct computation of the sound generated by vortex pairing in an axisymmetric jet. *J. Fluid Mech. 383* (1999), 113–142.

[83] Mollö-Cristensen, E., and Narashima, R. Sound emission from jets at high subsonic velocities. *J. Fluid Mech. 8(01)* (1960), 49:60.

[84] Monkewitz, P. A., Bechert, D. W., Barsikow, B., and Lehmann, B. Self-excited oscillations and mixing in a heated round jet. *J. Fluid Mech. 213 (1)* (1990), 611–639.

[85] Monkewitz, P. A., and Sohn, K. D. Absolute instability in hot jets. *AIAA Journal 26* (1988), 911–916.

[86] Moore, C. J. The role of shear-layer instability waves in jet exhaust noise. *J. Fluid Mech. 80 (2)* (1977), 321–367.

[87] Morgans, W. XIV. The Kirchhoff formula extended to a moving surface,. vol. 9 of *The London, Edinburgh, and Dublin Philosophical Magazine and Journal of Science*, pp. 141–161 1930.

[88] Morris, P. J. The spatial viscous instability of axisymmetric jets. *J. Fluid Mech. 77* (1976), 511–529.

[89] Morris, P. J., Long, L. N., Scheidegger, T. E., Wang, Q., and Pilon, A. R. High speed jet noise simulations. No. AIAA 98-2290.

[90] Najafi-Yazdi, A., Brés, G. A., and Mongeau, L. An acoustic analogy formulation for moving sources in uniformly moving media. vol. 467 of *Proceedings of the Royal Society of London*, pp. 144–165.

[91] Nichols, J., and Lele, S. Global modes and transient response of a cold supersonic jet. *Annu. Rev. Fluid Mech. 669 (1)* (2011), 225–241.

[92] Panda, J. Shock oscillation in underexpanded screeching jets. *J. Fluid Mech. 363* (1998), 173–198.

[93] Papamoschou, D. A new method for jet noise suppression in turbofan engines. No. 03-1053 in AIAA-paper.

[94] Pérez, C., Puigt, G., Airiau, C., and Boussuge, J. F. Large Eddy Simulation of shock-cell noise from a dual stream jet. No. 16-2798 in AIAA-paper.

[95] Perrault-Joncas, D., and Maslowe, S. A. Linear stability of a compressible coaxial jet with continuous velocity and temperature profiles. *Phys. Fluids 20(7)*, 074102 (2008).

[96] Phillips, O. On the generation of sound by supersonic turbulent shear layers. *J. Fluid Mech. 9 (1)* (1960), 1–28.

[97] Pilon, A. R., and Lyrintzis, A. S. Development of an improved Kirchhoff method for jet aeroacoustics. *AIAA Journal 36 (5)* (1998), 783–790.

[98] Piot, E., Casalis, G., Muller, F., and Bailly, C. Investigation of the PSE approach for subsonic and supersonic hot jets. detailed comparison with les and linearized euler equations results. *International Journal of Aeroacoustic 5-4* (2006), 361–393.

[99] Powell, A. On the mechanism of choked jet noise. vol. 66 of *Proceedings of the Physical Society*, pp. 1039–1057.

[100] Powell, A. Theory of vortex sound. *Journal of the Acoustical Society of America 36 (1)* (1964), 177–195.

[101] Pralits, J. O., Airiau, C., Hanifi, A., and Henningson, D. S. Sensitivity analysis using adjoint parabolized stability equations for compressible flows. *Flow Turbul. Combust. 65*, 3/4 (2000), 321–346.

[102] Ray, P. K., Lawrence, C., Cheung, C., and Lele, S. K. On the growth and propagation of linear instability waves in compressible turbulent jets. *Phys. Fluids 21* (2009).

[103] Ray, P. K., and Lele, S. K. Sound generated by instability wave/shock-cell interaction in supersonic jets. *J. Fluid Mech. 587* (2007), 173–215.

[104] Rayleigh, L. On the question of the stability of the flow of fluids. vol. 1892 of *Philosophical Magazine*, pp. 59–70.

[105] Reynolds, O. An experimental investigation of the circumstances which determine whether the motion of water shall be direct or sinuous, and of the law of resistance in parallel channels. vol. 35 of *Proceedings of the Royal Society of London*, pp. 224–226.

[106] Rodríguez, D., Samanta, A., Cavalieri, A. V. G., Colonius, T., and Jordan, P. Parabolized Stability Equation models for predicting large-scale mixing noise of turbulent round jets. No. AIAA 2011-2838.

[107] Rodríguez, D., Sinha, A., brés, G. A., and Colonius, T. Acoustic field associated with parabolized stability equation models in turbulent jets. No. AIAA 2013-2279.

[108] S. G. Rubin, J. C. T. Parabolized/reduced Navier-Stokes computational techinques. *Annu. Rev. Fluid Mech. 24* (1992), 117–144.

[109] Saltelli, A., Annoni, P., Azzini, I., Campolongo, F., Ratto, M., and Tarantola, S. Variance based sensitivity analysis of model output. design and estimator for the total sensitivity index. *Computer Physics Communications 181* (2010), 259–279.

[110] Schmid, P. J. Nonmodal stability theory. *Annu. Rev. Fluid Mech. 39* (2007), 129–162.

[111] Sinha, A., Gaitonde, D. V., and Sohoni, N. Parabolized stability analysis of dual-stream jets. No. 16-3057 in AIAA-paper.

[112] Sinha, A., Rodriguez, D., Brés, G. A., and Colonius, T. Wavepacket model for supersonic jet noise. *J. Fluid Mech. 742* (2104), 71–95.

[113] Smolyak, S. Quadrature and interpolation formulas for tensor products of certain classes of functions. *Soviet Math. Dokl 4* (1963), 240–243.

[114] Spagnoli, B., and Airiau, C. Adjoint analysis for noise control in a two-dimensional compressible mixing layer. *Computers and Fluids 37* (2008), 475–486.

[115] Sritharan, S. Dynamic programming of Navier-Stokes equations. vol. 16 of *System Control Lett.*, pp. 299–307.

[116] Stefano, D. D., Rona, A., Hall, E., and Puigt, G. Implementing the ffowcs williams and hawkings acoutic analogy in antares. In *22nd International Congress on Sound and Vibration* (Florence, Italy, 2015).

[117] Suzuki, T., and Colonius, T. Instability waves in a subsonic round jet detected using a near- field phased microphone array. *J. Fluid Mech. 565* (2006), 197–226.

[118] Tam, C. K. Computational aeroacoustics-issues and methods. *AIAA Journal 33* (1995), 1788–1796.

[119] Tam, C. K. Supersonic jet noise. *Annu. Rev. Fluid Mech. 27(1)* (1995), 17–43.

[120] Tam, C. K., Pastouchenko, N. N., and Viswanathan, K. Computation of shock cell structure of dual-stream jets for noise prediction. *AIAA Journal 46 (11)* (2008), 2857–2867.

[121] Tam, C. K. W. Directional acoustic radiation from a supersonic jet generated by shear layer instability. *J. Fluid Mech. 46*, 4 (1971), 757–768.

[122] Tam, C. K. W., and Burton, D. E. Sound generated by instability waves of supersonic flows. part 1.. two-dimensional mixing layers. *J. Fluid Mech. 138* (1984), 249–271.

[123] Tam, C. K. W., and Burton, D. E. Sound generated by instability waves of supersonic flows. part 2. axisymmetric jets. *J. Fluid Mech. 138* (1984), 273–295.

[124] Tam, C. K. W., and Chen, P. A statistical model of turbulence in two-dimensional mixing layers. *J. Fluid Mech. 92* (1979), 303–326.

[125] Theofilis, V. Advances in global linear instability analysis of nonparallel and three-dimensional flows. *Progress in Aerospace Sciences 39 (4)* (2003), 249–316.

[126] Thurow, B., Samimy, M., and Lempert, W. compressibility effects on turbulence structures of axisymmetric mixing layers. *Phys. Fluids*, 5 (2003), 1755–1765.

[127] Tissot, G., Zang, M., Lajús, F. J., Cavalieri, A., Jordan, P., and Colonius, T. Sensitivity of wavepackets in jets to non-linear effects: the role of the critical layer. No. AIAA 2015-2218.

[128] Troutt, T. R. *Measurements on the flow and acoustic properties of a moderate-Reynolds number supersonic jet.* PhD thesis, Oklahoma State University, 1978.

[129] Troutt, T. R., and McLaughlin, D. K. Experiments on the flow and acoustic properties of a moderate Reynolds-number supersonic jet. *J. Fluid Mech. 116* (1982), 123–156.

[130] Viswanathan, K. Parametric study of noise from dual-stream nozzles. *J. Fluid Mech. 521* (2004), 35–68.

[131] Walther, S., Airiau, C., and Bottaro, A. Optimal control of Tollmien-Schlichting waves in a developing boundary layer. *Phys. Fluids 13*, 7 (2001), 2087–2096.

[132] Wei, M., and Freund, J. B. A noise-controlled free shear flow. *J. Fluid Mech. 546* (2006), 123–152.

[133] Yen, C. C., and Messersmith, N. L. Application of Parabolized Stability Equations to the prediction of jet instabilities. In *AIAA/ASME, 36th Conference* (1998).

[134] Yen, C. C., and Messersmith, N. L. The use of compressible parabolized stability equations for predicition of jet instabilities and noise. No. 99-1859 in AIAA-paper.

# Appendix

Any field $\Phi(x, r, \theta, t)$ is decomposed into a base flow $\bar{\phi}(x, r)$ and a disturbance $\phi'(x, r, \theta, t)$.

## A - PSE MATRICES

All the values contained to the matrices are referred to the baseflow:

$$A_0 = \begin{bmatrix} 0 & \bar{\rho} & 0 & \bar{u}_r & 0 \\ 0 & \bar{\rho}\bar{u}_r & 0 & 0 & 1 \\ 0 & 0 & \bar{\rho}\bar{u}_r & 0 & 0 \\ \bar{\rho}\bar{u}_r & 0 & 0 & 0 & 0 \\ 0 & 0 & 0 & -\bar{u}_r & \bar{\rho}\bar{u}_r M^2 \end{bmatrix} \quad A_1 = \begin{bmatrix} \bar{\rho} & 0 & 0 & \bar{u}_x & 0 \\ 0 & \bar{\rho}\bar{u}_x & 0 & 0 & 0 \\ 0 & 0 & \bar{\rho}\bar{u}_x & 0 & 0 \\ \bar{\rho}\bar{u}_x & 0 & 0 & 0 & 1 \\ 0 & 0 & 0 & -\bar{u}_x & \bar{\rho}\bar{u}_x M^2 \end{bmatrix}$$

$$A_2 = \begin{bmatrix} 0 & 0 & \bar{\rho} & 0 & 0 \\ 0 & 0 & 0 & 0 & 0 \\ 0 & 0 & 0 & 0 & 1 \\ 0 & 0 & 0 & 0 & 0 \\ 0 & 0 & 0 & 0 & 0 \end{bmatrix} \quad A_3 = \begin{bmatrix} 0 & 0 & 0 & 1 & 0 \\ 0 & \bar{\rho} & 0 & 0 & 0 \\ 0 & 0 & \bar{\rho} & 0 & 0 \\ \bar{\rho} & 0 & 0 & 0 & 1 \\ 0 & 0 & 0 & -1 & \bar{\rho}M^2 \end{bmatrix}$$

$$B = \begin{bmatrix} \dfrac{\partial \bar{\rho}}{\partial x} & \dfrac{\bar{\rho}}{r} + \dfrac{\partial \bar{\rho}}{\partial r} & 0 & \dfrac{\bar{u}_r}{r} + \dfrac{\partial \bar{u}_x}{\partial x}\dfrac{\partial \bar{u}_r}{\partial r} & 0 \\ \bar{\rho}\dfrac{\partial \bar{u}_r}{\partial x} & \bar{\rho}\dfrac{\partial \bar{u}_r}{\partial r} & 0 & 0 & 0 \\ 0 & 0 & \dfrac{\bar{\rho}\bar{u}_r}{r} & 0 & 0 \\ \bar{\rho}\dfrac{\partial \bar{u}_x}{\partial x} & \dfrac{\partial \bar{\rho}}{\partial r} & 0 & 0 & 0 \\ -\dfrac{\partial \bar{\rho}}{\partial x} & -\dfrac{\partial \bar{\rho}}{\partial x} & 0 & 0 & 0 \end{bmatrix}$$

# B - APSE EQUATION

## B-1 Procedure

All the different directional derivatives vanish with exception of $\dfrac{\partial \mathcal{L}}{\partial \boldsymbol{f}}\delta \boldsymbol{f}$. It yields

$$\begin{aligned} \frac{\partial \mathcal{L}}{\partial \boldsymbol{q}}\delta \boldsymbol{q} &= \chi_f \left\langle \left( A^h + B^h - \frac{\partial A_1^h}{\partial x} - \frac{\partial A_0^h}{\partial r} - \frac{1}{r}A_0^h \right) \boldsymbol{q}^*, \delta \boldsymbol{q} \right\rangle_\Omega - \chi_f \left\langle A_1^h \frac{\partial \boldsymbol{q}^*}{\partial x} + A_0^h \frac{\partial \boldsymbol{q}^*}{\partial r}, \delta \boldsymbol{q} \right\rangle_\Omega \\ &+ \left\langle \bar{n}^* \frac{\partial \boldsymbol{q}}{\partial x} - \frac{\partial \left(n^* \boldsymbol{q}\right)}{\partial x}, \delta \boldsymbol{q} \right\rangle_\Omega - \chi \bar{\chi} \left\langle \boldsymbol{q}, \delta \boldsymbol{q} \right\rangle_\Omega \\ &+ \chi_f \left\langle A_{1f}^h \boldsymbol{q}_f^*, \delta \boldsymbol{q}_f \right\rangle_r + \left\langle n_f^* \boldsymbol{q}_f, \delta \boldsymbol{q}_f \right\rangle_r \\ &+ \chi_f \int_{x_0}^{x_f} \left[ (A_0^t \bar{\boldsymbol{q}}^*)^t \delta \boldsymbol{q}\, r \right]_{r=0}^{r=\infty} dx + c.c. = 0 \end{aligned}$$

$$\begin{aligned} \frac{\partial \mathcal{L}}{\partial \alpha}\delta \alpha &= \int_{x_0}^{x_f} \left( \left\langle \chi \boldsymbol{q}, \chi \boldsymbol{q} \right\rangle_r \int_{x_0}^{x} \delta\alpha d\xi \right) dx - \chi_f \int_{x_0}^{x_f} \left( \int_0^\infty \frac{\partial \left( \boldsymbol{q}^{*h} A_1 \boldsymbol{q} \right)}{\partial x} r\, dr \int_{x_0}^{x} \delta\alpha d\xi \right) dx \\ &+ \chi_f \left\langle \boldsymbol{q}_f^*, A_{1f} \boldsymbol{q}_f \right\rangle_r \delta\alpha_f + c.c. = 0 \end{aligned}$$

with $A = i\alpha A_1 + imA_2 - i\omega A_3$ and $\chi_f = \chi(x_f) = \bar{\chi}^*(x)\chi(x)$.

Imposing:

$$\frac{\partial \mathcal{L}}{\partial \boldsymbol{q^*}}\delta \boldsymbol{q^*} = \boldsymbol{0} \qquad \text{and} \qquad \frac{\partial \mathcal{L}}{\partial n^*}\delta n^* = 0$$

we obtain respectively Eq. 2.26 and Eq. 2.33.

## B-2 Adjoint Parabolized Stability Equations

Since all variations are arbitrary, except at boundaries where the conditions are fixed (such as, for example, at $x = x_0$).

- the different integrals vanish if the following Euler-Lagrange equations are satisfied:

$$L^*_{PSE}\boldsymbol{q}^* = \boldsymbol{g}(\boldsymbol{q}, n^*)$$

with

$$L^*_{PSE} = -\frac{1}{r}{A_0}^h + A^h + B^h - \frac{\partial A_1^h}{\partial x} - \frac{\partial A_0^h}{\partial r} - A_1^h\frac{\partial}{\partial x} - A_0^h\frac{\partial}{\partial r}$$

and

$$\boldsymbol{g}(\boldsymbol{q}, n^*) = \frac{1}{\bar{\chi}_f}\left[(n^* - \bar{n}^*)\frac{\partial \boldsymbol{q}}{\partial x} + \left(\frac{\partial n^*}{\partial x} + \chi\bar{\chi}\right)\boldsymbol{q}\right]$$

- closing relation:

$$\langle\chi\boldsymbol{q}, \chi\boldsymbol{q}\rangle_r + \int_0^\infty \left(\chi_f \frac{\partial\left(\boldsymbol{q}^{*h} A_1 \boldsymbol{q}\right)}{\partial x}\right) r\, dr + c.c. = 0$$

It is equation 3.28.

- terminal conditions:

$$\chi_f \int_0^\infty \boldsymbol{q}_f^{*h} A_{0f} \boldsymbol{q}_f\, r\, dr + c.c. = 0 \qquad \text{and} \qquad \bar{\chi}_f A_{1f}^h \boldsymbol{q}_f^* + n_f^* \boldsymbol{q}_f + c.c. = 0$$

- boundary condition:

$$\left[\bar{\chi}_f r A_0^h \boldsymbol{q}^*\right]_{r=0} + c.c. = 0 \qquad \text{and} \qquad \left[\bar{\chi}_f r A_0^h \boldsymbol{q}^*\right]_{r=\infty} + c.c. = 0$$

# C - AFW-H

*Thickness noise*

$$\begin{aligned} 4\pi p'_Q(\boldsymbol{x},t) = &\int_{g=0} \left[\frac{\rho_0 \left(\dot{U}_n + U_{\dot{n}}\right)}{r(1-M_r)^2}\right]_{ret} dS \\ &\int_{g=0} \left[\frac{\rho_0 U_n \left(r\dot{M}_r + c_0(M_r - M^2)\right)}{r^2(1-Mr)^3}\right]_{ret} dS \end{aligned} \tag{14}$$

with

$$U_n = U_i \hat{n}_i, \quad U_{\dot{n}} = U_i \, \dot{\hat{n}}_i, \quad \dot{U}_n = \dot{U}_i \hat{n}_i, \tag{15}$$

$$M_r = M_i \hat{r}_i, \quad \dot{M}_r = \dot{M}_i \hat{r}_i \tag{16}$$

*Loading noise*

$$\begin{aligned} 4\pi p'_L(\boldsymbol{x},t) = &\frac{1}{c_0}\int_{g=0} \left[\frac{\dot{L}_r}{r(1-M_r)^2}\right]_{ret} dS + \\ &\int_{g=0} \left[\frac{L_r - L_m}{r^2(1-M_r)^2}\right]_{ret} dS + \\ &\frac{1}{c_0}\int_{g=0} \left[\frac{\dot{L}_r \left(r\dot{M}_r + c_0(M_r - M^2)\right)}{r^2(1-M_r)^3}\right]_{ret} dS \end{aligned} \tag{17}$$

with

$$L_r = L_i \hat{r}_i, \quad \dot{L}_r = \dot{L}_i \hat{r}_i, L_M = L_i M_i. \tag{18}$$

*Quadrupole noise*

$$4\pi p'_t(\boldsymbol{x},t) = \int_{g>0} \left[\frac{K_1}{c_0^2 r} + \frac{K_2}{c_0 r^2} + \frac{K_3}{r^3}\right]_{ret} dV, \tag{19}$$

with

$$K_1 = \frac{\ddot{T}_{rr}}{(1-M_r)^2} + \frac{\ddot{M}_r T_{rr} + 3\dot{M}_r \dot{T}_{rr}}{(1-M_r)^4} + \frac{3\dot{m}_r^2 T_{rr}}{(1-M_r)^5} \tag{20}$$

$$\begin{aligned} K_2 = & \frac{\dot{T}_{ii}}{(1-M_r)^2} - \frac{4\dot{T}_{M_r} + 2T_{\dot{M}_r} + \dot{M}_r \dot{T}_{ii}}{(1-M_r)^3} + \\ & \frac{3[(1-M^2)\dot{T}_{rr} - 2\dot{M}_r T_{M_r} - M_i \dot{M}_r T_{rr}]}{(1-M_r)^4} + \\ & \frac{6\dot{M}_r (1-M^2) T_{rr}}{(1-M_r)^5} \end{aligned} \tag{21}$$

$$K_3 = \frac{2T_{mm} - (1-M^2)T_{ii}}{(1-M_r)^3} - \frac{6(1-M^2)T_{M_r}}{(1-M_r)^4} + \frac{3(1-M^2)T_{rr}}{(1-M_r)^5} \tag{22}$$

$$T_{MM} = T_{ijM_iM_j}, \quad Tm_r = T_{ij}M_i\hat{r}_j, \quad T_{\dot{M}_r} = T_{ij}\dot{M}_i\hat{r}_j \tag{23}$$

$$\dot{T}_{M_r} = \dot{T}_{ij}M_i\hat{r}_j, \quad \dot{T}_{rr} = \dot{T}_{ij}\hat{r}_i\hat{r}_j, \quad \ddot{T}_{rr} = \hat{r}_i\hat{r}_j \tag{24}$$

In equations 14, 17, 19, the convention $[\ldots]_{ret}$ is adopted to indicate that the quantities inside the square brackets are evaluated at the retarded time

$$t_{ret} = t - \frac{|\boldsymbol{x} - \boldsymbol{y}(\tau_{ret})|}{c_0} \tag{25}$$

Equation 25 expresses that a disturbance emitted from the source position $\boldsymbol{y}$ at time $\tau_{ret}$ will reach the observer $\boldsymbol{x}$ at time $t$, due to the time of flight of the noise propagating at the speed of sound $c_0$. Equations 14, 17, 19 are a consequence of applying the free space Green's function

$$G(\boldsymbol{x}, \boldsymbol{y}, t, \tau) = \frac{\delta(t - \tau - \frac{|\boldsymbol{x} - \boldsymbol{y}|}{c_0})}{r} \tag{26}$$

to the wave operator in the FW-H equation, eq. 5.1.